Phase diagrams and defect thermodynamics to devise doping strategies in lead chalcogenide thermoelectric materials and its alloys

Thesis by

Saurabh Bajaj

In Partial Fulfillment of the Requirements

for the Degree of

Doctor of Philosophy

California Institute of Technology

Pasadena, California

2016

(Defended Oct 23rd, 2015)

I would like to dedicate the work that went into this thesis to my family and the support system at Caltech, including my advisor, G. Jeffrey Snyder.

Acknowledgements

First and foremost, as clichéd as it may sound, this work would really have not been possible without the support of my parents. They provided me with not only their hard-earned life savings to enable me to explore life and gain knowledge in this country, but also the emotional support and mental strength that I sought during many tough times.

I cannot thank my advisor, G. Jeffrey Snyder, enough for his support and patience with me while I explored how my interest and experience in computational thermodynamics and phase stability could be applied to the field of thermoelectric materials research. As he always maintained that his door is always open for students (so much so that he never set up appointment times with us), every one of my visits to his office filled me with motivation and encouragement. His enthusiasm for my projects (which was at times more than mine), technical expertise, and relentless pursuit for interesting science were critical in the coming about of this work. His extremely approachable and informal attitude, together with his ability to offer just about the right amount of guidance to his students (i.e., a balance between the extremes of hands-on and hands-off approaches) are qualities that not only proved to be beneficial, but according to me, are those of an ideal advisor.

The thermoelectric group members (most of whom have now graduated) are a great bunch of intellectuals full of fun and laughter, who are also very kind. I learned a lot about experimental techniques used in our labs from both Zachary Gibbs and Heng Wang, who patiently explained them to a novice like me. Zachary Gibbs also introduced me to the Materials Project (https://www.materialsproject.org/), and offered a lot of optimistic advice, both of which I am very grateful to him for. Gregory Pomrehn, and Jeff Doak and Christopher Wolverton of Northwestern University offered tremendous expertise and advice which was critical to my understanding of the

complexity of defect physics.

Caltech goes out of the way to make students' lives easier so that they have nothing else to worry about except academics, and I was a first-hand witness to this. Felicia Hunt and Natalie Gilmore of the Graduate Office, Maria Oh, Mariel Tourani, Charisma Bartlett, Alice Sogomonian, and Divina Bautista of the Health and Counseling Center are some of the many wonderful and critical members of the Caltech community who offered me immense support and encouragement throughout my years at Caltech.

The first few years at Caltech are generally pretty tough times for graduate students due to the burden of classes and preparation for qualifying/candidacy examinations, and I want to thank a few people who helped me make that time manageable. Nicolas Batara, my friend and colleague, spent a lot of the first year working together on problem sets. He is a gold mine of qualities, both personal and professional, that I admire and spent many lunches experiencing in awe. I am very thanful for what I have learned from them so far, and hope to continue to do so in the future. Gregory Atrian, mi amigo, not only gave me confidence during hard times, but always made him himself available to me for help when I needed it. He and I spent many weekends exploring Los Angeles and the vast amount of variety it offers in terms of cultures and cuisines. My friends, Lee Wilson and Pablo Guerrero, helped me escape the stresses of academic life with lots of laughter. Members of the MatSci lunch group including John Lloyd, Erik Verlage, and others provided for some entertaining times. I may have bothered Brent Fultz, one of my committee members, with an endless number of questions on the topics of entropy, thermodynamics, and kinetics, during/after his class and over email, but he patiently answered all of them to help me hold a strong grasp of the subjects.

I owe my mentors, Raymundo Arröyave at Texas A&M University and Patrice Turchi at Lawrence Livermore National Laboratory, for all the support they provided to help propel me toward joining Caltech. Without them, I may not have reached this stage in my career, and I am grateful for their continued support. Sadasivan Shankar, who mentored me during my internship at Intel in the summer of 2013, taught me how to face and approach seemingly unsolvable and daunting problems, an invaluable skill. His guidance was vital to the nano phase diagram work described in this thesis, which I am very proud of.

A lot of my time at Caltech was spent swinging rackets in the recreational facilities at Caltech while playing tennis, squash, and most recently, UK (not US) racketball. These activities helped me keep sane and healthy, socialize, relieve stress, forget all my worries, and most importantly have fun and enjoy the times after work. None of them would be possible without the people who I played against: Evan Creer (tennis), Leslie Chill, Rob, Mark, Bob, Carl, Howard, Ronn, Eli Shechet (squash), and Eli Shechet (UK racketball) for introducing me to the great sport of UK racketball.

Last, but not the least, this work was supported by:
Grants: EDCBEE under Contract No. DEAC02-05CH11231 (DOE), W31P4Q-13-1-0010 (DARPA-ARO), and NSC101-3113-P-008-001 (National Science Council of Taiwan).
Computers: Chemical Engineering (CAT) Cluster at Texas A&M University; Hopper, Carver, and Mendel of National Energy Research Scientific Computing Center (NERSC) at Lawrence Berkeley National Laboratory; Wolf, Atom, and Ion of the Materials and Process Simulation Center (MSC) at Caltech.
Internship opportunities: Intel Corporation, Robert Bosch RTC

Abstract

This thesis discusses the application of phase diagrams and the associated thermodynamics to semiconductor materials through theoretical computational calculations. The majority of work is focused on thermoelectric semiconducting materials that enable direct inter-conversion between electrical and thermal energy. First, one of the most efficient thermoelectric material, PbTe, is picked to demonstrate the assessment of unknown phase diagrams by combining two methods - DFT and CALPHAD. Since there had been no previous investigations of defect stability in this material using computations, DFT is used to deduce the stability of various intrinsic point defects, and in turn attribute origins of n- and p-type conductivity to the most stable defects. Then, the calculated defect formation energies are used in the Pb-Te thermodynamic model built using the CALPHAD method to compare the estimated solubility lines and non-stoichiometric range of the PbTe phase with experimental data. Next, another lead chalcogenide, PbSe, is picked to explore the phase stability of the PbSe phase upon the addition of dopants (Br, Cl, I, Na, Sb, Bi, In), which is a common strategy to make thermoelectric materials and devices more efficient. The range of efficiencies and thermoelectric properties as functions of composition and temperature that can be achieved depends on the amount of dopant that can be added without precipitating secondary phases. Also, depending on the system and its phase diagram, there can be more than one way of doping a material. To help detail which method(s) of doping into PbSe will result in maximum dopant solubility, a procedure similar to the above for PbTe is followed by using DFT in combination with Boltzmann statistics to map solvus boundaries of the PbSe phase, but now in the ternary phase space of composition and temperature. This method also helps predict electrical conductivity, n- or p-type, in each region of the phase diagrams that represent different doping methods.

Lastly, the role of surface energy contributions in changing phase stability at nano-dimensions

is explored. The CALPHAD approach is employed to investigate these changes in three systems by calculating their phase diagrams at nano dimensions and comparing them with their bulk counterparts.

Contents

List of Figures

List of Tables

Chapter 1

Introduction

1.1 Thermoelectric effect and applications

The effect of climate change and global warming in raising earth's average temperature is undeniable considering the available evidence [1, 2]. The rise in temperature will have detrimental effects on the current state of social and economic life. There have been several cycles of glacial advance and retreat in this time period; however, the current trend of glacial melting due to the highest levels of carbon dioxide in the atmosphere in 650,000 years is unprecedented. More importantly, 97% of the scientific community is in robust consensus that this effect is anthropogenic-based [3–5]. Thus, the need for renewable energy technologies such as wind, solar, etc. that do not release greenhouse gases to the atmosphere is urgent, and it is widely agreed that the energy source portfolio of the future will be a mix of these technologies rather than being dominated by one single source.

Waste heat recovery using thermoelectric generators is one such technology that is expected to play an important role in the formation of an energy portfolio, especially considering that somewhere between 20 to 50% of industrial energy input is lost as waste heat in the form of hot exhaust gases, cooling water, and heat lost from hot equipment surfaces and heated products [6]. Thermoelectric materials have already found applications in a wide variety of applications, such as a replacement of alternators in automobiles to directly convert waste exhaust heat to electric power [7, 8], and in radioisotope thermoelectric generator to power space rovers [9, 10], etc. Thermoelectric devices have many advantages over heat engines, such as having spot temperature control and being low maintenance, and, as they are solid-state devices, they have no moving parts, thus

making their operation quiet and vibration free. These advantages enable its application for remote sensing, such as in the Voyager spacecrafts of NASA-JPL, which has been one of its most prolific and successful applications [11]. These deep space probes, after a journey of more than 37 years, have reached interstellar space, the furthest point any man-made object has reached, which proves power stability of thermoelectric devices over extended periods of time.

To be able to convert energy from heat into electrical voltage and vice-versa, the material needs to contain free charge carriers to make this energy transfer possible. It is also desirable that it have high electrical conductivity while maintaining a low thermal conductivity so that charge carriers can be transported without compromising temperature gradient. These characteristics are inter-dependent on each other and on carrier concentrations, as can be seen from Fig. 1.1.

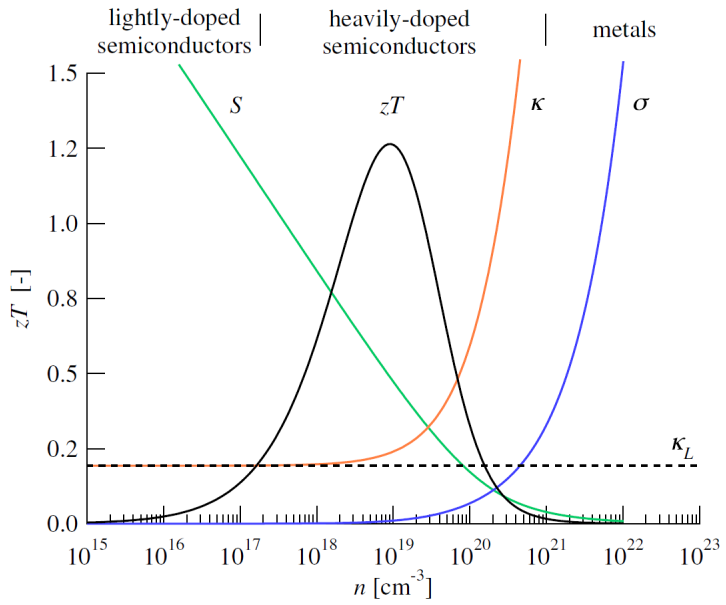

Figure 1.1: Contradictory nature of material properties that contribute to efficiency of thermoelectric materials plotted as functions of carrier concentrations.

The efficiency of thermoelectric materials is measured by the figure of merit zT, which is given by,

$$zT = \frac{S^2\sigma T}{(\kappa_L + \kappa_e)}, \tag{1.1}$$

where, S is the Seebeck coefficient, σ is the electrical conductivity, T is the absolute temperature, and κ_L and κ_e are the lattice and electronic thermal conductivities, respectively. To maximize zT, a large Seebeck coefficient is needed, which is ensured when only a single type of carrier (electrons or holes) is present in the material, while also maximizing electrical conductivity and minimizing thermal conductivity. As can be seen from Fig. 1.1, zT commonly peaks at carrier concentrations of 10^{18} to 10^{21} carriers/cm^3. Such carrier concentrations are typical of low band gap heavily doped semiconductor materials that fall in a domain between metals and conventional semiconductors. The thermoelectric effect is based on three correlated effects: the Seebeck effect, the Peltier effect and the Thomson effect. The Seebeck effect, named after Thomas Johann Seebeck who discovered it in 1822, is most often discussed when characterizing thermoelectric performances, as in practice, the Seebeck effect is most convenient with respect to lab measurements of voltage generated per degree of temperature difference. According to this effect, when one side of the material is heated while the other side is kept cooler, electrons diffuse to the cold side of the material. This phenomenon is schematically shown in Fig. 1.2 in a thermoelectric module consisting of one n-type and one p-type leg that are electrically connected in series and thermally in parallel. To balance this chemical diffusive driving force created by a temperature gradient, a stable electric field/voltage is generated across the material to drive a current I through the resistance R.

1.2 Motivation behind and organization of this thesis

The stumbling block that has kept thermoelectric devices out of widespread commercial applications is their low Carnot efficiency compared with heat engines and their economic evaluations [12]. One of the factors contributing to these low efficiencies occurs at the contacts between source and device in maintaining a steady thermal transfer, but another major contributing factor arises from the efficiency of the material itself. The latter has been subject of the majority of thermoelectric materials research.

The lead chalcogenides (PbQ, Q = Te, Se, S) crystalize in a cubic rock salt structure with space

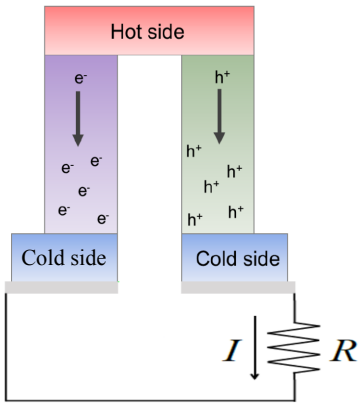

Figure 1.2: Schematic of a thermoelectric module with n-type and p-type legs connected electrically in series and thermally in parallel. As shown, the charge carriers travel from the hot side to the cold side, which drives a current I through the resistance R.

group $Fm\bar{3}m$ (no. 225), and are one of the most well studied class of thermoelectric materials due to their highly symmetric structure, relatively simple defect chemistry, and ease of synthesis without competing phases. They also have the advantages of have narrow band gaps with fairly high carrier mobilities, and their carrier densities are easily tunable between the ranges of 10^{16} to 10^{21} carriers/cm^3 for both n- and p-type operation, thus making them ideal for thermoelectric and optoelectronic applications. PbTe based alloys used in thermoelectric generators have a peak zT of around 0.8 for both n- and p-type operation [13]. The bulk of the work in this thesis is focused on two such lead chalcogenides, PbTe, and its less studied analog, PbSe.

Defect control is critical in semiconductors and a prerequisite to optimize zT not only because intrinsic defects and intentional doping is a primary means of controlling the majority carrier type for charge transport, but also because defects can significantly alter properties of semiconductors. This is challenging and in many cases has impeded the realization of the best zT as predicted. Thus, first in Chapter 3, the stability of intrinsic point defects in PbTe, one of the most widely studied and efficient thermoelectric material, is explored by means of *Ab initio* based Density Functional Theory (DFT) [14, 15], a method that is described in detail in Chapter 2. Prior to this work, to the author's knowledge, there was no study on intrinsic point defects in PbTe, making this work

even more critical. These calculations could prove to be very helpful in determining the defect thermodynamics of various defects in this system. The origin of n- and p-type conductivity in PbTe is attributed to particular intrinsic charged defects by calculating their formation energies. These DFT calculated defect formation energies are then used in the Gibbs free energy description of this phase as part of the Pb-Te thermodynamic model built using the CALPHAD (CALculation of PHAse Diagrams) approach [16] (also described in detail in Chapter 2), and in the resulting phase diagram it is found that its solubility lines and non-stoichiometric range agree very well with experimental data. Such an approach of using DFT in conjunction with CALPHAD for compound semiconductor phases that exhibit very small ranges of non-stoichiometry does not only make the process of calculating phase diagrams for such systems more physical, but is necessary and critical for the assessment of unknown phase diagrams. A CALPHAD type thermodynamic model is necessary to improve our understanding of phase stability, phase equilibrium, and thermodynamics for a system. Chapter 3 presents the methodology and approach of the CALPHAD technique which involves the modeling of Gibbs energies of all the phases taking part in equilibrium through reliable and consistent experimental data. Such a model offers many advantages: (i) it can be extrapolated to regions of temperatures and compositions which are not easily accessible by experiments, (ii) and it provides an easy way to study how equilibria and reactions are affected by various external factors. The use of such techniques plays an even more important role since experiments are challenging and expensive for this class of systems.

For additional control over the performance of a semiconductor for a specific application, an external dopant is usually added to it which allows for precise control over electron and hole densities, which in turn is directly related to the dopant concentration. It is an essential strategy to improve the efficiency of thermoelectric materials and devices. Thermoelectric semiconductors are so heavily doped that their transport properties mimic properties of metals more than semiconductors. The doping levels in these materials are orders of magnitude higher than in other semiconductors, making intrinsic impurities or self-doping less important than extrinsic impurities. To estimate the amount of dopant that can be added to a semiconductor without precipitating secondary phases, a detailed phase diagram is needed. Calculated phase diagrams could be very helpful when time-consuming experimental ones are not available. In Chapter 4, we have calculated dopant solubilities of Br and Na in the thermoelectric material PbSe by mapping its solvus

boundaries in different regions of the respective ternary phase diagrams using DFT defect energy calculations. The narrow gap PbSe provides an example where most defects with charge state as expected from electron count are properly localized, whereas other charge states of defects lead to charge delocalization, which, in effect, alter their charge state to those of localized defects. The equilibrium electron chemical potential is positioned where the defect landscape is dominated by delocalized defects that, from the view of defect thermodynamics, are not expected to be stable or play a role in controlling the majority carrier type or concentration, resulting in unexpected dopant concentrations and solubilities. Experimentally measured doping efficiencies for these systems indicate much higher formation energies for these defects, beyond the inaccuracies of the calculations due to any known reason. Performing thermodynamic calculations using only the expected charge states, precluding others, enables accurate prediction of experimentally measured doping efficiencies and phase diagrams. Utilizing such a method in related semiconductors containing only localized defects will expedite the use of such calculations by experimentalists in understanding phase diagrams and devising effective doping strategies.

Cl, Br, I, Sb, Bi, and In are popular n-type and p-type dopants in PbSe and other chalcogenides. The range of thermoelectric properties as a function of carrier concentration and temperature, such as Seebeck coefficient and electrical conductivity, that can be achieved depends on the amount of dopant that can be added to it without precipitating secondary phases. This requires a mapping of solvus boundaries of the thermoelectric phase in composition and temperature space upon the addition of a dopant. In Chapter 5, we employ density functional theory (DFT) calculations to predict the most stable defects in different regions of thermodynamic phase stability between the PbSe phase and these dopants. When this information is used as input to a statistical mechanics model, we determine the dilute-limit single-phase boundary of PbSe in each ternary system containing the dopant. This enables the calculation of dopant solubility and carrier concentration in PbSe in the ternary composition space as a function of temperature, which helps detail which method(s) of doping into PbSe will result in maximum dopant solubility without precipitating second phases. As will be shown in this chapter, it also helps predict electrical conductivity behavior, electron or hole type, in each phase region representing the different doping methods.

Lastly, in Chapter 6, the effect of grain size of material alloys on their phase stability and phase

diagrams is explored. Phase diagrams of multi-component systems are critical for the development and engineering of material alloys for all technological applications. At nano dimensions, surfaces (and interfaces) play a significant role in changing equilibrium thermodynamics and phase stability. In this work, it is shown that these surfaces at small dimensions affect the relative equilibrium thermodynamics of the different phases. The CALPHAD approach for material surfaces (also termed "nano-CALPHAD") is employed to investigate these changes in three binary systems by calculating their phase diagrams at nano dimensions and comparing them with their bulk counterparts. The surface energy contribution, which is the dominant factor in causing these changes, is evaluated using the spherical particle approximation. Butler's equations are used to calculate alloy surface tensions, which along with bulk thermodynamic models, are used to calculate interaction parameters to develop thermodynamic models. It is first validated with the Au-Si system for which experimental data on phase stability of spherical nano-sized particles is available, and then extended to calculate phase diagrams of similarly sized particles of Ge-Si and Al-Cu. Additionally, the surface energies of the associated compounds are calculated using DFT, and integrated into the thermodynamic model of the respective binary systems. Computed data on melting points of pure components, and alloy surface tensions are compared and agree well with available experimental data. In this work we found changes in miscibilities, reaction compositions of about 5 at.%, and solubility temperatures ranging from 100-200 K for particles of sizes 5 nm, indicating the importance of phase equilibrium analysis at nano dimensions.

Finally, a summary of the thesis is provided in Chapter 7, where it is explained how the results of this work on defect thermodynamics fit within the larger context of determining phase equilibria in binary and ternary multi-component thermoelectric alloys, and directions on future work that can be undertaken to achieve the objective of devising effective doping strategies will be briefly discussed.

Chapter 2

Computational Methodology

2.1 Electronic structure calculations

2.1.1 Introduction

Density Functional Theory (DFT) has been one the most important breakthroughs in the physical sciences in the last 50 years, and is a popular method for the quantum mechanical solution of periodic systems to compute the electronic structure of matter. It has proven to be a very successful approach for the description of ground-state properties of metals, semiconductors, and insulators, and thus its application to study a large number of properties of real materials has seen an explosive growth over the last couple of decades, especially considering the exponential increase in supercomputing power. It is partly a parameterless method, which is why it is sometimes referred to as an *ab inito* method, and so its results are considered fundamental in a physical sense. The fundamental principle of DFT is that any property of a system consisting of many-body interactions can be viewed as a functional of the ground state density, which in principle, determines all information on the ground state. In this section, a succinct description of the formulation is described. A good exposition of the method can be found in Ref. [17].

Consider a solid of atomic number Z, and composed of N number of nuclei. These nuclei are positively charged particles and heavier than the negatively charged electrons. The total number of interacting particles in such a solid becomes $(N + Z.N)$, thus making this a many-body problem. The Hamiltonian for a solid is given by,

$$\begin{aligned}\hat{H} &= -\frac{\hbar}{2}\sum_i \frac{\nabla^2_{\vec{R}_i}}{M_i} - \frac{\hbar}{2}\sum_i \frac{\nabla^2_{\vec{r}_i}}{m_e} \\ &\quad - \frac{1}{4\pi\epsilon_0}\sum_{i,j}\frac{e^2 Z_i}{\mid \overrightarrow{R}_i - \overrightarrow{r}_j \mid} + \frac{1}{8\pi\epsilon_0}\sum_{i\neq j}\frac{e^2}{\mid \overrightarrow{r}_i - \overrightarrow{r}_j \mid} \\ &\quad + \frac{1}{8\pi\epsilon_0}\sum_{i\neq j}\frac{e^2 Z_i Z_j}{\mid \overrightarrow{R}_i - \overrightarrow{R}_j \mid}\end{aligned} \tag{2.1}$$

where the nuclei are of mass M_i and at $\overrightarrow{R_i}$, and the electrons are of mass m_e and at positions $\overrightarrow{r_i}$. The charge of the electron is e. The first two terms are the kinetic energy operators of the nuclei and electrons, respectively. The last three terms describe the Coulombic interactions between a nucleus and an electron, between two electrons, and between two nuclei, respectively.

Even for the modern-day computers, it is extremely challenging to solve Eqn. (2.1) exactly for elements with more than a few electrons. Thus, several approximations are made to ease the calculations. These are briefly described in the following subsections.

2.1.2 The Born-Oppenheimer Approximation

This approximation, also known as the adiabatic approximation, assumes the nuclei to be "frozen" due to their heavier masses. Thus, the kinetic energy term of the nuclei is eliminated, and the potential term now becomes a constant. Thus, only electrons are left as interacting particles in this many-body problem, and Eqn. (2.1) reduces to

$$\hat{H} = \hat{T} + \hat{V} + \hat{V}_{ext}, \tag{2.2}$$

where the first term ($\hat{T}$) is the kinetic energy operator for the electrons, the second term ($\hat{V}$) describes the potential energy between the electrons, and the last term ($\hat{V}_{ext}$) is the potential energy of the electrons in the external potential of nuclei.

2.1.3 Density Functional Theory

After the first level of approximation, the problem becomes simpler, but still remains difficult to solve; the solution of $\hat{H}$ is still intractable for systems with more than a few dozen atoms because the many-body wave function depends on at least 3N variables for a system with N interacting electrons. Thus, the so-called Density Functional Theory (DFT) is used to simplify the problem further and this method relies on two important theorems by Hohenberg and Kohn [14]. The first theorem states that there is a one-to-one relationship between the external potential V_{ext} and the ground-state density $\rho(\overrightarrow{r})$ of a many-electron system. The Hamiltonian is determined by V_{ext}, so all the properties of the many particle system follow from a specification of $\rho(\overrightarrow{r})$. The second theorem states that the lowest energy is obtained if and only if the ground state density $\rho_0(\overrightarrow{r})$ is used in the energy functional. It establishes a variational principle for the ground-state total energy functional $H[\rho] \equiv E_{V_{ext}}[\rho]$ as,

$$E_{V_{ext}}[\rho] = \underbrace{< \psi|\hat{T} + \hat{V}|\psi >}_{F_{HK}[\rho]} + < \psi|\hat{V}_{ext}|\psi >, \tag{2.3}$$

where the Hohenberg-Kohn density functional $F_{HK}[\rho]$ is universal for many-electron systems as it contains information regarding only electrons and not protons. It is postulated in this theorem that at the ground-state density V_{ext}, the ground-state energy functional $E_{V_{ext}}[\rho]$ reaches its minimum value.

2.1.4 Kohn-Sham equations

The Kohn-Sham equations helped turn DFT into a usable and practical tool. The first formulation is defined for the correlation energy, which is the part of the total energy present in the exact solution, but absent in the Hartree-Fock solution, and is given by,

$$V_c = T - T_0, \tag{2.4}$$

where T is the exact kinetic energy functional for the electrons, and T_0 is the kinetic energy functional for a non-interacting electron gas. The second formulation defines the exchange contribution to the total energy that is present in the Hartree-Fock solution, and absent in the Hartree solution. Thus, it is given by,

$$V_x \;=\; V \;-\; V_H, \tag{2.5}$$

where V is the exact electron-electron potential energy functional, and V_H is the Hartree contribution. Thus, the Hohenberg-Kohn functional, from Eqn. (2.3) is written in the following way:

$$\begin{aligned} F_{HK} &= T_0 \;+\; V \;+\; (T \;-\; T_0) \\ &= T_0 \;+\; V \;+\; V_c && from\ (2.4) \\ &= T_0 \;+\; V_H \;+\; V_c \;+\; V_x && from\ (2.5), \end{aligned}$$

where V_{xc} is the exchange-correlation energy functional. The energy functional is thus written as,

$$E_{V_{ext}}[\rho] \;=\; T_0[\rho] \;+\; V_H[\rho] \;+\; V_{xc}[\rho] \;+\; V_{ext}[\rho]. \tag{2.6}$$

The corresponding Kohn-Sham Hamiltonian is given by,

$$\hat{H}_{KS} \;=\; \hat{T}_0 \;+\; \hat{V}_H \;+\; \hat{V}_{xc} \;+\; \hat{V}_{ext}. \tag{2.7}$$

For a system with N particles, the Hamiltonian is solved as a one particle system in its N lowest eigenstates ϕ_i, usually referred to as the Kohn-Sham orbitals. The eigenstates are then determined by solving a Schrödinger-like non-interacting single-particle equation given by,

$$\hat{H}_{KS}\phi_i \;=\; \epsilon_i\phi_i. \tag{2.8}$$

These N equations are the Kohn-Sham equations, and are at the heart of DFT. They can be solved by expanding the single electron wave functions in a basis and diagonalizing the Hamiltonian matrix. Since both V_H and V_{xc} depend on the electron density $\rho(\overrightarrow{r})$, which in turn depends on the wavefunctions ϕ_i being calculated, this problem becomes self-consistent. In the first step, an initial guess of the electron density density ρ_0 is made. With this value, the Hartree operator V_H and exchange-correlation operator V_{xc}, both of which depend on ρ_0, are calculated. Thus, the Hamiltonian H_{KS} is constructed, and the eigenvalue problem is solved to obtain ϕ_i which in turn leads to the calculation of a new density ρ_1. This new density is then compared with the starting

guess ρ_0, and the procedure is repeated again until both become equal.

2.1.5 Generalized Gradient Approximation

This approximation method for the exchange-correlation functional is used for the work presented in this thesis. In this method, the exchange-correlation contribution of every infinitesimal volume not only depends on that volume, but also on the density in neighboring volumes [18]. Thus, the gradient in density between different volumes is also taken into account, and thus it is termed as Generalized Gradient Approximation (GGA).

2.1.6 Solving the Kohn-Sham equations

The single-electron equations to solve are infinite and similar to Eqn. (2.8) irrespective of the method of approximation chosen for the exchange-correlation functional. The wave functions are expressed as,

$$\phi_m \;=\; \sum_{p=1}^{P} c_p^m \phi_p^b, \tag{2.9}$$

where c_p^m are the coefficients to be calculated, and ϕ_p^b is a basis set. The dimensions of the function space in which the wave functions ϕ_m are being searched, are infinite, thus making P infinite. However, it is impossible to work with an infinite basis set, and thus its selection is made in such a way that the resulting functions are close to ϕ_m. The larger the value of P, the more accurate the wave functions, but more time consuming the calculations. Once the selection of a basis set is made, solving Eqn. (2.8) becomes an eigenvalue problem. The choice of a basis set is made in such a way that it is both efficient, i.e., it represents the wave functions as closely as possible, thus requiring lower values of P, and unbiased, i.e., its properties are not influenced by the wave functions. One such basis set that satisfies both of these requirements quite well is the plane wave basis set, which is briefly described in the following section.

2.1.7 Pseudo-potential method

Blöch's theorem defines an eigenfunction as,

$$\psi^{n}_{\overrightarrow{k}}(\overrightarrow{r}) \;=\; \sum_{\overrightarrow{K}} c^{n,\overrightarrow{k}}_{\overrightarrow{K}} e^{i\overrightarrow{k}.\overrightarrow{r}}, \tag{2.10}$$

where $c^{n,\overrightarrow{k}}_{\overrightarrow{K}}$ are coefficients to be determined, $e^{i\overrightarrow{k}.\overrightarrow{r}}$ is a plane wave that contains the periodicity of the lattice, and $\overrightarrow{k}$ is a vector in the first Brillouin zone. Comparing Eqns. (2.9) and (2.10), we thus obtain that m represents (n, $\overrightarrow{k}$), and p represents ($\overrightarrow{k} + \overrightarrow{K}$). However, such a basis set is also almost impossible to calculate accurately. Thus, the potential in regions close to the nuclei, which is its most fluctuating part, is replaced by a pseudo-potential that yields smooth wavefunctions near the atomic nucleus as this part of the solid behaves similarly to free atom electrons. This makes the basis set manageable to calculate for a system. Older pseudopotentials, such as norm-conserving [19] (where electron charge within the core part is equal to that of the actual atom) and ultrasoft [20, 21] pseudopotentials (do not conserve charge but reduce the heights of the peak in the potential that reduces the number of necessary plane waves) can be quite fast and accurate in some cases, and are still in use. The more recent projector augmented wave (PAW) method [18, 22–24] was used for the work presented in this thesis. Ref. [25] presents a comparison of the constructions and performances of these pseudopotentials methods. The PAW method involves the expansion of the wave functions in a plane wave basis set. It retains the full all-electron wave function and charge density while still being computationally efficient. Also, for plane waves, the cut-off can be easily set by limiting the set to k with $k < K_{max}$.

2.2 The CALPHAD method

The thermodynamics of solution phases is first described here as it forms the fundamental basis of the CALPHAD method. Solution is a term referred to a system in a solid, liquid or gaseous state, which exhibits solubility between the various components that make up the system. With relevance to the present work, thermodynamics of two-component systems or binary solutions will be dealt with in the following, noting that the formulation can be extended in a straightforward manner to ternary and higher-order systems.

2.2.1 Ideal mixing

Ideal mixing represents an ideal case of no mixing or interactions in solutions. Statistical thermodynamics defines entropy in terms of disorder in the system. Kelvin and Boltzmann gave a mathematical formulation of this definition as:

$$S \ = \ k \ log_e W, \tag{2.11}$$

where k is Boltzmann's constant and W is a measure of disorder in the system. If in a binary solution, out of a total of N sites n sites are occupied by A-type of atoms and the rest, $(N \ - \ n)$ sites, by B-type atoms as shown in Fig. 2.1.

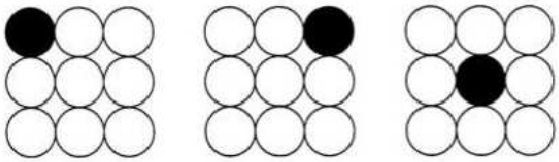

Figure 2.1: Schematic representation of random mixing of A and B atoms/molecules in a binary solution (adapted from Ref. [16]).

The disorder or probability of distribution in this case is given by,

$$W \ = \ \frac{N!}{n!(N \ - \ n)!}. \tag{2.12}$$

The entropy of this solution is then given by,

$$S \ = \ k \ log_e \frac{N!}{n!(N \ - \ n)!}. \tag{2.13}$$

After applying Stirling's approximation and subsequent simplifications, the entropy change for ideal mixing is given by,

$$S \ = \ - R(x_a log_e x_a \ + \ x_b log_e x_b). \tag{2.14}$$

Thus, the Gibbs energy of mixing in case of no interactions between constitutive elements is given by,

$$G_{mix}^{ideal} \;=\; RT(x_a log_e x_a \;+\; x_b log_e x_b). \tag{2.15}$$

2.2.2 Non-ideal mixing

In reality, there is always some kind of interactions between different atom types in a solution. These interactions can either be attractive or repulsive in nature. The effects of such interactions are incorporated via the excess mixing energy term, G_{mix}^{xs}, which is modeled in the simplest way according to the regular solution model:

$$G_{mix}^{xs} \;=\; \Omega\; x_a x_b, \tag{2.16}$$

where Ω is a regular solution parameter, and its sign depends on the nature of chemical interactions, positive for repulsive and negative for attractive interactions. The tendency to form a miscibility gap or two-phase structures in binary solution phases increases with an increase in magnitude of this regular solution parameter. In the case of attractive interactions or negative values of the regular solution parameter, the tendency is to form continuous solid solutions. Equations (2.15) and (2.16) combine to give the Gibbs energy of solution,

$$G_{mix} \;=\; RT(x_a log_e x_b \;+\; x_b log_e x_b) \;+\; \Omega\; x_a x_b. \tag{2.17}$$

However, in the presence of crystallographically distinct phases, the Gibbs energy at end-points of the mixing curve have to be calculated, thus requiring that reference states be defined for the pure components. The Gibbs energy is then written as,

$$G \;=\; G_{ref} \;+\; G_{mix}^{ideal} \;+\; G_{mix}^{xs}, \tag{2.18}$$

where G_{ref} is given by,

$$G_{ref} \;=\; \sum_i x_i G_i^o, \tag{2.19}$$

where x_i is the mole fraction of component i, and G_i^o is the Gibbs energy of the phase for pure component i.

2.2.3 Thermodynamic models

Solution phases are modeled via various methods, two of which are described here.

2.2.3.1 Random substitutional model

In this model, the components occupy crystal sites in a random manner rather than in an ordered manner, as shown in Fig. 2.2. Thus, gases, liquids and some metallic solid solutions are represented very well by this model.

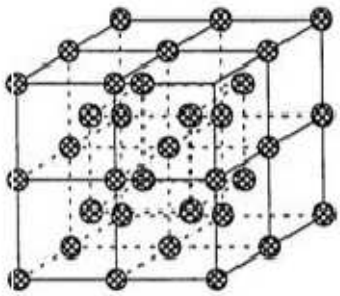

Figure 2.2: Random occupation of sites on a bcc structure (adapted from Ref. [16]).

In the present work, the liquid, and solid solution phases (that are non-stoichiometric) phases are modeled in this manner. One of the simplest non-ideal models is the regular solution model which considers no dependence of the nature of interactions between the components on the composition of the solution. The Gibbs free energy expression of such a model is given similar to Eqn. (2.18),

$$G_m^{\phi} \;=\; \sum_{i=A,B} x_i \; {}^{o}G_i^{\phi} \;+\; RT \sum_{i=A,B} x_i log_e x_i \;+\; x_A x_B L_{A,B}^{\phi}, \tag{2.20}$$

where G_m^{ϕ} denotes the Gibbs energy of phase ϕ, x_i is the mole fraction of component i, ${}^{o}G_i^{\phi}$ defines the Gibbs energy of the phase containing the pure component i obtained from the SGTE database [26], and $L_{A,B}^{\phi}$ is an interaction parameter that incorporates the effects of non-ideal mixing. To account for dependencies on changes in composition, this parameter is expanded using Redlich-Kister formalism [27] as,

$$L_{A,B}^{\phi} \;=\; \sum_{v} L_{A,B}^{\phi} (x_A \;-\; x_B)^v. \tag{2.21}$$

The above equation for G^{xs}_{mix} is considered a regular solution when $v = 0$ and non-regular solution when $v > 1$. Th binary interaction parameter is made temperature-dependent using,

$$ {}^{v}L^{\phi}_{A,B} \;=\; {}^{v}A \;+\; {}^{v}BT, \tag{2.22} $$

where ${}^{v}A$ and ${}^{v}B$ are model parameters to be optimized.

2.2.3.2 Sublattice model

This method of modeling phases can be applied to a variety of phase types such as interstitial and solution phases. The sublattice model can be visualized as consisting of interlocking sublattices as shown in Fig. 2.3.

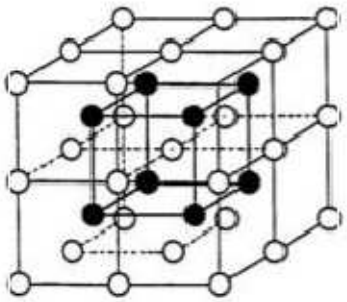

Figure 2.3: A bcc structure shown with preferential occupation of sites by atoms on the two simple cubic sublattices (adapted from Ref. [16]).

Its crystalline nature does not particularly represent a crystal structure within its general definition; however, certain external terms and conditions can be imposed to simulate special structure types. In this method it is necessary to define the fractional site occupation of each component in all the sublattices, which is given by,

$$ {}^{s}y_i \;=\; \frac{n^s_i}{N^s}, \tag{2.23} $$

where n^s_i is the number of atoms of component i on sublattice s. In many cases, when vacancies are involved and become important to model a phase, such as an intermetallic phase, the site occupation is modified as,

$$ {}^{s}y_i \;=\; \frac{n_i^s}{n_{Va}^s \;+\; \sum_i n_i^s}, \tag{2.24} $$

where n_{Va}^s gives the number of vacancies on sublattice s. The Gibbs energy reference state is obtained when only pure components can be considered as existing on each sublattice, and is given by,

$$ G_m^{ref} \;=\; \sum_{I0} P_{I0}(Y)^o G_{I0}^{\phi}, \tag{2.25} $$

where P_{I0} represents the corresponding product of site fractions when each sublattice is occupied by only one component. In general, P_{IZ} is the site fraction product when only one sublattice contains Z components and the remaining sublattices are occupied by one component. G_{I0}^{ϕ} is the Gibbs energy of the compound defined by I in phase ϕ. For example, if a two-sublattice phase is modeled as $(A,B)_1(C,D)_2$, where A, B, C and D are the components of this phase, the Gibbs energy reference state is written as,

$$ G_m^{ref} \;=\; y_A y_C G_{AC}^o \;+\; y_A y_D G_{AD}^o \;+\; y_B y_C G_{BC}^o \;+\; y_B y_D G_{BD}^o. \tag{2.26} $$

The ideal entropy of mixing in this case is given by,

$$ G_{mix}^{ideal} \;=\; RT \sum_s N^s \sum_i y_i^s log_e y_i^s. \tag{2.27} $$

Vacancies are included in the fractional site occupation term, y_i^s. The ideal entropy term in the above expression includes all possible configuration contributions by all components mixing in each sublattice. The Gibbs excess energy of mixing for the two-sublattice system described previously as $(A,B)_1(C,D)_2$, is given by,

$$ G_{mix}^{xs} \;=\; y_A^1 y_B^1 L_{A,B:*}^0 \;+\; y_C^1 y_D^1 L_{*:C,D}^0. \tag{2.28} $$

The above equation represents the regular solution format, and $L_{A,B:*}^0$ and $L_{*:C,D}^0$ are the regular solution mixing parameters for each sublattice that are independent of the site occupation on the other sublattice. The sub-regular format includes the site occupation on the other sublattice as,

$$G^{xs}_{mix} \;=\; y^1_A y^1_B y^2_C L^0_{A,B:C} \;+\; y^1_A y^1_B y^2_D L^0_{A,B:D} \;+\; y^1_C y^1_D y^2_A L^0_{A:C,D} \;+\; y^1_C y^1_D y^2_B L^0_{B:C,D}. \qquad (2.29)$$

Similar to the formalism in the case of the random solution model, the parameters are made composition dependent as,

$$L^0_{A,B:C} \;=\; y^1_A y^1_B y^2_C \sum_v L^v_{A,B:C} (y^1_A \;-\; y^1_B)^v. \qquad (2.30)$$

The other parameters are modeled in a similar manner. The final Gibbs excess energy of mixing is given by,

$$G^{xs}_{mix} \;=\; \sum_{Z>0} \sum_{IZ} P_{IZ}(Y) L^{\phi}_{IZ}. \qquad (2.31)$$

Thus, the total Gibbs energy of this phase is obtained by combining the reference energy, ideal entropy contribution and excess energy contribution from Eqns. (2.25), (2.27), and (2.31), respectively, which is then given by,

$$G^{\phi}_m \;=\; \sum_{I0} P_{I0}(Y)\, {}^oG^{\phi}_{I0} \;+\; RT \sum_s N^s \sum_i {}^s y_i log_e \, {}^s y_i \;+\; \sum_{Z>0} \sum_{IZ} P_{IZ}(Y) L^{\phi}_{IZ}. \qquad (2.32)$$

2.2.4 Evaluation of Gibbs energy parameters

After having made a decision of the model for the Gibbs energy of each phase to be considered for a given system, and entering all experimentally measured quantities and data from DFT calculations in an input file (.POP), the next step in the CALPHAD method is the evaluation of the parameters. This is carried out using an optimizer code that essentially revolves around Gibbs energy minimization. This type of code is based on the aim of reducing the statistical error between the experimental data and the calculated phase equilibria as much as possible.

2.2.4.1 Minimization procedure for single-phase equilibria

In the case of solution phases where enthalpies and entropies are temperature dependent, the Gibbs energy minimization is carried out by minimizing the function,

$$\Delta G^{1\phi} \;=\; \sum_i x_i^{\phi} \overline{G}_i^{\phi} \;-\; G^{\phi} \;=\; 0 \tag{2.33}$$

A Newton-Raphson method is used for rapid convergence. An initial temperature is chosen and both $\Delta G^{1\phi}$ and $\Delta G^{1\phi}/dT$ are calculated and then used to estimate a new temperature where $\Delta G^{1\phi}$ is expected to be equal to zero as shown in Fig. 2.4. If this new temperature does not satisfy the convergence condition, a new temperature is chosen. This process is repeated until $\Delta G^{1\phi}=0$.

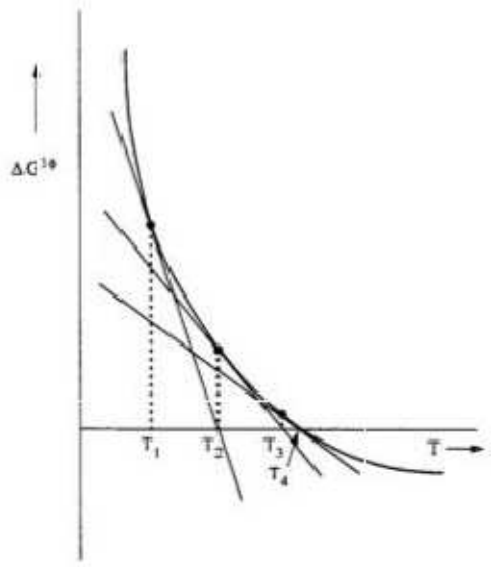

Figure 2.4: Schematic diagram showing the process of calculating the temperature at which $\Delta G^{1\phi}=0$ (adapted from Ref. [16]).

2.2.4.2 Minimization procedure for two-phase equilibria

The following mass balance equations will be utilized in the calculation of a two-phase equilibria,

$$N_i \;=\; \sum_{\phi} N_i^{\phi} \tag{2.34}$$

and,

$$\sum_{i} N^i \;=\; M, \tag{2.35}$$

where N_i is the total number of mole of component i in the system, N_i^{ϕ} is the number of moles of component i in phase ϕ, and M is the total number of moles in the system.

The following is a brief description of the general minimization procedure: at first, the phase equilibrium is assumed to be single-phase. Then, an arbitrary amount of the second phase is introduced in the system, and in accordance with the mass balance equations a corresponding change is made in the composition of the first phase followed by the calculation of the Gibbs energy. The composition of this phase is then kept constant and the amount of the second phase is then varied with a corresponding change in its composition, to maintain mass balance, so that the Gibbs energy is minimized, as shown in Fig. 2.5.

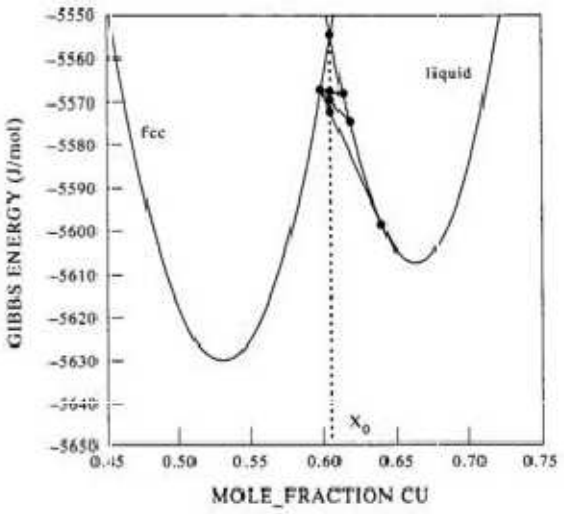

Figure 2.5: First stage in the iteration process of Gibbs energy minimization of a Cu-Ni alloy at composition x_0 in Cu, and at 1523 K (adapted from Ref. [16]).

The selection of the amount of the second phase to be varied can be made by calculating the second derivative of G with respect to N^{liq} to obtain the composition at which $dG/dN^{liq}=0$, as shown in Figs. 2.6 and 2.7.

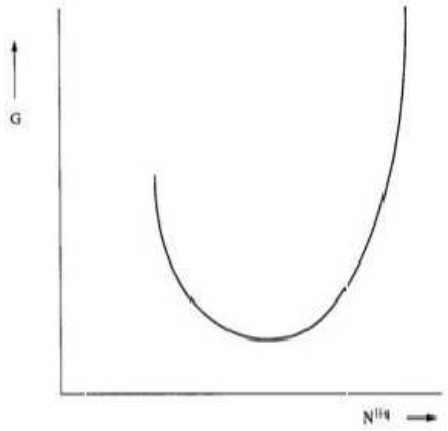

Figure 2.6: Gibbs energy versus N^{liq} in an alloy shown schematically (adapted from Ref. [16]).

This process is repeated until the Gibbs energy is minimized. The same procedure is then applied by varying the amount and composition of the first phase as shown in Fig. 2.8(a). This cycle is repeated as shown in Fig. 2.8(b) and 2.8(c) until a minimum is obtained in the Gibbs energy and the convergence criteria is satisfied.

2.2.4.3 Stepping and mapping

The previous procedures are for the calculation of equilibrium points at specific composition, temperature and pressure. However, for phase diagram calculations when changing a particular condition, such as composition or temperature in the present case, a procedure known as stepping is employed. In this process, a property is increased in small amounts or steps, and then the stability of the phase is checked at this step. If the phase is stable at that particular step, it is used as a starting point for the next step. This process is repeated until the conditions are not satisfied. Mapping is the process by which a phase diagram is plotted and employs the calculated results of the stepping code to map a phase boundary. Binary phase diagrams have two degrees of freedom that are most commonly represented by the temperature and composition.

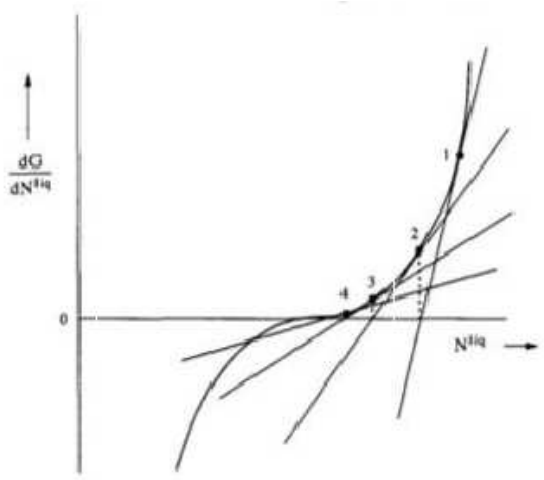

Figure 2.7: Calculation of the second derivative of G with respect to N^{liq} to obtain the minimum in Gibbs energy (adapted from Ref. [16]).

The requirements from a calculation method must be to reduce the degrees of freedom, calculate the Gibbs energy of the system, and use some iterative technique to minimize the Gibbs energy. Also, the robustness and the speed of the calculations depend heavily on the choice of starting guesses for the model parameters. Even though the calculation methods being used might be global minimization programs, there is always a possibility for the calculation to get stuck at a local minimum, thus giving an incorrect equilibrium result. Therefore, it is always recommended to have some prior knowledge of the phase diagram equilibria. This problem is most evident in the case of phases that have a miscibility gap. In case of availability of prior information on the miscibility information, such a phase is then given start points for both #1 and #2 phases (that form the miscibility gap) by the program and it ensures the convergence accounts for both minima. However, in a generalized environment, this method would fail if unknown miscibility gaps were present or if there was an order/disorder transition associated with the phase. Thus, some prior knowledge of miscibility gap or ordering is necessary to obtain reasonable accuracy and speed of execution.

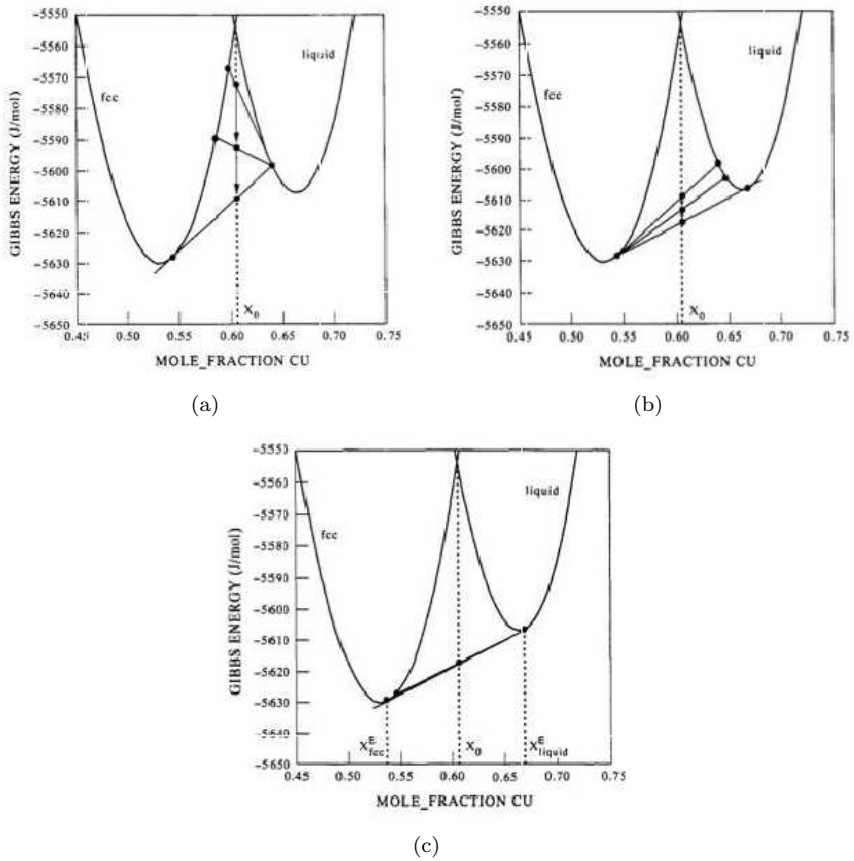

Figure 2.8: Second, third, and fourth stage in the iteration process of Gibbs energy minimization of a Cu-Ni alloy with composition x_0 in Cu, and at 1523 K (adapted from Ref. [16]).

2.2.4.4 The PARROT programme

The PARROT module [28] is integrated with the Thermo-Calc package [29] and is essentially based on the following governing principles:

- Establish a criterion for best fit: This criterion is based on a maximum likelihood principle where a likelihood function is chosen and must be maximized to obtain the best estimates of the model parameters. Simplification of this process is made by assuming that the joint probability density function of all the experimental data is Gaussian in form, and that there is no dependence or coupling between different experimental measurements.

- Data separation based on accuracies: The PARROT module allows the user to input experimental data that are significantly inaccurate compared with their true values in addition to the data which are free from such inaccuracies. Dependent and independent variables: Both types of variables can be used in the optimization process of the PARROT module. Dependent variables are those that describe the responses of the system to prescribed conditions, whereas independent variables define the equilibrium conditions. The calculation of the Gibbs energies for different phases and the determination of equilibria are then performed by the Poly-3 module of the Thermo-Calc software that is coupled with PARROT. State variables such as temperature, pressure, and chemical potentials are treated as independent variables and are preselected to define the equilibrium conditions. Dependent variables, or responses of the system, are then written as functions of the independent variables and the model parameters. This makes it possible to use almost any type of experimental information in the evaluation of the model parameters. A significant advantage of using the CALPHAD method is that various other properties can be automatically obtained after the calculation procedure and can also be plotted as functions of the state variables.

In developing the thermodynamic model of the PbTe phase in the Pb-Te system (Chapter 3), the optimization process was started with a small number of iterations and very low statistical weights assigned to experimental and calculated data. The liquid and the PbTe phases were first entered in the optimization process. The weights were increased appropriately during the optimization process to be within an acceptable range of the input data. To aid in the calculation of a global equilibrium, another constraint that was used was the driving force for the formation of a particular phase. Driving force is defined as the affinity between reacting chemical species, and its magnitude gives the equilibrium of a phase at particular composition and temperature. At particular temperature and composition it is negative for the stable phase, and positive for the phases that are not at equilibrium under those conditions. Also, the optimization was carried out until a balance was achieved between different sets of input data, which in the present work are the solidus, liquidus equilibrium lines, the formation enthalpies of the liquid and PbTe phases, and the defect formation energies.

Chapter 3

Ab initio study of intrinsic point defects in PbTe: an insight into phase stability through defect thermodynamics

Adapted from Ref. [30] with permission from Elsevier.

3.1 Introduction

One solution to the rapidly changing climate and global warming is to extract the available energy (or exergy) from waste heat, and convert it to electricity. Devices that perform such an operation are called thermoelectric generators, and materials used in these devices are known as thermoelectric (TE) materials. The lead chalcogenide salt PbTe, one of the most widely studied TE materials, is a IV-VI semiconductor with a small band-gap and is the best performing TE material for mid-temperature power generation (200-600^{0}C) [13]. It exhibits both types of conductivity depending on the growth conditions- n-type (electrons) in a Pb-rich environment and p-type (holes) in a Te-rich environment [31–37], which makes it particularly advantageous since TE devices consist of both n- and p-type legs coupled together. Furthermore, tuning the carrier densities by adjusting the defect/dopant concentrations not only maximizes zT, but also gives control over where its peak occurs in the temperature space [13]. This coupling between carrier concentration, defects/dopants, and zT makes it important to understand the defect chemistry of a material for its application as

a thermoelectric material.

In a previous study by Ahmad *et al* [38], the physics and electronic structure of vacancy and impurity induced deep defect states in PbTe was investigated by *ab initio* calculations. Another study by Xiong *et al* [39] investigated the impact of dopants on the density of states (DOS) and band structures between pure and extrinsically doped PbTe. Both these works have not investigated the energetics of different types of point defects in intrinsic PbTe. In a recent publication by Wang *et al* [40], spin-orbit coupling (SOC) calculations were performed that result in a band gap of 0.11 eV, which is in better agreement with the room temperature experimental band gap of 0.31 eV. However, it was found that the fermi level is positioned where Te vacancy V_{Te}^{+2} donor defects for Pb-rich and Te substitutional Te_{Pb}^{+2} donor defects for Te-rich conditions are most stable, thus leading to n-type conductivity for both growth conditions. p-type/hole conductivity for Te-rich conditions was found to only occur for a limited set of Te chemical potential. This result is inconsistent with the well-known observance of both electron and hole conductivity in PbTe from numerous experimental works. Additionally, no comparison with experimental results on carrier concentrations is made. Thus, in this work, we investigate the role of intrinsic point defects in the conductivity and doping behavior of PbTe within the framework of Density Functional Theory (DFT). Specifically, we study the stability of vacancy, anti-site, and interstitial defects by calculating their formation energies for both Pb-rich and Te-rich growth conditions. Defects with the lowest formation energies will help us attribute the origins of n-type and p-type conductivity in PbTe to that specific type of point defect type.

The phase diagram of Pb-Te exhibits a very small range of non-stoichiometry in the PbTe phase to the order of $x = 10^{-4}$ on both sides of the stoichiometric line at $x = 0.50$ [31–37] due to the presence of defects, which in turn leads to the n- and p-type conductivity in this phase. A previously developed thermodynamic model of this system by Gierlotka *et al* [41] describes the Gibbs energy of this compound using the Wagner-Schottky defect model [42] that assumes anti-site defects - $(Pb, Te)_1$:$(Te, Pb)_1$ to cause the very small non-homogeneity range. However, as we shall see later, it is actually the vacancy defects that have the lowest formation energy and hence are the most stable among the different types of defects. Thus, in this work, we use the CALculation of PHAse Diagrams (CALPHAD) method [16] to modify the description of the PbTe phase, and then use the

DFT vacancy formation energy values in its Gibbs free energy expressions, which result in solubility lines that agree very well with experimental data. This approach of using information from DFT to select a particular type of phase model and use the DFT calculated defect formation energies in the Gibbs free energy descriptions to calculate a phase diagram makes the process of building thermodynamic models more physical. More importantly, in the field of TE materials where dopants are added in small concentrations to fine tune TE properties, this methodology helps determine the solubility ranges of those dopants in the base material, and is critical to the future development of unexplored phase diagram databases.

In the next section we first discuss the method used to calculate defect formation energies, and the correction schemes employed to account for using finite-sized supercells with periodic boundary conditions to model dilute defects. We also briefly describe the CALPHAD method, and the vacancy defect model used to model the PbTe phase in this section. The results obtained for both Pb-rich and Te-rich conditions are shown and discussed in Section 3.3 along with the calculated carrier concentrations that are compared with experimental data. The thermodynamic model for the PbTe system and the resulting thermodynamic data are compared with that from literature in the same section. Finally, concluding remarks are presented in Section 3.4.

3.2 Methodology

3.2.1 Defect thermodynamics

The stability of a defect is determined by its formation energy which, according to the Zhang-Northrup supercell formalism [43] for a defect D of charge q, is given by

$$\Delta H_{d,q} = [E_{d,q} - E_H] + \sum_{\alpha} n_\alpha(\mu_\alpha^0 + \Delta\mu_\alpha) + q(E_{VBM} + \Delta V_{PA} + \mu_e) + \Delta E_{IC}, \quad (3.1)$$

where $E_{d,q}$ and E_H are the total energies of the defect containing supercell and the ideal supercell, respectively, and represent the bond energy cost due to the creation of a defect. The atomic chemical potentials μ_α is the energy of the atomic reservoir of the atoms either removed ($n_\alpha = +1$) or added (n_α = -1) to the host supercell in the formation of a defect. It reflects the crystal growth

conditions as $\mu_\alpha = \mu_\alpha^0 + \Delta\mu_\alpha$, where μ_α^0 is the chemical potential of an element in its standard reference state (the phase in equilibrium at conditions of room temperature and pressure, T = 298 K and P = 1 atm), and $\Delta\mu_\alpha$ is the change in chemical potential of an element with reference to its standard state. For a maximally rich growth environment of an element, $\Delta\mu_\alpha = 0$. For example, Pb-rich/Te-poor growth environment in PbTe is represented by $\mu_{Pb} = \mu_{Pb}^0$ ($\Delta\mu_{Pb} = 0$). In these conditions, the chemical potential of Te is reduced to below the value for its standard reference state value, i.e., $\mu_{Te} < \mu_{Te}^0$ ($\Delta\mu_{Te} < 0$). Its exact value is given by the condition that correlates the elemental chemical potential for the stability of this phase,

$$\mu_{Pb} + \mu_{Te} = \mu_{PbTe}, \tag{3.2}$$

where μ_{PbTe} is the chemical potential of the defect-free PbTe compound. The above condition is true in the case of PbTe since there are no other competing phases in the phase stability regions between the elemental reference phases and the PbTe phase.

For charged defects ($q \neq 0$), the second to last term in Eqn. (3.1), i.e., $q(E_{VBM} + \Delta V_{PA} + \mu_e)$, represents the energy cost of exchanging electrons with the electron reservoir. E_{VBM}, the valence band maximum (VBM) energy corresponds to the energy of the highest occupied level. It is the cost of removing an electron from the top of the valence band, and in this work the energy difference between a neutral defect-free supercell and the supercell with a hole is used to approximate the value of E_{VBM}.

The creation of a neutral defect in a supercell causes the band energy levels to shift relative to the levels in the defect-free supercell. Furthermore, in the case of creation of a charged defect, the charge neutrality condition is violated, which causes the Coulomb potential to diverge. This is avoided by setting $V_{el}(G = 0) = 0$, which is equivalent to introducing a compensating uniform background charge, and only affects the potential but not the charge density in the calculation. Thus, the energy levels of the charged defect cell do not reference to the potential of the host cell, and the defect energy levels need to be re-aligned to the host energy levels using a potential alignment (PA) term ΔV_{PA} that is added to the defect formation energy (in Eqn. (3.1) above) and is calculated as [44],

$$\Delta E_{PA} \;=\; q.\Delta V_{PA} \;=\; q.(V^r_{d,q} \;-\; V^r_H), \tag{3.3}$$

where ΔV_{PA} is the potential alignment between the spherically-averaged electrostatic potentials of the defect ($V^r_{d,q}$) and the host (V^r_H) cells far from the defect site so as to avoid including any spurious chemical interactions with the defect. In this work, it is found that ΔE_{PA} ranges between 0.25 eV to 0.05 eV for the various defects. Finally, the electron chemical potential μ_e term in Eqn. (3.1) is the additional energy of electrons in our system, and is set to range between the VBM and CBM (conduction band minimum) for plots showing the variation of defect formation energies as functions of electron chemical potential. Its value is fixed as a function of temperature by solving the charge neutrality condition, as explained later in Section 3.1.

The use of periodic boundary conditions in DFT causes charged defects to be periodically and infinitely repeated in neighboring supercells. These periodic images of defects result in electrostatic interactions between the charges, and defect concentrations in the order of tenths of a percent, which is significantly higher than that found in semiconductors (parts-per-million). Also, the computing demands posed by DFT limits the size of supercells that can be used to perform calculations on. Thus, in order to model a true isolated charge defect in a size limited supercell in non-degenerate conditions, an image charge correction energy term ΔE_{IC} is added to the defect formation energy in Eqn. (3.1) above. It is typically written in the form of a multipole expansion given by Makov and Payne [45],

$$\Delta E_{IC} \;=\; \frac{q^2\alpha}{2\epsilon L} \;+\; \frac{2\pi q Q_r}{3\epsilon L^3} \;+\; O(L^{-5}). \tag{3.4}$$

The first two terms are the monopole and quadrupole corrections where α is the Madelung constant of the supercell lattice (1.75 for the rock salt NaCl structure of PbTe), L is distance between defects, ϵ is the static dielectric constant which is calculated to be equal to 397 (including ionic contributions) for PbTe using density functional perturbation theory as implemented in VASP [46–48], and is in good agreement with available experimental data (412 $\pm$ 40) [49]. Q_r is the second radial moment of the charge density, and it has been found [44] that the quadrupole term is typically $\approx$ -35% of the monopole term which is implemented here. It is also found from Ref. [44] that these terms are not affected by the choice of the exchange-correlation functional. Higher order terms

$O(L^{-5})$ are neglected due to their minimal contributions. Altogether, the image charge correction term is calculated to have a maximum value of ≈ 0.01 eV in this work for q $\pm$ 2 charges.

3.2.2 Computational details

DFT calculations are performed with the Vienna Ab-initio Simulation Package (VASP) [50–53] using the Projector Augmented Wave (PAW) method [22–24] and generalized gradient approximation (GGA) with the exchange-correlation functional of Perdew, Burke, and Ernzerhof (PBE) [18]. The $5d^{10}6s^26p^2$ electrons of Pb and $5s^25p^4$ electrons of Te were treated as valence states to generate the PAW potentials. The primitive cell of PbTe contains 2 atoms, and all calculations are performed on a 5 x 5 x 5 supercell of the primitive cell that contains 250 atoms. , and is shown in Fig. **??** The cutoff energy of plane wave basis was set to 400 eV, and integrations over the first Brillouin zone were made using a k-point grid set of 2 x 2 x 2 generated according to the Monkhorst-Pack scheme [54]. Unit cell parameters and atomic positions were relaxed based on an energy convergence criteria of 10^{-4} eV, and a final static calculation was performed for an accurate total energy.

3.2.3 Thermodynamic models for the CALPHAD method

The thermodynamic models employed in this work are based on previous assessments by Gierlotka *et al* [41, 55] on the Pb-Te system. In these expressions, the Gibbs energies G_m^ϕ of each phase ϕ taking part in the equilibria are defined using the models described below. x_i is the molar fraction of component i, and ${}^oG_i^\phi$ is the reference Gibbs energy of the component i making up the phase at 298 K and 1 atm that is obtained from the Scientific Group Thermodata Europe (SGTE) database [26].

3.2.3.1 Liquid

The liquid phase of the Pb-Te system exhibits a sharp minimum versus composition in its enthalpy of mixing near the PbTe stoichiometry that indicates strong short-range order interactions [56], which has also been seen in experimental measurements on its conductivity [57] and viscosity [58]. Thus, following Ref. [55], in this work we have also used the associate model [59] to describe this phase. In CALPHAD terminology, the term “associate” is used to denote an association between

unlike atoms when the attractive forces between the atoms are not strong enough to form a stable chemical molecule. According to this model, the Gibbs energy per mole of atoms of such a phase is given by,

$$\begin{aligned} G_m^{Liq} &= G_{ref} \ + \ \Delta G_{mix}^{ideal} \ + \ \Delta G_{mix}^{xs} \\ &= \frac{[\sum_i x_i \ {}^oG_i^{Liq} \ + \ RT\sum_i x_i \ln x_i \ + \ \sum_i \sum_{j>1} x_i x_j \sum_v \ {}^vL_{i,j}^{Liq}(x_i \ - \ x_j)^v]}{(1 \ + \ x_{PbTe})}, \end{aligned} \tag{3.5}$$

where i, j = Pb, Te, and PbTe, R is the gas constant, and T is the temperature. ${}^vL_{i,j}^{Liq}$ is called the non-ideal interaction parameter, and is part of the excess Gibbs energy of mixing term ΔG_{mix}^{xs}, which includes temperature dependency of sources of entropy (non-ideal configurational, vibrational, and electronic) apart from the ideal configurational entropy ΔG_{mix}^{ideal}. The temperature dependency in these parameters is included by expanding them to be,

$${}^vL_{i,j}^{Liq} \ = \ {}^vA_{i,j}^{Liq} \ + \ {}^vB_{i,j}^{Liq}.T, \tag{3.6}$$

where ${}^vA_{i,j}^{Liq}$ and ${}^vB_{i,j}^{Liq}$, the only unknowns in Eqn. (3.5) above, are user-defined parameters that are fitted in the CALPHAD method to experimental and/or *ab initio* data on phase equilibria/diagram and thermodynamic properties.

3.2.3.2 PbTe

The PbTe structure is of rock salt NaCl structure with space group $Fm\overline{3}m$ (no. 225). As mentioned earlier in the Introduction, the small non-stoichiometry in the PbTe phase that is caused by defects is modeled using the Wagner-Schottky sublattice model [42], but now using vacancies as defects, i.e., (Pb, Va)$_1$:(Te, Va)$_1$ instead of anti-site defects assumed before [41]. The Gibbs energy of this phase is given by,

$$G_m^{PbTe} \ = \ \sum_{I0} P_{I0}(y) {}^oG_{I0}^{\phi} \ + \ RT\sum_s N^s \sum_i \ {}^sy_i \ln \ {}^sy_i \ + \ \sum_{Z>0} \sum_{IZ} P_{IZ}(y) L_{IZ}^{\phi}, \tag{3.7}$$

where P_{I0} is a product of sublattice site fractions when each of them is occupied by only one component, N^s is the number of sites on sublattice s, P_{IZ} is also a product of sublattice site

fractions but when only one sublattice contains Z components and the remaining are occupied by one component, and ${}^{s}y_i$ is called the site fraction defined by,

$$ {}^{s}y_i \;=\; \frac{n_i^s}{N^s}, \tag{3.8} $$

where n_i^s is the number of atoms of component i on sublattice s. For the vacancy model of the PbTe phase, this simplifies to,

$$ \begin{aligned} G_m^{PbTe} \;=\; & y_{Pb}^{I} y_{Te}^{II}\; {}^{0}G_{Pb:Te}^{PbTe} \;+\; y_{Pb}^{I} y_{Va}^{II}\; {}^{0}G_{Pb:Va}^{PbTe} \;+\; y_{Va}^{I} y_{Te}^{II}\; {}^{0}G_{Va:Te}^{PbTe} \;+\; y_{Va}^{I} y_{Va}^{II}\; {}^{0}G_{Va:Va}^{PbTe} \\ & +\; 0.5RT(y_{Pb}^{I} \ln y_{Pb}^{I} \;+\; y_{Va}^{I} \ln y_{Va}^{I}) \;+\; 0.5RT(y_{Te}^{II} \ln y_{Te}^{II} \;+\; y_{Va}^{II} \ln y_{Va}^{II}) \;+\; \Delta G_{mix}^{xs}, \end{aligned} \tag{3.9} $$

where it is assumed ${}^{0}G_{Va:Va}^{PbTe} \;=\; 0$ due to the unphysical character of having vacancies completely occupy both the sublattices. ${}^{0}G_{Pb:Te}^{PbTe}$, ${}^{0}G_{Pb:Va}^{PbTe}$, and ${}^{0}G_{Va:Te}^{PbTe}$ are given by,

$$ \begin{aligned} {}^{0}G_{Pb:Te}^{PbTe} \;&=\; {}^{o}G_{Pb}^{fcc} \;+\; {}^{o}G_{Te}^{hex} \;+\; X_1 \;+\; Y_1.T \\ {}^{0}G_{Pb:Va}^{PbTe} \;&=\; {}^{o}G_{Pb}^{fcc} \;+\; X_2 \;+\; Y_2.T \\ {}^{0}G_{Va:Te}^{PbTe} \;&=\; {}^{o}G_{Te}^{hex} \;+\; X_3 \;+\; Y_3.T. \end{aligned} \tag{3.10} $$

X_i and Y_i are user-defined parameters, that along with ${}^{v}A_{i,j}^{Liq}$ and ${}^{v}B_{i,j}^{Liq}$ in the expansion of the excess Gibbs energy term ΔG_{mix}^{xs} (similar to as in Eqn. (3.6)), are the only unknowns. ${}^{0}G_{Pb:Va}^{PbTe}$ and ${}^{0}G_{Va:Te}^{PbTe}$ are related to the vacancy formation energies on the Te and Pb sublattices, respectively, and the temperature-independent parameters X_2 and X_3 in these expressions are fixed to the vacancy defect formation energies calculated from DFT. The rest of the parameters in Eqn. (3.10) are fitted to experimental data on the phase diagram and thermodynamic data.

3.2.3.3 Fcc_A1, Hexagonal_A8

The standard reference phases of Pb and Te, fcc and hexagonal, respectively, have been modeled with no solubilities as previous experimental results indicate. Thus, the Gibbs energies of these phases are described by the reference energies ${}^{o}G_{Pb}^{fcc}$ and ${}^{o}G_{Te}^{hex}$.

3.3 Results and Discussion

3.3.1 Defect stability

The calculated lattice constant of 6.559 Å and formation enthalpy of -0.406 eV/atom of PbTe are in good agreement with the experimental values of 6.462 Å [60], and ≈ -0.36 eV/atom [61, 62], respectively. However, the calculated direct band gap of 0.82 eV at the L point using GGA overestimates the value of 0.31 eV obtained from recent experiments [63]. On the other hand, our calculations show that the hybrid HSE functional coupled with SOC leads to an upward shift of the topmost valence band and a downward shift of the lowest conduction band, leading to a reduction in the gap to 0.28 eV (for a 0.3 $Å^{-1}$ screening length and 25% Hartree Fock exchange mixing), whereas just including SOC effects results in a gap of 0.08 eV. Both these methods are computationally prohibitive with current supercomputers to be applied to the 250 atom defect supercells used in this work. HSE calculations on smaller supercells would be plausible (but still very expensive); however, the effect of approximations in image-charge and potential alignment correction schemes would then become more pronounced due to the relatively small size of these supercells, thus negating the beneficial effect of using an accurate band gap. This is why a vast majority of defect calculations still employ PBE (or other semi-local or local) functionals coupled with band gap correction schemes, as well documented in the literature [64, 65]. Thus, we have just resorted to a well-documented methodology of using GGA for defect calculations together with a band-gap correction scheme that is discussed later in this section.

Three types of point defects are considered in this work on each of the Pb and Te sublattices that make up the PbTe rock salt structure: vacancies (V_{Pb}, V_{Te}), anti-sites (Pb_{Te}, Te_{Pb}), and interstitials (Pb_i, Te_i), all in neutral and charged states ranging from -2 to +2. Formation energies of every defect in each charge state $\Delta H_{d,q}$ are calculated using Eqn. (3.1), taking into account the image charge and potential alignment corrections that are calculated using methods explained in Section 2. Their concave hulls are plotted in Fig. 3.1 for both Pb-rich and Te-rich growth conditions so as to show only the lowest energy defect as a function of electron chemical potential or Fermi level μ_e.

The charge state of the defect corresponds to the slope of these lines. As seen in this figure, the most stable defects with the lowest formation energy for Pb-rich conditions are Pb and Te vacancies

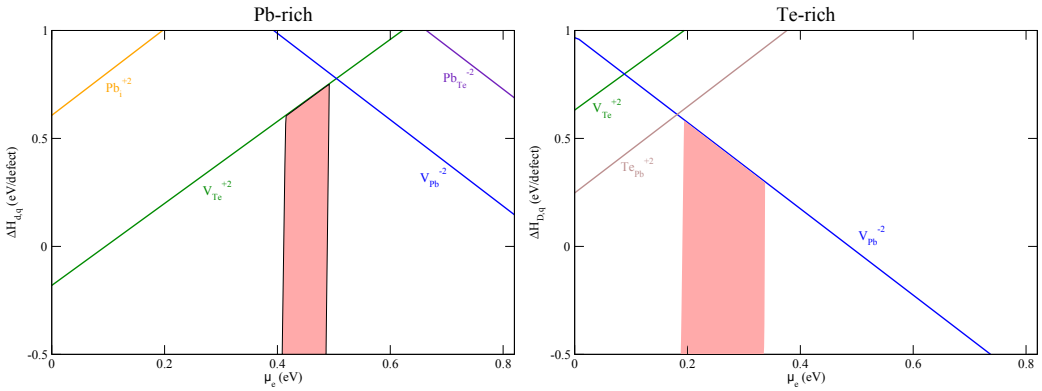

Figure 3.1: (Color online) Calculated defect formation energies, $\Delta H_{d,q}$ in PbTe as a function of Fermi level, μ_e in Pb-rich and Te-rich conditions. Slope of lines corresponds to the charge state of the defect, and shaded areas represent the range of calculated equilibrium Fermi levels shown in Fig. 3.2.

(V_{Pb}^{-2}, V_{Te}^{+2}), and for Te-rich conditions are Pb vacancy and Te anti-site defects (V_{Pb}^{-2}, Te_{Pb}^{+2}). The most dominant defect is determined by the position of the Fermi level, which in turn is calculated as a function of temperature by solving the charge neutrality condition. Under the assumption of dilute limit of defect concentrations, the number of free charge carriers in the compound is controlled by the number of electrons charged defects that can either donate to or accept from the bands. The conservation of charge neutrality condition requires,

$$n - p = \sum_d q_d c_{d,q}, \tag{3.11}$$

where n and p are the free carrier concentrations of electrons and holes given by,

$$\begin{aligned} n &= \int_{E_{CBM}}^{+\infty} n(E) f(E;\mu_e,T) dE \\ p &= \int_{-\infty}^{E_{VBM}} n(E)[1 - f(E;\mu_e,T)] dE, \end{aligned} \tag{3.12}$$

where $n(E)$ is the density of states of the defect-free crystal, and $f(E;\mu_e,T)$ is the Fermi-Dirac distribution. In the non-degenerate limit, when Fermi levels are more than several kT below E_{CBM} and above E_{VBM}, the carrier concentrations simplify to [66],

$$\begin{aligned} n &= N_C \; exp(-\frac{E_{CBM} - \mu_e}{kT}) \\ p &= N_V \; exp(-\frac{\mu_e - E_{VBM}}{kT}), \end{aligned} \tag{3.13}$$

where k is the Boltzmann constant, and N_C and N_V are the effective density of states in the conduction and valence bands, respectively, given by,

$$\begin{aligned} N_C &= 2(\frac{2\pi m_e kT}{h^2})^{3/2} \\ N_V &= 2(\frac{2\pi m_h kT}{h^2})^{3/2}, \end{aligned} \tag{3.14}$$

where h is the Planck's constant, and m_e and m_h are the effective masses for the electrons and holes, and are equal to $0.17m_0$ and $0.20m_0$, respectively, for PbTe [66] where m_0 is the mass of an electron. In Eqn. (3.11) above, q_d is the charge of the defect d with concentration $c_{d,q}$. In the dilute limit of defect concentrations, the concentration $c_{d,q}$ of a particular defect in the structure is given by the Botlzmann distribution,

$$c_{d,q} = c_0 e^{-\Delta H_{d,q}/kT}, \tag{3.15}$$

where c_0 is the concentration of possible defect sites in the supercell.

Band-gap correction scheme: The GGA functional used in this work results in an erroneous band gap of 0.82 eV because of which we need to correct our defect formation energies. Without doing more computationally expensive hybrid functional or SOC calculations, we have employed a simple projection scheme for this. According to this scheme, the electron chemical potential μ_e is mapped between the carrier concentrations (n and p in Eqn. (3.13)) and defect concentrations ($c_{d,q}$ in Eqn. (3.15)) that assume different band gaps. This mapping is accomplished by turning μ_e into a fractional quantity of the band gaps as,

$$x = \frac{\mu_{e,exp}}{E_{g,exp}} = \frac{\mu_{e,theo}}{E_{g,theo}}, \tag{3.16}$$

where $\mu_{e,exp}$ is used in Eqn. (3.13), $E_{g,exp}$ is the temperature dependent experimental band gap

from Ref. [63] used in this equation for the calculation of n and p, and $\mu_{e,theo}$ is used in Eqn. (3.1) and (3.15) for the calculation of defect energies $\Delta H_{d,q}$ and concentrations $c_{d,q}$ that use the theoretical GGA band gap of $E_{g,theo} = 0.82$ eV. The fractional quantity x can be solved for self-consistently from the charge neutrality condition in Eqn. (3.11), which becomes,

$$N_C \; exp(-\frac{E_{CBM} - \mu_{e,exp}}{kT}) \; - \; N_V \; exp(-\frac{\mu_{e,exp} - E_{VBM}}{kT}) \; = \; \sum_d q_d c_0 e^{-\Delta H_{d,q}(\mu_{e,theo})/kT}, \quad (3.17)$$

where $\Delta H_{d,q}$ is a function of $\mu_{e,theo}$ as in Eqn. (3.1). Solving this equation for x gives us $\mu_{e,exp}$ and $\mu_{e,theo}$ from Eqn. (3.16) above. It is $\mu_{e,theo}$ that is used to represent the electron chemical potential or Fermi level μ_e mentioned in the text of this work, and used in the figures.

The position of the Fermi level as a function of temperature is determined by numerically solving the charge neutrality condition in Eqn. (3.11) at a range of temperatures, the results of which are shown in Fig. 3.2 for both Pb-rich and Te-rich growth conditions. This range of Fermi level results in electrons being the dominant carrier for Pb-rich conditions and holes for Te-rich conditions, thus correctly predicting n-type behavior on the Pb-rich side and p-type behavior on the Te-rich side as observed in various experiments [31–37]. The calculated net carrier concentrations are plotted in Fig. 3.3, and also agree well with these experimental data. The position of Fermi levels leads to vacancies being the most dominant defects for both Pb-rich and Te-rich conditions. Donor defects V_{Te}^{+2} for Pb-rich conditions and acceptor defects V_{Pb}^{-2} for Te-rich conditions are the highest concentration defects that lead to the observed n-type and p-type behavior, respectively. Table 3.1 shows the defect formation energies of all defects calculated at the equilibrium value of the Fermi level at 300 K. Experimental evidence of Pb and Te vacancies being the primary point defects in PbTe has been shown through experiments by Brebrick and Grubner [32]. The proposition of Pb interstitials being the dominant defect over Te vacancies for Pb-rich conditions had been suggested earlier by Brebrick and Allgaier [31] due to the instability of Pb-saturated crystals, and Schenk *et al* [67] due to the increase of lattice parameter with carrier concentration. However, Brebrick and Grubner [32] later did not see the crystal instability in Pb-rich samples attributing it to impurities, and based on the increasing order of mobility of Te vacancy, Pb vacancy, and Pb interstitial, they implied that Pb and Te vacancies were indeed the predominant point defects. Thus, as has been

confirmed by the DFT calculations in this work, Pb and Te vacancies are the primary defects in PbTe, and this result along with their formation energies shown in Table 3.1 has been used in the thermodynamic CALPHAD model of the PbTe phase as discussed in the following section.

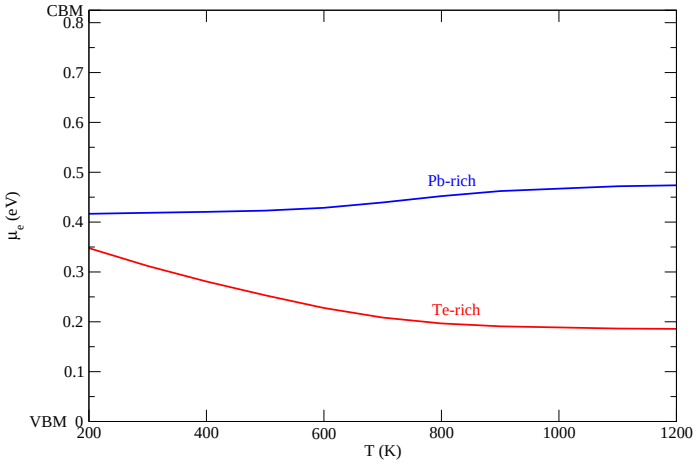

Figure 3.2: (Color online) Equilibrium positions of the Fermi level, μ_e for Pb-rich and Te-rich conditions obtained from solving the charge neutrality equation.

Table 3.1: Defect formation energies $\Delta H_{d,q}$ (eV/defect) calculated for each point defect considered in the PbTe system for chemical potentials corresponding to Pb-rich and Te-rich conditions. Values are determined at $\mu_e = 0.42$ eV for Pb-rich and $\mu_e = 0.31$ eV for Te-rich conditions, which are the equilibrium Fermi levels (relative to the VBM) obtained at T = 300 K by solving the charge neutrality equation, as shown in Fig. 3.2. Only the lowest energy charge state for each defect at this Fermi level, corresponding to Fig. 3.1, is shown.

Pb-rich		**Te-rich**	
Defect	$\Delta H_{d,q}$ (eV/defect)	Defect	$\Delta H_{d,q}$ (eV/defect)
V_{Te}^{+2}	0.72	V_{Pb}^{-2}	0.35
V_{Pb}^{-2}	0.95	Te_{Pb}^{+2}	0.87
Pb_i^{+2}	1.44	V_{Te}^{+2}	1.32
Pb_{Te}^{-2}	1.49	Pb_i^{+2}	2.04
Te_{Pb}^{+2}	2.71	Te_i^{+2}	2.78
Te_i^{+2}	3.73	Pb_{Te}^{-1}	3.29

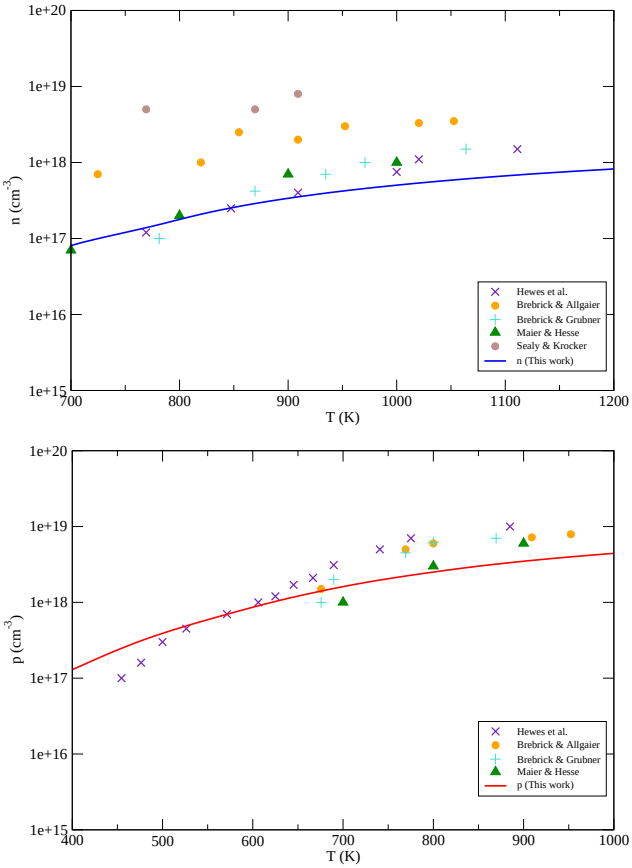

Figure 3.3: (Color online) Calculated concentrations of electrons and holes for Pb-rich and Te-rich growth conditions, respectively, compared with experimental data from Refs. [31–35].

3.3.2 Modification and assessment of the CALPHAD model

The thermodynamic model of the binary Pb-Te system was last calculated and developed by Gierlotka *et al* [41] in which the small non-stoichiometry of the PbTe phase was modeled using the Wagner-Schottky defect model [42] for anti-site defects, i.e., $(Pb, Te)_1$:$(Te, Pb)_1$. In a later publication [55], the PbTe phase was assumed to be an ideal defect-free compound. From our DFT calculations in this work, we found that the Fermi level is positioned where vacancy defects have the lowest formation energy, and are thus more stable than the anti-site defects on both the Pb and Te sublattices, i.e., in Pb-rich and Te-rich crystal growth conditions, respectively. Thus, in this work, we have changed the PbTe phase model to instead consist of vacancies - $(Pb, Va)_1$:(Te,

$Va)_1$, used the defect formation energies calculated from DFT in its Gibbs energy description, and reassessed the entire Pb-Te thermodynamic model.

The evaluation and optimization of the thermodynamic model was performed using the PARROT module of Thermo-Calc [29] package for the calculation of phase diagrams. The Gibbs free energy G_m^{ϕ} of each phase expected to participate in the equilibrium phase diagram of the system was defined using models as described in Section 2. Parameters X_2 and X_3 in the Gibbs free energy expansion of the PbTe phase shown in Eqn. (3.10) are fixed to the DFT defect formation energies of V_{Te}^{+2} and V_{Pb}^{-2} defects, respectively, shown in Table 3.1 and as explained earlier in Section 2.3.2. Thus, $X_2 = 0.72$ eV/defect = 69,469 J/mol, and $X_3 = 0.35$ eV/defect = 33770 J/mol, as listed in Table 3.2. The rest of the parameters entering these models were fitted to available experimental data on the positions of various solubility lines in the phase diagram. The liquidus line was fitted to data determined by DTA and thermal analysis in Refs. [68–72]. The position of the equilibrium lines of the PbTe phase determined through carrier concentration measurements in Refs. [31–34, 36, 37] were used to fit the rest of the user-defined parameters shown in Eqn. (3.10). Experimental measurements of thermodynamic data on this system are also used to optimize parameters of this system. This additional set of experimental data helps impose restrictions to the optimization process by reducing the degrees of freedom, and thus results in a thermodynamically consistent model [73]. The first set of thermodynamic data used is the enthalpy of mixing of the liquid phase that has been measured using the calorimetric method in Refs. [69, 74–76]. The second set of thermodynamic data used is the chemical potential of Te in the liquid phase that was determined using partial pressure measurements made in Refs. [77, 78] assuming the gaseous phase only contains Te_2.

The set of optimized thermodynamic parameters of the model that form part of the Gibbs free energy functions are listed in Table 3.2 along with the phase models used. The resulting phase diagram is shown in Fig. 3.4. The solubility lines of the PbTe phase are shown in Fig. 3.5 along with solubility lines obtained using defect concentrations calculated using DFT in this work. Both sets of data agree reasonably well with experimental data, and that the solubility on the Pb-rich side is lower than that on the Te-rich side of the stoichiometric line at $x = 0.50$. As is the case with the experimental and CALPHAD-calculated solubility lines, the DFT solubility lines do not meet at the invariant melting point of the phase mainly because the DFT phase boundaries are calculated

Table 3.2: Model description and parameters for phases in the Pb-Te system. The functions GHSERPB, GHSERTE, GLIQPB, and GLIQTE are obtained from the SGTE database [26]. Parameters X_2 and X_3 in the Gibbs free energy expansion of the PbTe phase shown in Eqn. (3.10) are fixed to the DFT defect formation energies of V_{Te}^{+2} and V_{Pb}^{-2} defects, respectively, shown in Table 3.1 and as explained in Section 3.3.2. Thus, $X_2 = 0.72$ eV/defect = 69,469 J/mol, and $X_3 = 0.35$ eV/defect = 33770 J/mol, as listed below.

Phase	**Model**	**Model parameters (J/mol)**
Fcc_A1	Sublattice model $(Pb, Va)_1$	$G_{Pb:Va}^{fcc} = {}^{o}G_{Pb}^{fcc}$ = GHSERPB
Hexagonal_A8	Random solution $(Te)_1$	$G_{Te}^{hex} = {}^{o}G_{Te}^{hex}$ = GHSERTE
Liquid	Associate model $(Pb, Te, PbTe)_1$	G_{Pb}^{Liq} = GLIQPB
		G_{Te}^{Liq} = GLIQTE
		G_{PbTe}^{Liq} = GLIQPB + GLIQTE - 60870.3 + 18.1×T
		${}^{0}L_{Pb,PbTe}^{Liq}$ = 20634.8 - 9.7×T
		${}^{1}L_{Pb,PbTe}^{Liq}$ = 7.9
		${}^{0}L_{Te,PbTe}^{Liq}$ = -4167.5 - 2.7×T
		${}^{1}L_{Te,PbTe}^{Liq}$ = 3500.9
PbTe	Sublattice model $(Pb, Va)_1$:$(Te, Va)_1$	$G_{Pb:Te}^{PbTe}$ = GHSERPB + GHSERTE - 128362.3 + 432.9*T - 52.9×T×LN(T)
		$G_{Pb:Va}^{PbTe}$ = GHSERPB + 69469 + 18×T
		$G_{Va:Te}^{PbTe}$ = GHSERTE + 33770 + 25×T
		$G_{Va:Va}^{PbTe}$ = 0
		${}^{0}L_{Pb,Va:Te}^{PbTe}$ = 20621.9 - 35.7×T

without considering the liquid phase. If considered, the free energy of the liquid phase will most likely fall below that of the PbTe phase above its melting point, thus closing the phase boundaries of the PbTe phase at high enough temperatures by making it more stable. But below the melting points, the agreement is fairly good. Figs. 3.6 and 3.7 show the resulting thermodynamic data from the CALPHAD model on the enthalpy of mixing of the liquid phase and chemical potential of Te in the liquid phase at 1200 K, respectively, which agree well with experimental literature.

3.4 Conclusions and outlook

In this work, first principles calculations of defect energetics are used to understand the thermodynamic stability of different types of point defects in PbTe. For Pb-rich chemical potentials and crystal growth conditions, we find that the most stable defects with the lowest formation energy are Te vacancies V_{Te}^{+2} and Pb vacancies V_{Pb}^{-2}, whereas those for Te-rich growth conditions are Te

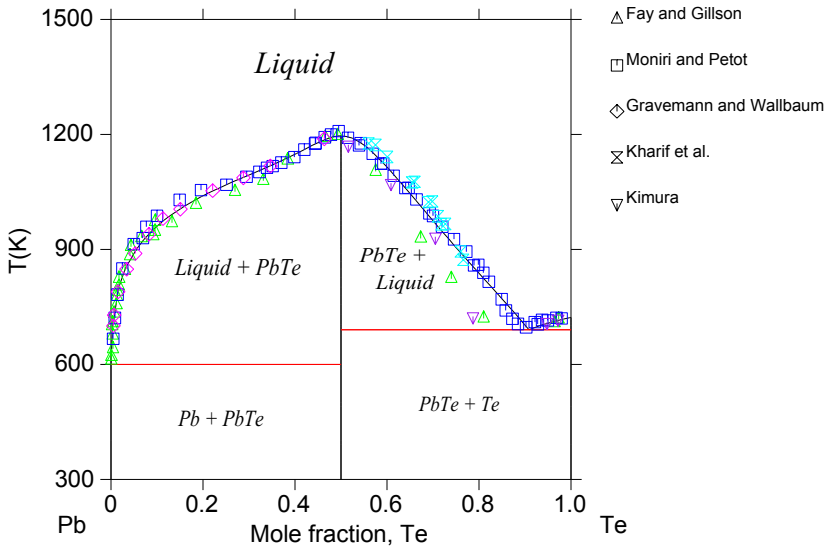

Figure 3.4: (Color online) Pb-Te phase diagram calculated with the CALPHAD method and compared with experimental data.

anti-sites Te_{Pb}^{+2} and Pb vacancies V_{Pb}^{-2}. The Fermi level is determined at various temperatures by numerically solving the charge neutrality equation, which tells us the equilibrium defect and carrier concentrations for various defects in each charged state for both growth conditions. It is found that the electron donating Te vacancies V_{Te}^{+2} are the highest concentration defects for Pb-rich conditions, which are the cause of its n-type conductivity, whereas it is the electron accepting Pb vacancies V_{Pb}^{-2} that are the cause of p-type conductivity in PbTe for Te-rich growth conditions. This result, along with calculated electron and hole concentrations, agrees well with data from previous experimental works.

This information is then used to modify and re-develop the thermodynamic model of the Pb-Te system using the CALPHAD method. A previous thermodynamic model of this system assumed an anti-site defect model for the PbTe phase, i.e., (Pb, Te)$_1$:(Te, Pb)$_1$. However, from our calculations we found that it is actually the vacancy defects that predominate in this phase over anti-site or interstitial defects. Accordingly, the defect model for this phase was changed to (Pb, Va)$_1$:(Te, Va)$_1$. In addition to this, the defect formation energies calculated from DFT were used in the parameters of the Gibbs free energy expression of this phase and the resulting non-stoichiometric

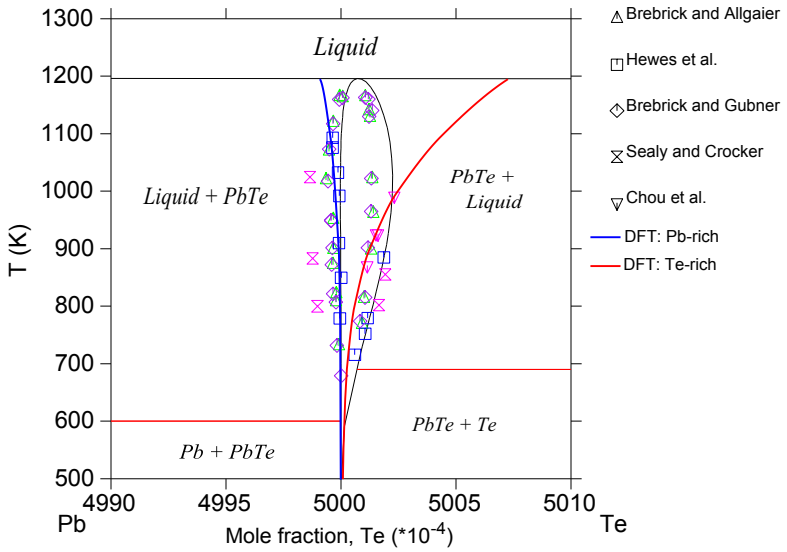

Figure 3.5: (Color online) Solidus lines of the PbTe phase calculated with the CALPHAD method compared with solubility lines calculated from DFT, and with experimental data.

range was in very good agreement with experimental data. The entire system was then re-assessed based on experimental information on the phase diagram and thermodynamic data on the mixing enthalpy of the liquid phase and chemical potential of Te in the liquid phase. Thus, in this work, we have demonstrated the use of DFT in conjunction with the CALPHAD method by calculating defect formation energies of various intrinsic point defects in PbTe using DFT, and then using those numbers as input to the thermodynamic model of the technologically important PbTe phase, which resulted in solubilities in excellent agreement with experiments. Such a methodology is important for the computation of solubility/stability ranges of dopants in TE materials in different regions of the phase diagrams, which is critical to the fine tuning of TE properties.

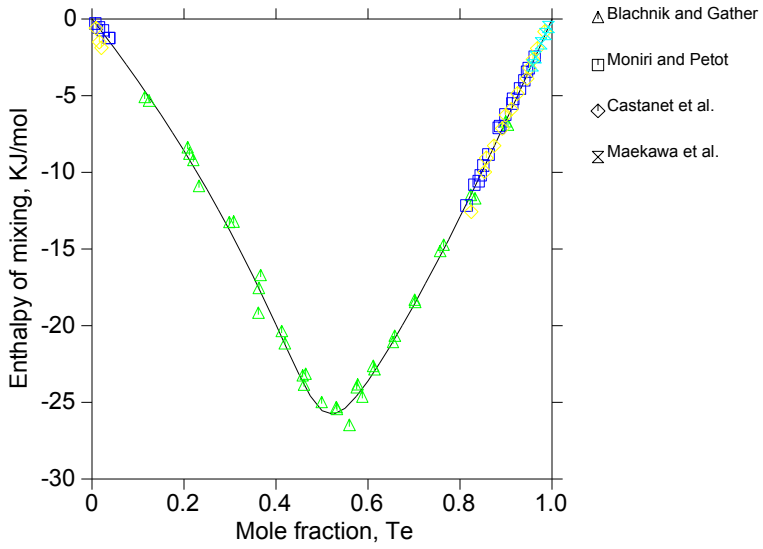

Figure 3.6: (Color online) Enthalpy of mixing of the liquid phase calculated at T = 1200 K with reference to the liquid phase states of Pb and Te, and compared with experimental data.

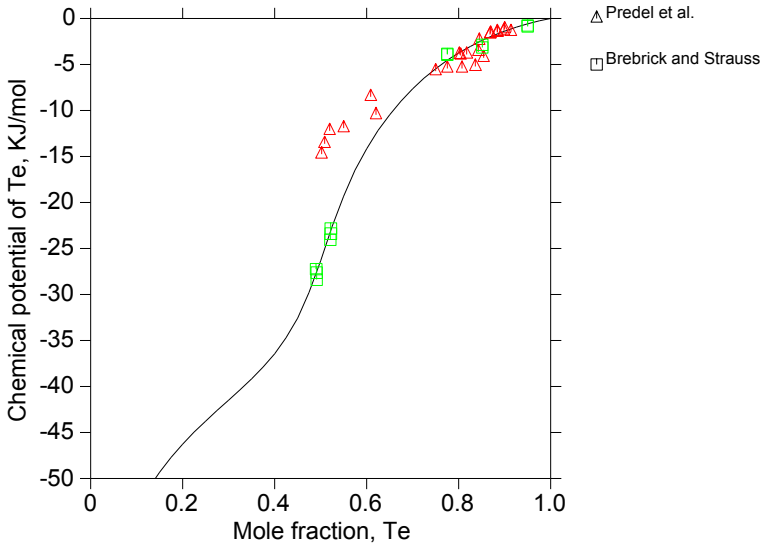

Figure 3.7: (Color online) Chemical potential of Te in the liquid phase calculated at T = 1200 K with reference to the fcc phase of Pb and hexagonal phase of Te, and compared with experimental data.

Chapter 4

Calculation of dopant solubilities and phase diagrams of X-Pb-Se (X = Br, Na) limited to defects with localized charge

4.1 Introduction

Impurity dopants are key to unlocking the potential of semiconductors for a variety of applications. Impurities act as extrinsic dopants that allow for precise control over charge carrier sign and densities. In a semiconductor with an ideal dopant, the excess charge supplied is directly related to the dopant concentration. In PbSe, for example, the substitution of a Br atom for a Se atom should make an ideal n-type dopant because each Br brings one extra electron even though the electronic states of Br are essentially the same as those of Se. Similarly the substitution of Na for Pb should be ideal for p-type PbSe. In many applications, the performance of a semiconductor is limited by the dopant solubility, which is the amount of dopant that can be incorporated [79] before a dopant-rich secondary phase precipitates from the semiconductor (known as dopant precipitation). Such formation and evolution of unwanted secondary phases often harms lifetime performance, or even the stability and integrity of the material. A phase diagram provides essential information for material design to address these challenges. However, experimental phase diagrams are not always available, or available without enough detail in the region of interest. In such cases, calculated phase diagrams could provide alternative guidelines and help in the development new materials.

Density functional theory (DFT) [14, 15] based defect energy calculations provide powerful insights for understanding properties of lightly doped semiconductors used as photovoltaics or optoelectronics (see, for example Ref. [80]) that have band gaps of nearly 1 eV or greater. Such studies have been particularly helpful in identifying charge state transitions of deep defects, states that form well inside the forbidden energy gap.

In this study, we use DFT methods to investigate the defect thermodynamics of ideal dopants in the narrow band gap ($\approx$ 0.3 eV) semiconductor PbSe. Experiments performed for this work show that Br is indeed an ideal donor dopant and Na is an ideal acceptor dopant with essentially 100% doping effectiveness, indicating that one charge carrier is measured for each impurity atom. Doping effectiveness is defined as the ratio of carrier concentration of the sample to the amount of dopant added to it and is given by,

$$\eta \;=\; \frac{n-p}{\sum\limits_{d,q}^{'} c_{d,q}^{'}} \quad or \quad \frac{p-n}{\sum\limits_{d,q}^{'} c_{d,q}^{'}}, \tag{4.1}$$

where the numerator is electron concentration $(n-p)$ in the case of Br-Pb-Se and $(p-n)$ in the case of Na-Pb-Se, and $\sum\limits_{d,q}^{'} c_{d,q}^{'}$ is the total atom concentration of the dopant in the PbSe phase found by summing over all the dopant containing defects. PbSe is chosen because the lead chalcogenides (PbQ, Q = Te, Se, S) with the rock-salt structure are excellent thermoelectric materials [13, 81–88] for applications between 600 K and 900 K [89], where its zT exceeds 1 [88] for both p-type [82] and n-type [84] materials. Br is chosen due to its comparable size and electronic structure to Se, and reported $zT \;=\; 1.1 \pm 0.1$ at 850 K [84]. Similarly, Na provides fine control over hole carrier concentration [81, 90] that leads to zT close to 1 at 850 K in PbSe [82, 91].

Despite the frequent use of these impurity dopants, no experimental literature is available (to the authors′ knowledge) on the phase diagrams of Br-Pb-Se or Na-Pb-Se, which is unsurprising due to the complexity of the experiments required to determine a ternary phase diagram. Accurate calculations of dopant solubilities could supplant tiresome experiments in the search for new semiconductors.

4.2 Methodology

The solubility limits of dopants in the PbSe phase in the ternary phase spaces of the Br-Pb-Se and Na-Pb-Se systems are determined by first using DFT to calculate the defect formation energies of intrinsic and extrinsic defects consisting of vacancies (V_{Pb}, V_{Se}), substitutions (Pb_{Se}, Se_{Pb}), interstitials (Pb_i, Se_i), and dopant-containing defects consisting of Br and Na substitutions on Pb or Se (Br_{Pb}, Br_{Se}, Na_{Pb}, Na_{Se}), as well as interstitial Br and Na (Br_i, Na_i), all in neutral and charged states ranging from -2 to +2. The defect formation energy of a defect d of charge q is given by [43],

$$\Delta E_{d,q} = [E_{d,q} - E_H] + \sum_{\alpha} n_{\alpha}^{d}(\mu_{\alpha}^{0} + \Delta\mu_{\alpha}) + q(E_{VBM} + \Delta V_{PA} + \mu_e) + \Delta E_{IC}, \quad (4.2)$$

where $E_{d,q}$ and E_H are the DFT total energies of the defect containing PbSe supercell and the pure PbSe supercell, respectively, n_{α}^{d} is the number of atoms added (n_{α}^{d} = -1) or removed (n_{α}^{d} = +1) from the pure supercell to form the defect, μ_{α}^{0} is the chemical potential of element α in its ground state or standard metallic state, and $\Delta\mu_{\alpha}$ is the change in the chemical potential of α corresponding to a particular phase equilibrium between PbSe and other compounds in the X-Pb-Se systems. μ_{α}^{0} and $\Delta\mu_{\alpha}$ are calculated using elemental ground state energies and compound formation energies taken from the Materials Project [92–94] (the calculation settings used by the Materials Project are verified to be the same as those used in the calculation of defect energies in this work so as to avoid any errors in the formation energies). E_{VBM} is the energy of the valence band maximum (VBM) and corresponds to the energy of the highest occupied level. ΔV_{PA} is the potential alignment (PA) correction term used to re-align defect energy levels with energy levels of the host supercell, and is calculated using $\Delta V_{PA} = \overline{(V_{d,q}^{r} - V_{H}^{r})}$ [44], where $V_{d,q}^{r}$ and V_{H}^{r} are the spherically-averaged electrostatic potentials of the defect and host supercells, respectively, far from the defect site so as to avoid including any spurious chemical interactions with it. The potential alignment correction term ranges from +0.08 eV to -0.13 eV for various charged defects. ΔE_{IC} is the image charge correction energy term that is added to the defect formation energy in order to model a true isolated charge defect in a size-limited supercell in non-degenerate conditions, and is calculated using the Makov-Payne expansion [45]. The dielectric constant ϵ used in this expansion is calculated to be equal to 594 (including both ion-clamped and ionic contributions) for PbSe using density functional

perturbation theory as implemented in the Vienna Ab-initio Simulation Package (VASP) [46–48]. Due to the high dielectric constant of PbSe, ΔE_{IC} has a maximum value of ≈ 7 meV in this work for q $\pm$ 2 charges, and thus has a minimal effect on defect formation energies. Finally, μ_e in Eqn. (4.2) is the electron chemical potential that is the additional energy of electrons in our system, and is set to range in values around the energies of the VBM and CBM (conduction band minimum) for plots showing the variation of defect formation energies as functions of electron chemical potential. μ_e is calculated as a function of temperature T and sets of chemical potentials μ_α by solving the charge-neutrality condition,

$$n \ - \ p \ = \ \sum_d q_d c_{d,q}, \tag{4.3}$$

where n and p are the free carrier concentrations of electrons and holes given by [95],

$$\begin{aligned} n \ &= \ \int_{E_{CBM}}^{+\infty} n(E) f(E;\mu_e,T) dE, \\ p \ &= \ \int_{-\infty}^{E_{VBM}} n(E)[1 \ - \ f(E;\mu_e,T)] dE, \end{aligned} \tag{4.4}$$

where $n(E)$ is the density of states of the defect-free crystal, and $f(E;\mu_e,T)$ is the Fermi-Dirac distribution. $c_{d,q}$ is the defect concentration, and in the dilute limit is given by [95],

$$c_{d,q} \ = \ N_{site}^{d,q} N_{sym}^{d,q} e^{-\Delta E_{d,q}/kT}, \tag{4.5}$$

where $N_{site}^{d,q}$ is the number of defect sites per formula unit of PbSe and $N_{sym}^{d,q}$ is the number of geometrically distinct but symmetrically equivalent ways of adding defect d with charge state q to a site.

The solvus boundaries of PbSe in the X-Pb-Se systems are calculated by summing over concentrations of each defect d, weighted by $-n_\alpha^d$, which is the change in composition of the XPbSe phase due to that defect, and is given by [96],

$$n_\alpha \ = \ \sum_d -n_\alpha^d c_{d,q}. \tag{4.6}$$

When calculated under different sets of chemical potentials μ_α, which represent different phase

equilibrium regions between PbSe and other compounds in the phase diagram, and at a particular temperature T, we obtain an isothermal section of the phase boundaries of PbSe in the system X-Pb-Se. Further details of this methodology can be found in the next chapter.

4.2.1 Computational details

DFT calculations in this work for the calculation of energies of the defect and host supercells are performed using VASP [50–53]. Ion-electron interactions were described using the Projector Augmented Wave (PAW) potentials [22–24] utilizing the generalized gradient approximation (GGA) with the exchange-correlation functional of Perdew, Burke, and Ernzerhof (PBE) [18]. The $5d^{10}6s^26p^2$ electrons of Pb, $4s^24p^4$ electrons of Se, $4s^24p^5$ electrons of Br, and $2p^63s^1$ electrons of Na are treated as valence states in the PAW potentials. All supercell calculations are performed on a 5 x 5 x 5 supercell of the primitive cell and contain 250 atoms. The cutoff energy of plane wave basis was set to 400 eV, a Gaussian smearing width of 0.1 eV is used to smear electron occupations, and integrations over the first Brillouin zone are made using a 2 x 2 x 2 Monkhorst-Pack k-point grid [54]. Unit cell parameters and atomic positions are relaxed based on an energy convergence criteria of 10^{-4} eV, and a final static calculation is performed for each defect to obtain accurate total energies.

4.3 Results and Discussion

Figs. 4.1 and 4.2 show the defect formation energies of the lowest energy defects in the Br-Pb-Se and Na-Pb-Se systems, respectively, plotted as a function of electron chemical potential or Fermi level μ_e for different regions of three-phase equilibrium that contain the PbSe phase. The dominant defects (defects with highest concentrations) of a system are determined by the equilibrium μ_e calculated as a function of temperature and atomic chemical potentials by numerically solving the charge neutrality condition in Eqn. 4.3. In the case of Br-Pb-Se, the equilibrium μ_e is positioned where, from Fig. 4.1, the lowest energy defects are Br_{Se}^{+1} and V_{Pb}^{-2} in the Se-rich PbSe-Se-$PbBr_2$ region and Br_{Se}^{+1} and Br_{Se}^{0} in the Pb-rich Pb-PbSe-$PbBr_2$ region. In Na-Pb-Se, from Fig. 4.2, the defect energy landscape in three out of the four regions of three-phase equilibria is dominated by the Na_{Pb}^{+2}, Na_{Pb}^{+1}, Na_{Pb}^{0}, and Na_{Pb}^{-1} defects. Whereas Na_{Pb}^{-1} is an acceptor defect that tends to dope PbSe p-type, the Na_{Pb}^{+2} and Na_{Pb}^{+1} defects are donor defects that tend to dope PbSe n-type.

However, it is well-known that Na is a p-type dopant in PbQ systems [13, 81, 82, 84, 89] with Na substitution on the Pb^{+2} sublattice producing one conducting hole for each substitution. Thus, the Na_{Pb}^{+2} and Na_{Pb}^{+1} defects would not be expected to be present in notable concentrations, and this discrepancy will be addressed below. The unexpected acceptor defects Br_{Se}^{-1} and Br_{Se}^{-2} do not pose an immediate problem as they are higher in energy than the defects shown in Fig. 4.1.

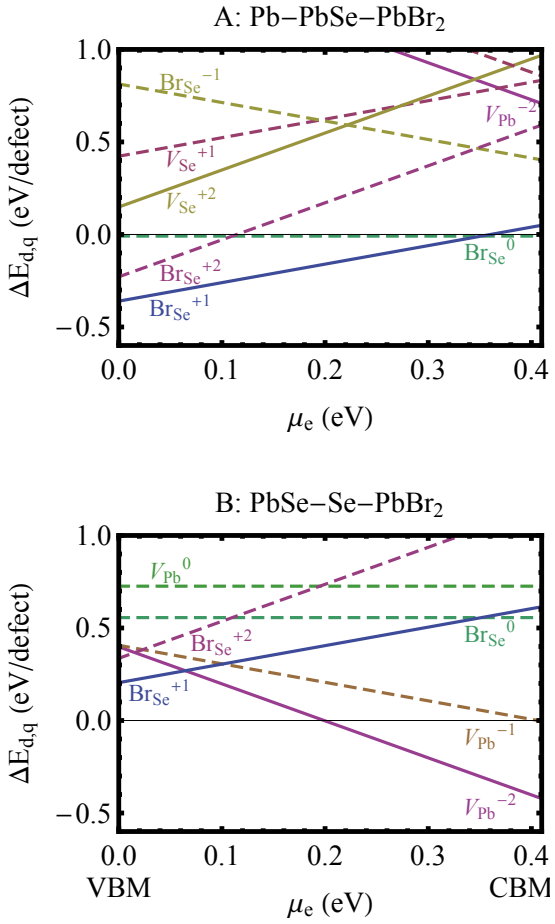

Figure 4.1: (Color online) Defect formation energies, $\Delta E_{d,q}$ of the lowest energy intrinsic and Br-containing defects in PbSe as a function of Fermi level, μ_e (relative to VBM) in different three phase equilibrium regions of PbSe in the Br-Pb-Se phase diagram. Solid lines indicate defects included in the calculation of the Br-Pb-Se phase diagram, whereas dashed lines indicate excluded defects.

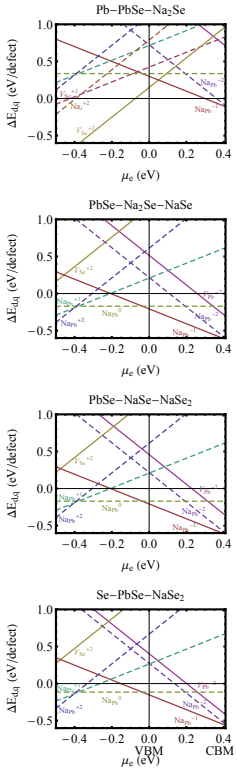

Figure 4.2: (Color online) Defect formation energies, $\Delta E_{d,q}$ of the lowest energy intrinsic and Na-containing defects in PbSe as a function of Fermi level, μ_e (relative to VBM) in different three phase equilibrium regions of PbSe in the Na-Pb-Se phase diagram. Solid lines indicate defects included in the calculation of the Na-Pb-Se phase diagram, whereas dashed lines indicate excluded defects.

The remaining neutral defects, Br^0_{Se} in Br-Pb-Se and Na^0_{Pb} in Na-Pb-Se, would, according to the low energies calculated, appear to play a dominant role in determining the dopant concentrations and effectiveness. The formation energy of the Br^0_{Se} defect in the Pb-rich Pb-PbSe-$PbBr_2$ region is slightly negative at about -8.8 meV (independent of Fermi level), and the equilibrium Fermi level in these conditions is positioned where the formation energies of these defects are negative. A similar issue is seen in Na-Pb-Se (Fig. 4.2): the defect formation energy of Na^0_{Pb} is negative, with a minimum of -0.171 eV, in three out of four regions of three-phase equilibria: PbSe-Na_2Se-NaSe, PbSe-NaSe-$NaSe_2$, and Se-PbSe-$NaSe_2$. This issue is however not seen in the Na-Pb-Te system in which, from Ref. [96], the Na^0_{Pb} defect is higher in energy and lower in concentration than the Na^{-1}_{Pb} defect at equilibrium Fermi levels in all regions of the phase diagram.

Negative defect formation energies (of neutral defects, which do not depend on μ_e) lead to unrealistic values for defect concentrations (> 100 %) under the dilute limit approximation, and thus low (essentially zero) dopant effectivity. If true, such defect formation energies would indicate non-equilibrium conditions or disorder at 0 K, in violation of the third law of thermodynamics, and so we must conclude that these calculations are either inaccurate or do not represent the intended defect.

There are several frequently suspected causes for inaccurate defect formation energies, which are listed below. For each of them we provide a rational argument for its insufficient impact on the results,

- First, unknown ternary compounds in the Br-Pb-Se and Na-Pb-Se systems could change the chemical potential map and hence the defect energies:

The relative energy difference between defects of the same element type but different charge state (e.g., Br_{Se}^{+1} vs Br_{Se}^{0}) does not depend on the chemical potential. Thus the low doping effectiveness calculated due to neutral defects will not be affected by the presence of unknown ternary phases.

- Second, inaccuracy of correction methods, such as image charge, potential alignment, band-filling corrections (not incl here):

Because the image charge and potential alignment corrections terms only affect charged defects, they cannot influence the neutral Br_{Se}^{0} and Na_{Pb}^{0} defects ($q = 0$ in Eqn. 4.2). Additionally, the magnitude of band-filling corrections [65] are not expected to be significant enough to resolve the issues discussed here.

- Third, non-convergence of formation energies at employed supercell size:

The formation energies of the defects in question appear to be converged within 0.1 eV, while, as we shall see below, the defect energies are at least 0.5 eV too low. Furthermore, in this work, these energies are found to decrease with an increasing supercell size, which follows a trend opposite to what may resolve the issue of unexpectedly low formation energies.

- Fourth, an incorrect determination of defect energies due to the DFT method employed as evidenced by an incorrect band gap that does not include spin-orbit coupling (SOC) effects, the use of hybrid functionals, or employment of the GW approach, etc.:

The calculated direct band gap of 0.41 eV at the L point using GGA over-estimates but is in fairly good agreement with the experimentally obtained value of 0.28 eV at room temperature

[63, 97, 98]. Previous calculations in Refs. [99–101] show that including SOC effects reduces the gap to near zero or negative values, representative of a metal, whereas the GW method or the use of hybrid HSE03 functionals, with and without SOC, leads to band gaps of $\approx$ 0.13 eV and 0.58 eV, respectively, which are both less accurate than just PBE-GGA. Also note that even in cases of materials with better agreement, the employment of these methods to defect supercells of size in the order used in this work (250 atoms) is computationally impractical. Although such calculations are plausible on smaller supercells, the image charge and potential alignment correction terms become very large, making any errors in these terms more pronounced, potentially negating the beneficial effect of using an accurate band gap.

In order to quantify the magnitude that the calculated Br^0_{Se} defect formation energy must be underestimated we calculate the doping effectiveness using Eqn. 4.1 at 973 K in the Pb-PbSe-$PbBr_2$ region of Br-Pb-Se and PbSe-Na_2Se-NaSe region of Na-Pb-Se as shown in Fig. 4.3. While Br^{+1}_{Se} produces one electron in the conduction band per Br atom, the extra electron in Br^0_{Se} is delocalized around the Br defect without adding electrons to the conduction band. Thus, Br^0_{Se} serves only to reduce the doping effectiveness. We know from extensive studies on polycrystalline PbSe doped with Br or Na that $Pb_{1.002}Se_{0.992}Br_{0.002}$ has nearly 100% doping effectiveness and $Pb_{0.9875}Na_{0.0125}Se$ has 90% [82, 84, 89] indicating that the formation energy of Br^0_{Se} and Na^0_{Pb} must be underestimated by at least 0.5 eV. These results are from samples made by first melting nominal compositions of $Pb_{1.002}Se_{1-x}Br_x$, or $Pb_{1-y}Na_ySe$. The ingots were annealed at 973 K for 72 hours, followed by consolidation of crushed powder by hot pressing, after which their Hall effect carrier densities were measured.

The severe underestimation of the Br^0_{Se} formation energy using DFT can be traced to delocalization of the extra Br electron in the DFT calculation, which leads us to conclude these do not represent the intended defects. Thus, in essence, this energy does not reflect the energy of the neutral defect with a localized charge, but instead the energy of a donor defect where the electron has formed a large polaronic state at the bottom of the conduction band. Such large polarons, which are essentially electrons in hydrogen atom like states around a central, charged (but screened) defect are expected from shallow defects [64]. In Fig. 4.4 we plot the partial charge density of the highest occupied state calculated for PbSe with the neutral Br^0_{Se} defect. These electrons are clearly not

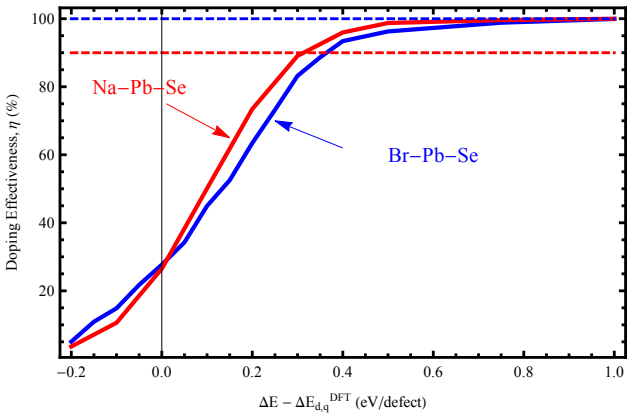

Figure 4.3: (Color online) Doping effectiveness of the shown defects at 973 K in the Pb-PbSe-$PbBr_2$ region of Br-Pb-Se and PbSe-Na_2Se-NaSe region of Na-Pb-Se calculated by varying the formation energies of the neutral Br^0_{Se} and Na^0_{Pb} defects (x-axis), respectively. ΔE - $\Delta E^{DFT}_{d,q}$ indicates the change from the true DFT calculated formation energy. Dashed lines mark the experimentally measured values of doping effectiveness for each system.

localized around the Br defect but delocalized as part of the conduction band.

We also notice that the +/0 donor transition level for the Br_{Se} defect (0/- acceptor transition level in case of Na_{Pb}) is close to the CBM (VBM for Na_{Pb}), as seen in Fig. 4.1, consistent with these neutral defects being shallow defects. The transitions are close to the band edge because the doped electron from the Br^{+1}_{Se} defect is located in a state that looks similar to and is close in energy to the CB, as evident from Fig. 4.4. The calculated neutral defect Br^0_{Se} is thus effectively the same as the charged defect Br^{+1}_{Se} with the Fermi level located near the CBM. The defect formation energy calculated for the neutral case instead becomes correlated with the formation energy of the charged defect at the band edges. Thus, the defect energy for Br^0_{Se} calculated by DFT (and most likely other defects with unexpected charge states as well) does not, in fact, have the charge state intended. Instead the charge has been delocalized, altering the charge state of the defect.

Excluding the defects Br^0_{Se}, Na^0_{Pb}, and others marked with dashed lines in Figs. 4.1 and 4.2, for phase diagram calculations, we can calculate realistic isothermal sections of solvus boundaries of the PbSe phase at 973 K in the Br-Pb-Se and Na-Pb-Se ternary phase diagrams, as shown in Figs. 4.5 and 4.6, respectively. From Fig. 4.5 it is evident that peak Br solubility in PbSe occurs

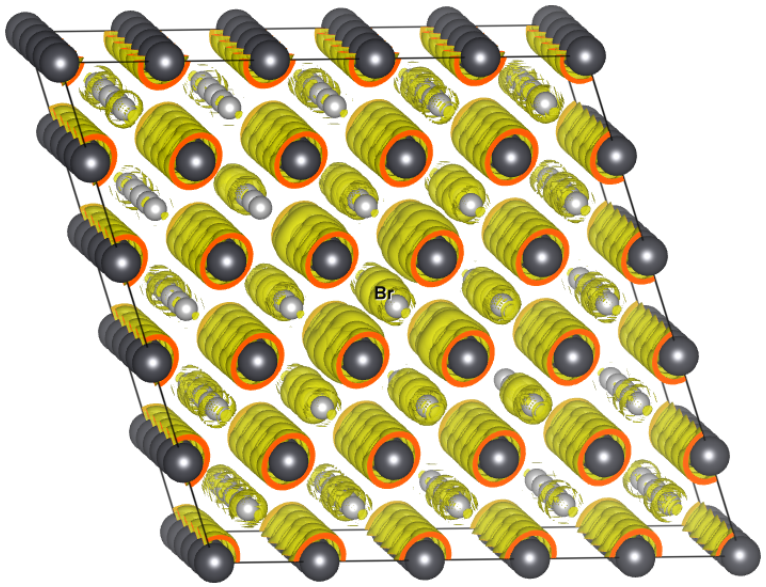

Figure 4.4: (Color online) Partial charge density plot of the highest energy electrons in the supercell (of the PbSe primitive cell) containing the Br^{0}_{Se} defect (at the center of the supercell) showing charge delocalization that makes this defect equivalent to the case of the charged defect Br^{+1}_{Se} with the Fermi level located at or near the CBM. Pb atoms are shown in dark grey, Se atoms in light grey, and Br atom in green.

in a direction slightly Br-rich and Pb-deficient of the PbSe-PbBr line - the line for 1:1 substitution of Se with Br. Fig. 4.6 shows that the PbSe single-phase region is very narraow and has maximum Na solubility along the PbSe-NaSe line, similar to the solubility of Na predicted in PbTe in Ref. [96].

For accurate phase diagrams and dopant effectiveness that matches experiment, we suggest using only the expected charge states for each defect (here: Br^{+1}_{Se}, Na^{-1}_{Pb}, V^{-2}_{Pb}, V^{+2}_{Se}, as marked with solid lines in Figs. 4.1 and 4.2) in calculations of phase diagrams and doping effectiveness. We suspect this is widespread in calculations on easily doped, low band-gap semiconductors with high dielectric constants. Although this problem is understood by the defect calculation community [64], it is not frequently described as the method that was primarily developed to understand deep defects in large band-gap semiconductors or insulators.

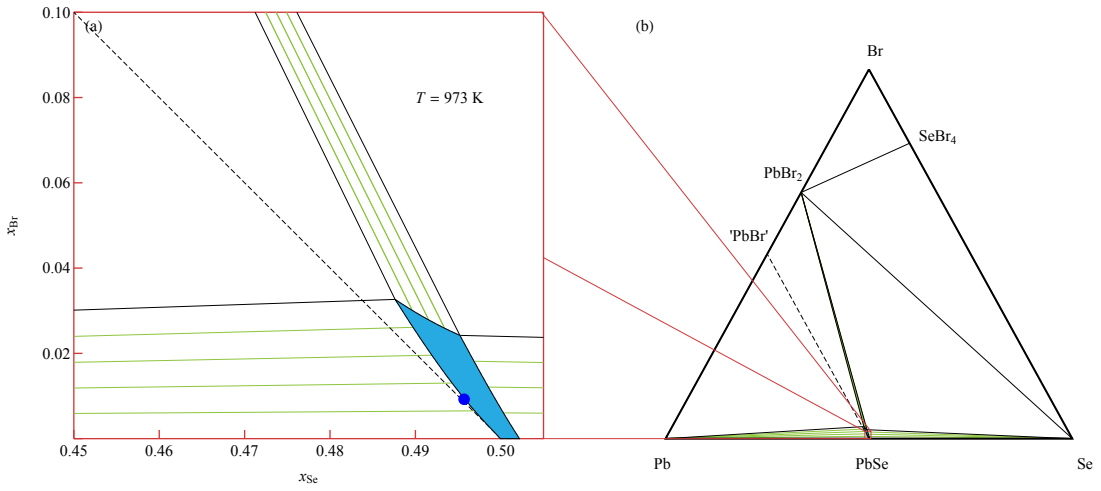

Figure 4.5: (Color online) (a) Isothermal section of the Br-Pb-Se phase diagram calculated at T = 973 K showing the single-phase region of PbSe in blue, and green tie-lines representing two-phase regions between it and other compounds that are shown in the full isothermal section plot in (b). Sample composition at which doping effectiveness measurements were made is shown as a closed blue circle in (a). Dashed line represents a path between PbSe and a hypothetical PbBr compound for one-to-one replacement of Se with Br, i.e., as $PbBr_xSe_{1-x}$.

4.4 Conclusions

In summary, we performed standard defect energy calculations on PbSe with a n-type dopant Br and a p-type dopant Na, and found that defects with unexpected charge states result in unexpectedly low formation energies that would not agree with experimentally observed phase diagrams or dopant efficiencies. This has been traced to the delocalization of charge, which alters the charge state of the calculated defect. Thus, these defects were excluded from calculations of the phase diagrams giving results that appear accurate. Similar consideration is surely relevant to many defect calculations, particularly in narrow band gap semiconductors. Refining a procedure to identify delocalized charge and eliminating unnecessary calculations will expedite the use of such calculations by experimentalists in understanding phase diagrams and devising effective doping strategies. Figures in this chapter have been created using the LevelScheme scientific figure preparation system [102].

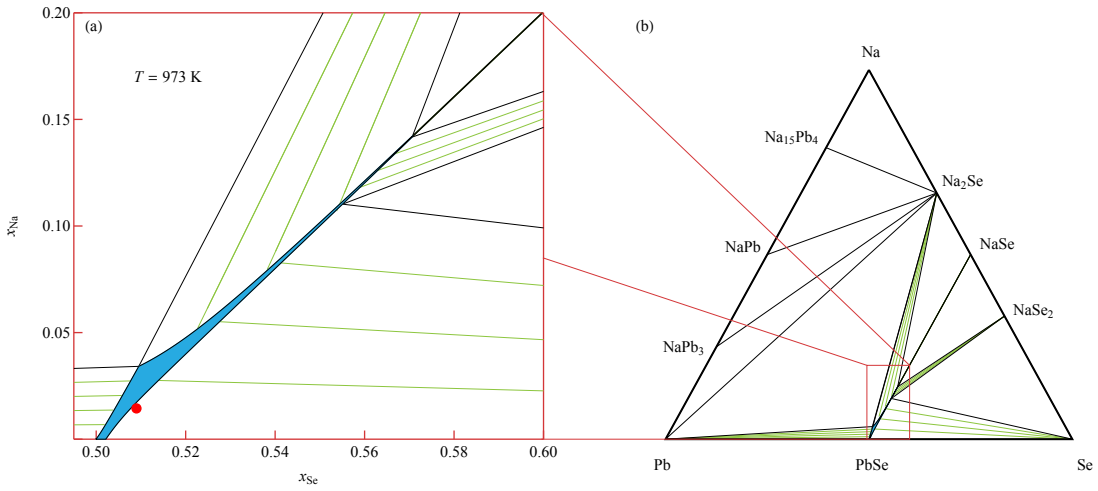

Figure 4.6: (Color online) (a) Isothermal section of the Na-Pb-Se phase diagram calculated at T = 973 K showing the single-phase region of PbSe in blue, and green tie-lines representing two-phase regions between it and other compounds that are shown in the full isothermal section plot in (b). Sample composition at which doping effectiveness measurements were made is shown as a closed red circle in (a).

Chapter 5

Phase diagrams and defect thermodynamics to devise doping strategies in the thermoelectric material PbSe

5.1 Introduction

Thermoelectric generators are devices that are of considerable interest to the automobile, space, and other types of industries [103] as they help recover available energy (or exergy) from waste heat and convert it into electricity. Typical thermoelectric materials that enable the direct conversion between heat and electricity are compound semiconductors. The control of free carrier concentration and improvement of their mobility are at the core of essentially all materials engineering of semiconductors. In order to have desired properties for a specific application, semiconductors need to be doped, which is accomplished by substituting atoms with a different element, i.e., a dopant. Optimal thermoelectric performance requires materials with well-defined electrical and thermal conductivities, thermoelectric power, and high mobility of free charge carriers. These properties are also influenced by the presence of impurities/dopants and their interaction with native point defects, all of which cause deviations from stoichiometry for the semiconductor compound. With renewed interests in developing defect-tolerant electronic materials to meet the current technological, environmental, and energy challenges, the importance of defect studies only increases. Therefore, the investigation of the nature of point defects, both intrinsic and extrinsic, is vital both for an un-

derstanding of the role these defects play in variation of the thermoelectric properties and for their optimal use in practical devices. In particular, the nature of the carrier type is strongly dependent on intrinsic and extrinsic point defects, leading to intensive efforts to understand the role of these defects in variation of the thermoelectric properties.

The range of carrier concentration is usually set by the solubility of a certain dopant, whereas the dominance of an electronically preferred defect leads to either electron or hole conductivity, fine carrier concentration tuning, and high doping efficiency, as well as higher mobilities due to the absence of compensation. On the other hand, for applications under harsh conditions, for example, thermoelectric modules for heat recovery, the formation and evolution of unwanted secondary phases often harms lifetime performance, or even the stability and integrity of devices. Phase diagrams provide useful information in such aspects. However, aside from few extensively studied systems, experimental phase diagrams usually are not available, and even less for ternary systems than binary systems. When available, they lack enough detail in the composition ranges of interest. In such cases, calculated phase diagrams could provide alternative guideline for optimized doping strategies.

The rock-salt lead chalcogenides (PbQ, Q = Te, Se, S) are a popular class of TE materials that, due to their superior properties [13], have been the subject of significant TE materials research [81–84]. The material system we studied is PbSe, which has received great interest as a material for thermoelectric power generation [82, 85–88] at high temperatures (600 - 900K) [89] where its zT exceeds 1 [88] for both p-type [82] and n-type [84] samples. In comparison with PbTe, one of the most widely studied TE materials, PbSe is advantageous, as Se is less expensive and more abundant than Te. The amount of dopant governs the carrier concentration in PbSe, and the maximum concentration of dopant that can be added to it without precipitating secondary phases can be determined by calculating the solvus boundary of the PbSe single phase in the ternary system X-Pb-Se, where X is a dopant. With monovalent atoms substituting on the anion Se^{-2} sublattice, PbSe is doped n-type with one conducting electron produced for each substituted Se atom, whereas substitutions on the Pb^{+2} sublattice dopes PbSe p-type with one conducting hole produced for each substituted Pb atom. In this work, using a large set of defect energies calculated using density functional theory (DFT) [14, 15], and a ternary statistical mechanics model we investigate the influence on the single phase boundary of PbSe in the cases of addition of Cl, I, Sb, Bi, and In.

Through the calculated solvus boundaries, it will become possible to determine dopant solubilities and electrical conductivity properties in different regions of the phase diagram, which will help devise the most effective synthesis routes for adding dopants to PbSe.

5.2 Methodology

5.2.1 Defect thermodynamics

To determine the solvus boundaries of the PbSe phase in the phase spaces of the ternary system X-Pb-Se (the Cl-Pb-Se, I-Pb-Se, Sb-Pb-Se, Bi-Pb-Se and In-Pb-Se systems in this work), first we calculate the defect formation energies of intrinsic defects consisting of vacancies (V_{Pb}, V_{Se}), substitutions (Pb_{Se}, Se_{Pb}), interstitials (Pb_i, Se_i), and extrinsic defects consisting of dopant substitutions on Pb or Se (Cl_{Pb}, Cl_{Se}, I_{Pb}, I_{Se}, Sb_{Pb}, Sb_{Se}, Bi_{Pb}, Bi_{Se}, In_{Pb}, In_{Se}), as well as interstitials (Cl_i, I_i, Sb_i, Bi_i, In_i), all in neutral and charge states ranging from q = -2 to +2. All sites in the PbSe supercell are symmetrically equivalent for the defect to be positioned. The defect formation energy of a defect d of charge q of a solute in the PbSe compound is given according to the Zhang-Northrup supercell formalism [43] by,

$$\Delta E_{d,q} = [E_{d,q} - E_H] + \sum_{\alpha} n_{\alpha}^{d}(\mu_{\alpha}^{0} + \Delta\mu_{\alpha}) + q(E_{VBM} + \Delta V_{PA} + \mu_e) + \Delta E_{IC}, \quad (5.1)$$

where $E_{d,q}$ and E_H are the DFT total energies of the defect containing PbSe supercell and the pure PbSe supercell, respectively, n_{α}^{d} is the number of atoms added (n_α = -1) or removed (n_α = +1) from the pure supercell to form the defect, μ_{α}^{0} is the chemical potential of an element in its ground state or standard metallic state, and $\Delta\mu_\alpha$ is the change in the chemical potential of α with reference to its standard state corresponding to a particular three-phase equilibrium between PbSe and other compounds in the X-Pb-Se systems. μ_{α}^{0} and $\Delta\mu_\alpha$ are calculated using elemental ground state energies and compound formation energies taken from the Materials Project [92–94] (the calculation settings used by the Materials Project are verified to be the same as those used in the calculation of defect energies in this work so as to avoid any errors in the formation energies). For a maximally rich growth environment of an element, $\Delta\mu_\alpha = 0$. In these conditions, the chemical potential of the other elements are reduced to below their standard reference state values, i.e., $\mu_\alpha < \mu_{\alpha}^{0}$ ($\Delta\mu_\alpha < 0$).

Their exact values are calculated using compound formation energies in equilibrium for a particular phase region. For example, the three-phase region Pb-PbSe-$PbCl_2$ of the Cl-Pb-Se ternary phase diagram is represented by,

$$\begin{aligned} \mu_{Pb} &= \mu^0_{Pb}(\Delta\mu_{Pb} = 0) \\ \mu_{Se} &= \mu_{PbSe} - \mu_{Pb} \\ \mu_{Cl} &= \frac{\mu_{PbCl_2} - \mu_{Pb}}{2}, \end{aligned} \tag{5.2}$$

where μ_{PbSe} and μ_{PbCl_2} are the formation energies of the defect-free PbSe and $PbCl_2$ compounds.

The second to last term in Eqn. (5.1), i.e., $q(E_{VBM} + \Delta V_{PA} + \mu_e)$, represents the energy cost of exchanging electrons with the electron reservoir for charged defects ($q \neq 0$). The valence band maximum (VBM) energy, E_{VBM}, corresponds to the energy of the highest occupied level. It represents the cost of removing an electron from the top of the valence band, and in this work is evaluated by calculating the energy difference between a neutral defect-free supercell and the supercell with a hole. The creation of a neutral defect in a supercell causes the band energy levels to shift relative to the levels in the defect-free supercell. Furthermore, in the case of creation of a charged defect, the charge neutrality condition is violated, causing the Coulomb potential to diverge. This is avoided by setting $V_{el}(G = 0) = 0$, which is equivalent to introducing a compensating uniform background charge that only affects the potential and not the charge density in the calculation. Thus, the energy levels of the charged defect cell do not reference to the potential of the host cell, needing a re-alignment of the defect energy levels to the host energy levels. This is achieved using a potential alignment (PA) term ΔV_{PA} that is added to the defect formation energy (in Eqn. (5.1) above) and is calculated as [44],

$$\Delta E_{PA} = q.\Delta V_{PA} = q.\overline{(V^r_{d,q} - V^r_H)}, \tag{5.3}$$

where ΔV_{PA} is the potential alignment between the spherically-averaged electrostatic potentials of the defect ($V^r_{d,q}$) and the host (V^r_H) cells far from the defect site so as to avoid including any spurious chemical interactions with the defect. The potential alignment correction term ranges from +0.08 eV to -0.13 eV for various charged defects. Due to the periodic boundary conditions employed by

DFT, charged defects are periodically and infinitely repeated in neighboring supercells, resulting in defect concentrations in the order of tenths of a percent, which is significantly higher than that found in semiconductors (parts-per-million). These periodic images of defects electrostatically interact with each other. Thus, in order to model a truly isolated charge defect in a size-limited supercell, an image charge correction energy term ΔE_{IC} is added to the defect formation energy in Eqn. (5.1). It is typically written in the form of a multipole expansion given by Makov and Payne [45],

$$\Delta E_{IC} \;=\; \frac{q^2\alpha}{2\epsilon L} \;+\; \frac{2\pi q Q_r}{3\epsilon L^3} \;+\; O(L^{-5}), \tag{5.4}$$

where α is the Madelung constant of the supercell lattice (1.75 for the rock salt NaCl structure of PbSe), L is distance between defects, and ϵ is the dielectric constant which is calculated to be equal to 594 (including both ion-clamped ion-clamped and ionic contributions) for PbSe using density functional perturbation theory as implemented in VASP [46–48]. The first two terms are the monopole and quadrupole corrections, where Q_r is the second radial moment of the charge density. In Ref. [44] it is found that these terms are not affected by the choice of the exchange-correlation functional. Higher order terms $O(L^{-5})$ are neglected due to their minimal contributions. All together, the image charge correction term is calculated to have a maximum value of ≈ 7 meV in this work for q $\pm$ 2 charges, which is low due to the high dielectric constant of PbSe.

5.2.2 Calculation of isothermal solvus boundaries

The most dominant defect is determined by the position of the electron chemical potential, μ_e in Eqn. (5.1). It is the additional energy of electrons in our system, and is set to range in values around the energies of the VBM and CBM (conduction band minimum) for plots showing the variation of defect formation energies as functions of electron chemical potential. Under the assumption of dilute limit of defect concentrations, the number of free charge carriers in the compound is controlled by the number of electrons charged defects can either donate to or accept from the bands. It is calculated as a function of temperature T and sets of chemical potentials μ_α, representing different regions of phase equilibrium involving the PbSe phase, by numerically solving the charge-neutrality condition,

$$n \ - \ p \ = \ \sum_d q_d c_{d,q}, \tag{5.5}$$

where n and p are the free carrier concentrations of electrons and holes given by [95],

$$\begin{aligned} n \ &= \ \int_{E_{CBM}}^{+\infty} n(E) f(E;\mu_e,T) dE, \\ p \ &= \ \int_{-\infty}^{E_{VBM}} n(E)[1 \ - \ f(E;\mu_e,T)] dE, \end{aligned} \tag{5.6}$$

where $n(E)$ is the density of states of the defect-free crystal that is calculated using DFT (with a high k-point mesh) in this work, and $f(E;\mu_e,T)$ is the Fermi-Dirac distribution. In the dilute limit of defect concentrations, the concentration $c_{d,q}$ of a particular defect in the structure is given by the Botlzmann distribution as in Ref. [95],

$$c_{d,q} \ = \ N_{site}^{d,q} N_{sym}^{d,q} e^{-\Delta E_{d,q}/kT}, \tag{5.7}$$

where $N_{site}^{d,q}$ is the number of defect sites per formula unit of PbSe and $N_{sym}^{d,q}$ is the number of geometrically distinct but symmetrically equivalent ways of adding defect d with charge state q to a site.

The solvus boundaries of PbSe in the X-Pb-Se systems are calculated by summing over concentrations of each defect d, weighted by $-n_\alpha^d$, which is the change in composition of the XPbSe phase due to that defect, and is given by [96],

$$n_\alpha \ = \ \sum_d -n_\alpha^d c_{d,q}. \tag{5.8}$$

When calculated under different sets of chemical potentials μ_α, which represent different phase equilibrium regions between PbSe and other compounds in the phase diagram, and at a particular temperature T, we obtain one data point of the solvus boundary for each phase equilibrium region. For example, at a fixed temperature T the set of chemical potentials corresponding to the three-phase equilibrium between PbSe, Pb, and $PbCl_2$ in the Cl-Pb-Se phase diagram gives one data point: the composition of the PbSe single phase boundary that is connected to both the $PbCl_2$ and Pb phases. Similarly, the set of chemical potentials corresponding to three-phase equilibrium between

PbSe, Se, and $PbCl_2$ gives one data point: the composition of the PbSe single phase boundary that is connected to both the $PbCl_2$ and Se phases. To determine the behavior of the PbSe solvus boundary between these 2 data points, it is first noted that there is one linear combination of chemical potentials that differ between neighboring three-phase equilibria (because only one phase is different between the two set of equilibria). Based on this, the chemical potentials between the neighboring three-phase equilibria are interpolated to get several sets of chemical potentials, with each set corresponding to a two-phase equilibria between the two phases in common between the two sets of three-phase equilibria (in the example above, this would be PbSe and $PbCl_2$). Determining the composition of PbSe at each of these two-phase equilibria chemical potentials fills in the PbSe single phase boundary curve. An additional complication occurs when we go from a three-phase region (such as PbSe-Pb-$PbCl_2$ in Cl-Pb-Se) to a two-phase region (PbSe-Pb) on the binary boundary of the phase diagram since, according to the example above, the Cl chemical potential is not well defined there. This is dealt with as follows: starting with the chemical potentials of the PbSe-Pb-$PbCl_2$ phase region, we sequentially subtract from them the chemical potential of Cl. Since there is technically no lower bound for the chemical potential of Cl in PbSe-Pb, the variables of the employed interpolation scheme are varied until the single phase boundary approached the binary edge of the plot and the choice of these variables no longer affected the resulting solvus boundaries.

5.2.3 Computational details

We use DFT as implemented in the Vienna Ab-initio Simulation Package (VASP) [50–53] to calculate energies of the defect and host supercells. Ion-electron interactions were described using the Projector Augmented Wave (PAW) potentials [22–24] utilizing the generalized gradient approximation (GGA) with the exchange-correlation functional of Perdew, Burke, and Ernzerhof (PBE) [18]. The $5d^{10}6s^26p^2$ electrons of Pb, $4s^24p^4$ electrons of Se, $3s^23p^5$ electrons of Cl, $5s^25p^5$ electrons of I, $5s^25p^3$ electrons of Sb, $5d^{10}6s^26p^3$ electrons of Bi, and $4d^{10}5s^25p^1$ electrons of In are treated as valence states in the PAW potentials. All supercell calculations are performed on a 5 x 5 x 5 supercell of the primitive cell and contain 250 atoms. The cutoff energy of plane wave basis was set to 400 eV, a Gaussian smearing width of 0.05 eV is used to smear electron occupations, and integrations over the first Brillouin zone are made using a 2 x 2 x 2 Monkhorst-Pack k-point grid set [54]. Unit cell parameters and atomic positions are relaxed based on an energy convergence

criteria of 10^{-4} eV, and a final static calculation is performed for each defect to obtain accurate total energies.

5.3 Results and Discussion

Using GGA for exchange-correlation results in a calculated direct band gap of 0.41 eV at the L point, which over-estimates but is in fairly good agreement with the experimentally obtained value of 0.28 eV at room temperature [63, 97, 98]. Previous calculations in Refs. [99–101] show that including spin-orbit coupling (SOC) effects reduces the gap to near zero or negative values, representative of a metal, whereas the GW method, or the use of hybrid HSE03 functionals, with and without SOC, leads to band gaps of ≈ 0.13 eV and 0.58 eV, respectively, which are both less accurate than just PBE-GGA. Thus, GGA gives a fairly accurate band gap without any underestimation, which is why hybrid functionals or SOC were not considered in our calculations.

5.3.1 Cl, Br, and I in PbSe

Defect formation energies of the various point defects, as mentioned in the previous section, in the Br-Pb-Se and Na-Pb-Se systems are shown in Figs. 5.1 and 5.2, respectively. They are plotted as a function of electron chemical potential or Fermi level μ_e for different regions of three-phase equilibrium (listed above each plot) that contain the PbSe phase in these systems. The slope of the line corresponds to the charge state. According to the methodology presented in the previous chapter, shallow defects with delocalized charge that are shown with dashed lines in these figures (and the rest) are precluded from the calculation, whereas those shown with solid lines that are deep localized charged defects are included in the calculation of isothermal solvus boundaries in these systems. As described in Section 2.2, the dominant defects (defects with highest concentrations) of a system are determined by calculating the equilibrium μ_e as a function of temperature and atomic chemical potentials by numerically solving the charge neutrality condition in Eqn. 5.5. With an increase in temperature, μ_e is expected to equilibrate closer to transition points between donor defects and acceptor defects to satisfy charge balancing. In cases of both the Cl-Pb-Se and I-Pb-Se systems, the equilibrium μ_e is positioned where, from Figs. 5.1 and 5.2, the lowest energy defects are donor defects Cl_{Se}^{+1} and I_{Se}^{+1} in the Pb-rich regions (points A) of Pb-PbSe-$PbCl_2$ and

Pb-PbSe-PbI_2 regions, respectively. These defects are expected to be most stable due to the -1 valence charge state exhibited by these halogens which when substituted on a Se atom with a -2 valence charge lead to a net charge of +1. The Se-rich regions (points B) in these systems are dominated by acceptor V_{Pb}^{-2} defects in addition to the above mentioned defects.

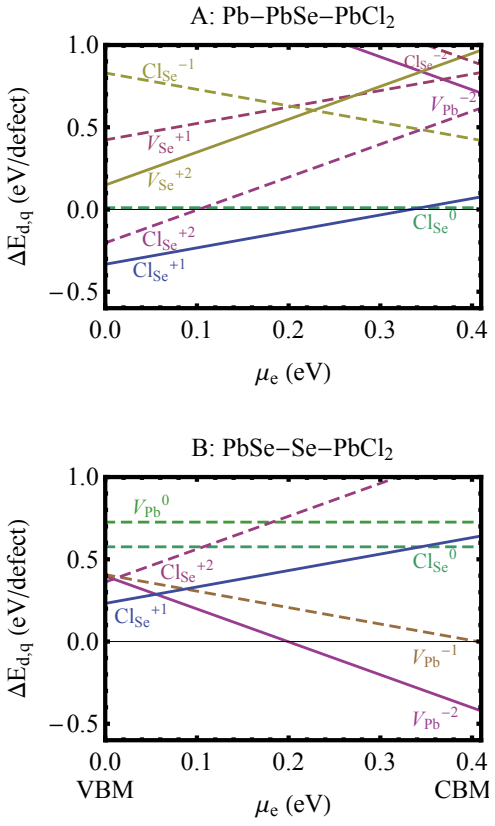

Figure 5.1: (Color online) Defect formation energies, $\Delta E_{d,q}$ of the lowest energy intrinsic and Cl-containing defects in PbSe as a function of Fermi level, μ_e (relative to VBM) in different three phase equilibrium regions of PbSe in the Cl-Pb-Se phase diagram. Solid lines indicate defects included in the calculation of the Cl-Pb-Se phase diagram, whereas dashed lines indicate excluded defects.

Continuing to follow the methodology of calculating defect concentrations detailed in Section 2.2 enables the mapping of solvus boundaries of the PbSe phase as a function of temperature. Figs. 5.3 and 5.4 show the calculated isothermal sections of the PbSe solvus boundaries upon the addi-

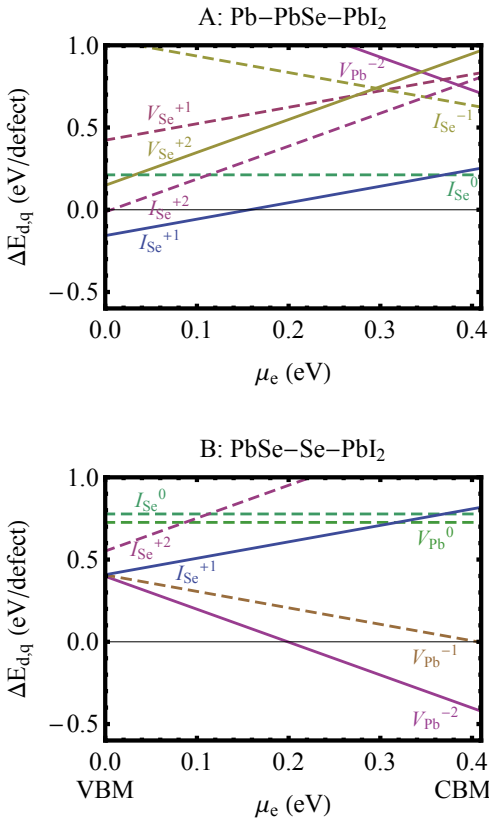

Figure 5.2: (Color online) Defect formation energies, $\Delta E_{d,q}$ of the lowest energy intrinsic and I-containing defects in PbSe as a function of Fermi level, μ_e (relative to VBM) in different three phase equilibrium regions of PbSe in the I-Pb-Se phase diagram. Solid lines indicate defects included in the calculation of the I-Pb-Se phase diagram, whereas dashed lines indicate excluded defects.

tion of Cl and I, respectively, at 573 K. This temperature was chosen as it falls within the range of operating temperatures for many thermoelectric applications. Red boxes in these figures show the expanded views of the isothermal section, next to which are the full ternary phase diagrams. In addition to the above diagrams, we have also plotted the solvus boundary of the PbSe phase in the Br-Pb-Se system at 573 K in Fig. 5.5 for comparison since Cl, Br, and I are all halogens falling in the same s^2p^5 column of the periodic table (refer to the previous chapter for a plot of defect formation energies in Br-Pb-Se). In all three figures, we have marked with dashed lines a path for one-to-one replacement of Se with the dopant, i.e., as PbX_xSe_{1-x} (where X = Cl, Br, I).

This makes it evident from all three phase diagrams that a greater amount of dopant can be added by atomic fraction to PbSe when they are added as a one-to-one replacement for Pb in a Pb-rich environment (chemical potentials at points A representing region Pb-PbSe-PbX_2) than when they are added to PbSe in a Se-rich environment, i.e., chemical potentials at points B representing the region PbSe-Se-PbX_2. In fact, the amount of dopant that can be added in a Pb-rich environment, without precipitating secondary phases, is about a factor of 4 (for Cl and Br) or 14 (for I) greater (at 573 K) than the amount of dopant that can be added to PbSe is a Se-rich environment. This can be explained by the magnitude of defect formation energies at the positions of equilibrium Fermi level μ_e at 573 K near the transition points between donor and acceptor defects: defect formation energies at or near equilibrium Fermi level μ_e are lower in Pb-rich regions than in Se-rich regions leading to higher defect concentrations and thus higher dopant solubilities in Pb-rich regions. It can also be seen by comparing the three phase diagrams that dopant solubilities in these systems follow the order x(Br) > x(Cl) > x(I). This is expected if we compare the atomic radii of Se to these dopants: Br (94 pm) is closer in size to Se (103 pm) than Cl (79 pm), which is in turn closer in size to Se than I (115 pm) [104, 105].

There is also a significant effect observed on calculated electrical properties of doped samples in these systems based on growth conditions. Samples prepared in a Pb-rich environment at chemical potentials of points A are predicted to be n-type, whereas those prepared in a Se-rich environment at chemical potentials of points B are predicted to be p-type due to the dominance of donor defects in the former and acceptor defects in the latter regions of the phase diagram (see Figs. 5.1 and 5.2). As can be seen from Figs. 5.3, 5.4, and 5.5, even a slight change in synthesis routes in the order of hundredths of atomic percent can lead to stabilization in a different region of phase diagram that can drastically change the electrical properties of a thermoelectric material. Carrier concentrations of electrons in Pb-rich regions of these systems at 573 K follow the order of dopant solubilities: 2.8 x 10^{20} electrons/cm^3 for Br, 2.3 x 10^{20} electrons/cm^3 for Cl, and 5.4 x 10^{19} electrons/cm^3 for I, whereas hole concentrations follow exactly a reverse order: 2.3 x 10^{19} holes/cm^3 for Br, 2.6 x 10^{20} holes/cm^3 for Cl, and 3.7 x 10^{19} holes/cm^3 for I. The reason for this trend reversal in Se-rich regions from Pb-rich regions is that the transition points of charge neutrality between X_{Se}^{+1} and V_{Pb}^{-2} in these systems shifts further towards the VBM from I to Cl to Br, thus leading to the equilibrium Fermi level μ_e being positioned closer to the middle of band gap where the defect

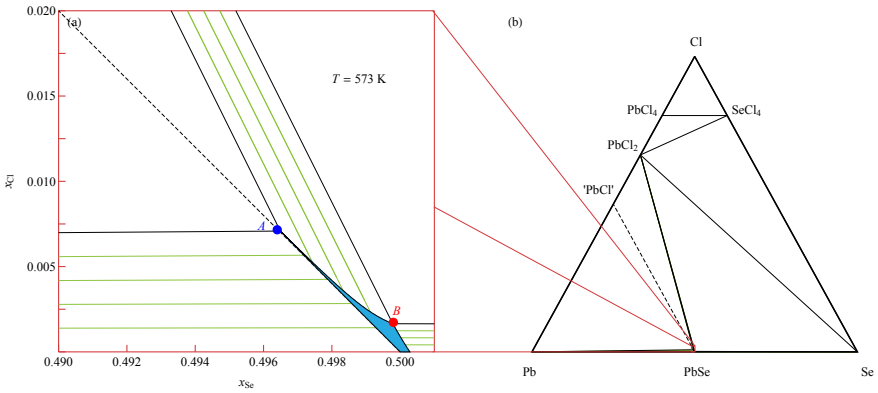

Figure 5.3: (Color online) (a) Isothermal section of the Cl-Pb-Se phase diagram calculated at T = 573 K showing the single-phase region of PbSe in blue, and green tie-lines representing two-phase regions between it and other compounds that are shown in the full isothermal section plot in (b). Dashed line represents a path between PbSe and a hypothetical PbCl compound for one-to-one replacement of Se with Cl, i.e., as $PbCl_xSe_{1-x}$. Point A (blue circle) marks the point of maximum Cl solubility in the three-phase region Pb-PbSe-$PbCl_2$ where a sample is predicted to exhibit n-type conductivity, whereas point B (red circle) marks the point of Cl solubility in the three-phase region PbSe-Se-$PbCl_2$ where a sample is predicted to exhibit p-type conductivity.

formation energies of V_{Pb}^{-2} are lower, leading to higher hole concentrations, in the order mentioned above. Hall measurements in Ref. [106] measured a monotonically increasing electron concentration beyond 3.8 x 10^{20} electrons/cm^3 of Cl doped PbSe samples with amount of Cl, which agrees with our prediction of a higher concentration at the solubility limit of Cl in PbSe at 573 K.

5.3.2 Sb and Bi in PbSe

Figs. 5.6 and 5.7 show the defect formation energies of point defects in PbSe upon the addition of Sb and Bi as dopants, respectively. Looking at the atomic radii of these elements from Refs. [104, 105], we note their order as r(Se) (103 pm) < r(Sb) (133 pm) < r(Bi) (143 pm) < r(Pb) (154 pm). The atomic size of Sb falls closer to the size of Pb than to that of Se making its substitution on a Pb site more likely than on a Se site. This is confirmed in our defect calculations in Fig. 5.6 where we see the defect formation energy of Sb as a single hole Sb_{Se}^{-1} acceptor defect in the Pb-rich Pb+PbSe+Sb region (point A) higher in energy than as a single electron Sb_{Pb}^{+1} donor defect in the

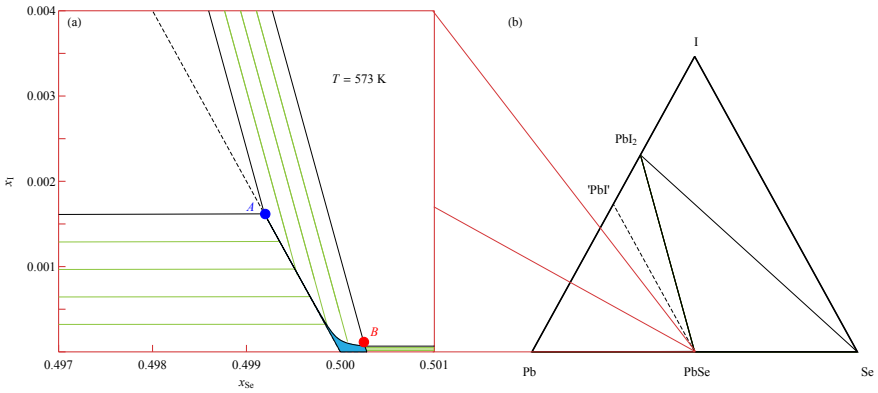

Figure 5.4: (Color online) (a) Isothermal section of the I-Pb-Se phase diagram calculated at T = 573 K showing the single-phase region of PbSe in blue, and green tie-lines representing two-phase regions between it and other compounds that are shown in the full isothermal section plot in (b). Dashed line represents a path between PbSe and a hypothetical PbI compound for one-to-one replacement of Se with I, i.e., as PbI_xSe_{1-x}. Point A (blue circle) marks the point of maximum I solubility in the three-phase region Pb-PbSe-PbI_2 where a sample is predicted to exhibit n-type conductivity, whereas point B (red circle) marks the point of I solubility in the three-phase region PbSe-Se-PbI_2 where a sample is predicted to exhibit p-type conductivity.

Se-rich regions of PbSe+Sb+Sb_2Se_3 region (point B) and PbSe+Sb_2Se_3+Se region (point C), thus resulting in low dopant solubilities in the Pb-rich region. Sb exhibits single electron donor and single hole acceptor properties since it has three electrons in its valence $5p^3$ orbital, causing it to exhibit a valence of -3 and +3. Similar is the case with Bi, which has three electrons in its valence $6p^3$ orbital. Its size is much closer to that of Pb than Se, which makes its substitution on a Pb site even more likely than on a Se site. This is verified from the defect energy plots in Fig. 5.7. The Pb-rich region (point A), similar to the case of Sb as a dopant, is dominated by V_{Se}^{+2} and Bi_{Se}^{-1} defects (Sb_{Se}^{-1} in case of Sb), but now in the case of Bi is also dominated by the Bi_{Pb}^{+1} defect, which is much lower in energy compared to the Sb_{Pb}^{+1} defect. This is a consequence of the atomic size of Bi being closer to that of Pb than that of Sb to Pb, making its substitution on a Pb site more energetically favorable. It is also a reason for the transition point of charge balance between donor defects (V_{Se}^{+2} in case of Sb and Bi_{Pb}^{+1} in case of Bi) and acceptor defects (Sb_{Se}^{-1} in case of Sb and Bi_{Se}^{-1} in case of Bi) to be shifted from closer to VBM in the case of Sb to almost at the CBM in the case of Bi when chemical potentials represent their respective Pb-rich regions. This causes the

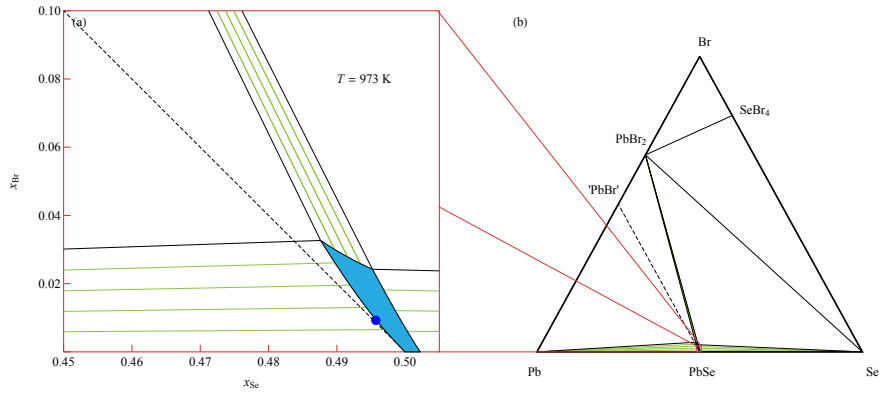

Figure 5.5: (Color online) (a) Isothermal section of the Br-Pb-Se phase diagram calculated at T = 573 K showing the single-phase region of PbSe in blue, and green tie-lines representing two-phase regions between it and other compounds that are shown in the full isothermal section plot in (b). Dashed line represents a path between PbSe and a hypothetical PbBr compound for one-to-one replacement of Se with Br, i.e., as $PbBr_xSe_{1-x}$. Point A (blue circle) marks the point of maximum Br solubility in the three-phase region Pb-PbSe-$PbBr_2$ where a sample is predicted to exhibit n-type conductivity, whereas point B (red circle) marks the point of Br solubility in the three-phase region PbSe-Se-$PbBr_2$ where a sample is predicted to exhibit p-type conductivity.

calculated Fermi level μ_e at 573 K to equilibrate closer to the middle of the gap in case of Sb at point A where where the acceptor Sb_{Se}^{-1} defects are stable, causing samples prepared in a Pb-rich growth environment to be p-type with a hole concentration of 8.2 x 10^{17} holes/cm^3, which is low for thermoelectric applications due to high formation energies. In a Pb-rich environment with Bi as a dopant, it equilibrates closer to the CBM, but now since the donor Bi_{Pb}^{+1} defect dominates majority of the low energy region, these samples are expected to exhibit n-type electrical conduction properties with a carrier concentration of 1.1 x 10^{18} electrons/cm^3.

When samples are prepared at chemical potentials representing the dopant-rich regions (points B) of both Sb-Pb-Se and Bi-Pb-Se phase diagrams, the Fermi level is at equilibrium where dopant substitutions on the Pb site, donating one electron to the lattice, become the prominent defect, thus causing n-type conduction in both samples. Since the atomic size of Bi is more similar to Pb than the atomic size of Sb, the defect formation energy of the Bi_{Pb}^{+1} defect is lower compared to the Sb_{Pb}^{+1} defect, causing the charge balance transition point and the equilibrium Fermi level in this

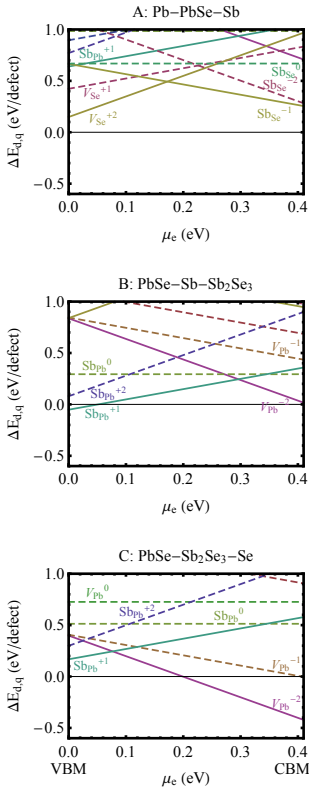

Figure 5.6: (Color online) Defect formation energies, $\Delta E_{d,q}$ of the lowest energy intrinsic and Sb-containing defects in PbSe as a function of Fermi level, μ_e (relative to VBM) in different three phase equilibrium regions of PbSe in the Sb-Pb-Se phase diagram. Solid lines indicate defects included in the calculation of the Sb-Pb-Se phase diagram, whereas dashed lines indicate excluded defects.

region to be slightly above mid-gap in case of Sb and near the CBM in case of Bi (see Figs. 5.6 and 5.7). At these points, the lower defect formation energy of Bi_{Pb}^{+1} results in a higher carrier concentration of 4.0 x 10^{19} electrons/cm^3 compared to 2.5 x 10^{18} electrons/cm^3 in case of Sb. This is the same reason for the higher hole concentration of 1.9 x 10^{19} holes/cm^3 in the case of Sb than 1.1 x 10^{19} holes/cm^3 in case of Bi in the Se-rich regions (points C) of these systems. Samples prepared at chemical potentials of these regions are dominated by the V_{Pb}^{-2} defects, thus exhibiting p-type electrical conduction properties.

The two dopants, Sb and Bi, when added to PbSe exhibit electrical conduction properties of

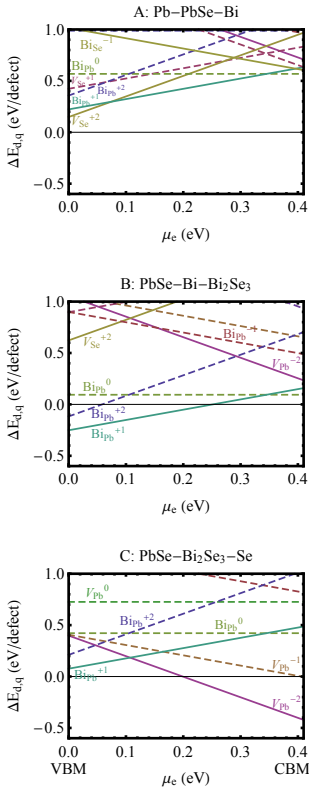

Figure 5.7: (Color online) Defect formation energies, $\Delta E_{d,q}$ of the lowest energy intrinsic and Bi-containing defects in PbSe as a function of Fermi level, μ_e (relative to VBM) in different three phase equilibrium regions of PbSe in the Bi-Pb-Se phase diagram. Solid lines indicate defects included in the calculation of the Bi-Pb-Se phase diagram, whereas dashed lines indicate excluded defects.

both type: n-type at dopant-rich regions (points B) of the phase diagrams, and p-type at Se-rich regions (points C) of the phase diagrams. This makes both Sb and Bi amphoteric dopants in PbSe, and not just n-type carriers as assumed by many studies [107]. The amphoteric nature of Sb in PbTe was confirmed by nuclear magnetic resonance (NMR) spectroscopy experiments in Ref. [108] and Mössbauer spectroscopy in Ref. [109]. Thus, in this work, since both the Sb donor and acceptor defects dominate the defect energy landscape in PbSe, we predict an amphoteric behavior of Sb also in PbSe. The amphoteric nature of Bi in PbSe has been evidenced in a study of electrical properties of Bi-doped PbSe films in Ref. [110], thus verifying our calculations in this work.

Figs. 5.8 and 5.9 show the resulting solvus boundaries of the PbSe phase at 573 K upon the addition of dopants Sb and Bi, respectively. As discussed above, formation energies of defects in Pb-rich regions of both systems are higher (at equilibrium Fermi levels) relative to those in the other two regions (points B and C) leading to lower carrier concentrations. This also leads to low dopant solubilities in these regions as seen from the calculated phase boundaries at point A. However, dopant solubilities are much higher in both the dopant-rich (point B) and Se-rich (point C) regions of the phase diagram since at 573 K the Fermi level equilibrates where defect formation energies are lower, which also lead to higher carrier concentrations. Without precipitating secondary phases, the amount of Bi that can be added to PbSe in Bi-rich and Se-rich regions of the phase diagram are more than a factor of 3 higher than those of Sb, which is in agreement with room temperature Hall carrier-concentration measurements in Ref. [107] that suggest a significantly higher solubility of Bi in PbSe than Sb. For reasons discussed above, this is expected as the atomic size of Bi is closer to that of Pb than that of Sb, making its substitution on a Pb-site more energetically favorable, thus explaining its higher solubility. In both phase diagrams, we have again marked with dashed lines a path for one-to-one replacement of Pb with a dopant, i.e., as $Pb_{1-x}X_xSe$ (where X = Sb, Bi). It can be seen from both the diagrams that the largest atomic fraction of dopant can be obtained by adding the dopant to PbSe in a ratio of two dopant atomic substitutions for three Pb atoms, i.e., in a ratio less than one-to-one, which leaves one Pb vacancy, the defect formation energy of which (as seen from Figs. 5.6 and 5.7) dominates the chemical potential regions of points B and C. From Figs. 5.8 and 5.9, it is evident that points B and C are within $\approx$ 0.001 at.% and less of each other in composition space, and as shown above, represent samples of opposite electrical conduction properties: n-type at point B and p-type at point C. This shows the importance of having information on phase solvus boundaries of a thermoelectric material being synthesized since even a change of 0.001 at.% in sample composition can significantly affect its electrical properties.

5.3.3 In in PbSe

In our final case study of In as a dopant in PbSe, defect formation energies of defects in this system are plotted in Fig. 5.10, and the resulting solvus boundaries of the InPbSe phase at 573 K are shown in Fig. 5.11. The atomic size of In is 156 pm [104, 105], which is very close to that of Pb at 154 pm, making it energetically favorable for substitution on a Pb site with a +1 net charge by losing its three valence electrons in its 5s and 5p orbitals. This is confirmed from our results in

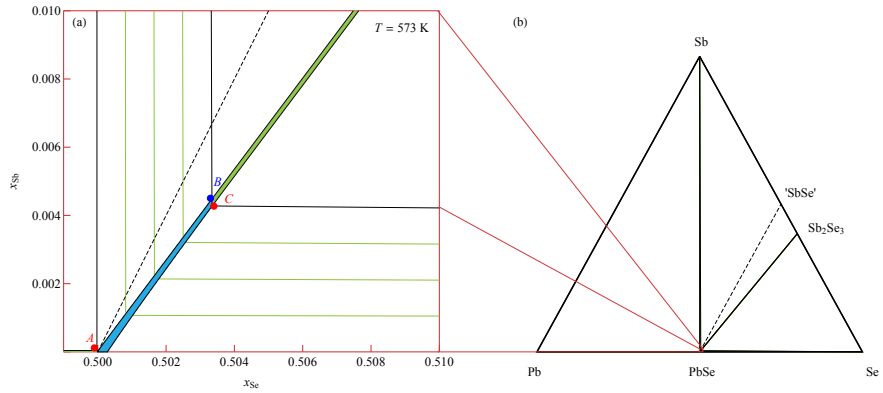

Figure 5.8: (Color online) (a) Isothermal section of the Sb-Pb-Se phase diagram calculated at T = 573 K showing the single-phase region of PbSe in blue, and green tie-lines representing two-phase regions between it and other compounds that are shown in the full isothermal section plot in (b). Dashed line represents a path between PbSe and a hypothetical SbSe compound for one-to-one replacement of Pb with Sb, i.e., as $Pb_{1-x}Sb_xSe$. Point B (blue circle) marks the point of maximum Sb solubility in the three-phase region PbSe-Sb-Sb_2Se_3 where a sample is predicted to exhibit n-type conductivity, whereas point C (red circle) marks the point of Sb solubility in the three-phase region PbSe-Sb_2Se_3-Se where a sample is predicted to exhibit p-type conductivity.

Fig. 5.10 where In_{Pb}^{+1} defects dominate the energy landscape in three out of the four regions (points A, B, and C), thus resulting in n-type behavior in these regions. The maximum calculated carrier concentration is 2.4 x 10^{18} electrons/cm^3 at 573 K (which is lower than those measured in Refs. [111, 112]) at point B of the phase diagram in a direction that suggests a one-to-one replacement of Pb with In. It is also the direction along which, from Fig. 5.11, we obtain the peak solubility of In at 573 K and thus is the most efficient doping strategy for doping PbSe samples with In. Samples prepared in a Se-rich growth environment exhibit p-type conductivity with a concentration of 3.6 x 10^{19} holes/cm^3, due to the dominance of V_{Pb}^{-2} defects.

5.4 Conclusions and outlook

To summarize, we have used DFT calculations on a large number of neutral and charged supercells of PbSe containing intrinsic and extrinsic point defects with Cl, Br, I, Sb, Bi, and In as dopants. These results were used as input to a dilute-limit approximation based ternary statistics mechanics

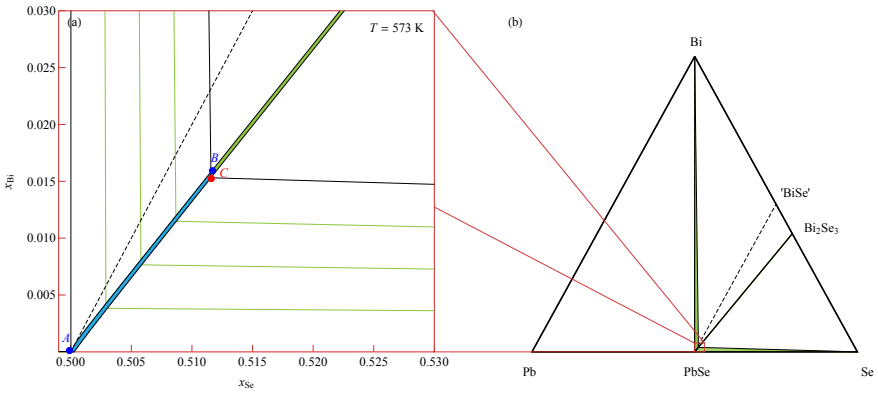

Figure 5.9: (Color online) (a) Isothermal section of the Bi-Pb-Se phase diagram calculated at T = 573 K showing the single-phase region of PbSe in blue, and green tie-lines representing two-phase regions between it and other compounds that are shown in the full isothermal section plot in (b). Dashed line represents a path between PbSe and a hypothetical BiSe compound for one-to-one replacement of Pb with Bi, i.e., as $Pb_{1-x}Bi_xSe$. Point B (blue circle) marks the point of maximum Bi solubility in the three-phase region PbSe-Bi-Bi_2Se_3 where a sample is predicted to exhibit n-type conductivity, whereas point C (red circle) marks the point of Bi solubility in the three-phase region PbSe-Bi_2Se_3-Se where a sample is predicted to exhibit p-type conductivity.

model to obtain carrier and defect concentrations, and ultimately solvus boundaries of the PbSe phase in the respective ternary systems.

Dopants Cl, Br, and I are known to be anion dopants in PbSe with dopants substitutions on the Se site, and this is confirmed from our calculated defect formation energies where we find X_{Se}^{+1} (X = Cl, Br, I) donor defects to be the dominant defects in Pb-rich regions of these systems. These are also the regions of maximum observed solubility in each system, with one-to-one replacement of Se with the dopant, and predicted n-type conductivity. Dopant solubilities follow the order: Br > Cl > I, which is explained in terms of atomic sizes, with the atomic size of Br being closest to that of Se, making its substitution on the anion site energetically favorable. On the other hand, dopants Sb and Bi are predicted to be amphoteric in PbSe with substitutions on both the cation and anion site, as observed from experiments. The dopant-rich regions of their phase diagrams are found to be dominated by cation site donor dopants X_{Pb}^{+1} (X = Sb, Bi) leading to n-type conductivity. A slight change of composition leads to stabilization in the Se-rich regions of these phase diagrams

which are dominated by V_{Pb}^{-2} defects, and thus p-type conductivity.

To conclude, results here show the importance of having information on phase stability of doped semiconductors or thermoelectric materials. Calculations in this work enable the estimation of dopant solubilities and carrier concentrations, which are strongly varying functions of temperature and alloy composition, and an understanding of these dependencies allows for finer control over the electronic properties of a thermoelectric material. Even a slight change in alloy composition or synthesis route to sample preparation can result in drastically different dopant concentrations and electrical conductivity behavior. Figures in this chapter have been created using the LevelScheme scientific figure preparation system [102].

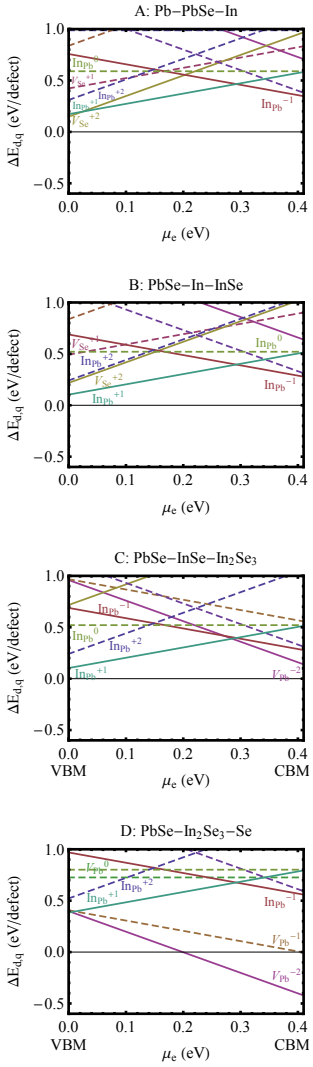

Figure 5.10: (Color online) Defect formation energies, $\Delta E_{d,q}$ of the lowest energy intrinsic and In-containing defects in PbSe as a function of Fermi level, μ_e (relative to VBM) in different three phase equilibrium regions of PbSe in the In-Pb-Se phase diagram. Solid lines indicate defects included in the calculation of the In-Pb-Se phase diagram, whereas dashed lines indicate excluded defects.

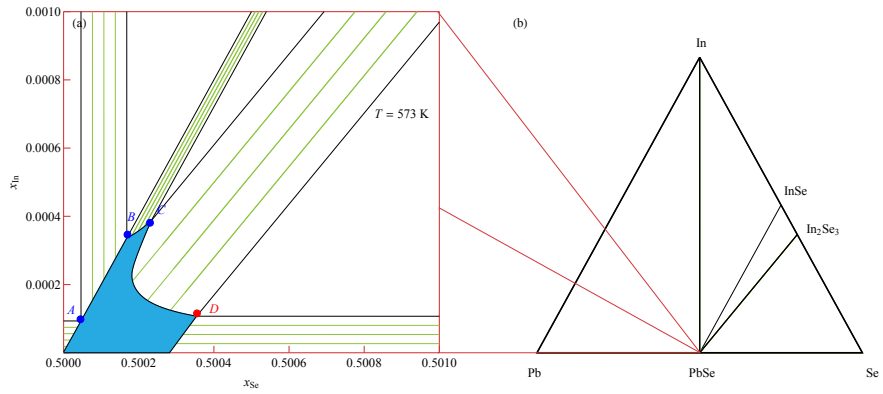

Figure 5.11: (Color online) (a) Isothermal section of the In-Pb-Se phase diagram calculated at T = 573 K showing the single-phase region of PbSe in blue, and green tie-lines representing two-phase regions between it and other compounds that are shown in the full isothermal section plot in (b). Point C (blue circle) marks the point of maximum In solubility in the three-phase region PbSe-InSe-In_2Se_3 where a sample is predicted to exhibit n-type conductivity, whereas point D (red circle) marks the point of In solubility in the three-phase region PbSe-In_2Se_3-Se where a sample is predicted to exhibit p-type conductivity.

Chapter 6

Phase stability in nanoscale material systems: Extension from bulk phase diagrams

Adapted from Ref. [113] with permission from The Royal Society of Chemistry.

6.1 Introduction

Traditional phase diagrams show equilibrium solubility lines determined for a bulk system, which as defined in Ref. [114], consist of phases and interface layers with all of their dimensions greater than 100 nm such that the material resembles the bulk. However, when the dimensions of a significant fraction of particles is reduced to approximately below 100 nm, it has been observed in many experimental works, including and not limited to Refs. [115–120], that these equilibrium lines are shifted from their original positions in the bulk phase diagram with the amount of shift depending on particle size, surface to volume ratio, and the material system. This not only changes the solubilities [121], and temperature and compositions of the invariant reactions [122] of the phase diagram, but also affects material properties such as electronic [123], magnetic [124], optical [125], and catalytic [126] properties. Additionally, the stabilization of phases that might otherwise be metastable with respect to the bulk ground state may also be promoted. These changes are attributed to the size effect caused due to the larger energies associated with surfaces.

The phenomenon of suppression of melting points in pure elements with a decrease in particle

size was first experimentally shown about 60 years ago [127]. Recently, it was shown by Chen *et al* in Ref. [128] that the melting points of Bi-Sn, In-Sn, and Pb-Sn alloys decreased more rapidly as a function of particle radius than those of the constituent metals. Additionally, in the work by Jesser *et al* [129] on the GaAs-GaSb pseudo-binary system, complete solid solubility was observed for particles of sizes 10-50 nm in regions of the phase diagram where a miscibility gap was expected from its bulk phase diagram. In the electronics industry, transistor sizes continue to pursue Moore's law [130] from current commercially used node sizes of 22 nm and below. It is important to note that even at the 22 nm technology node there are dimensions in the technology roadmap already less than 22 nm. At these sizes, we show that the change in alloy thermodynamic and phase stability from bulk will be pronounced. This makes the development of a thermodynamic model at these dimensions critical. Phase diagrams exhibited by materials used in devices are expected to be considerably different from their bulk counterparts. In compound semiconductors for example, samples are prepared with small particle sizes when one may not be able to achieve the target band gap due to changing miscibility. Thus, the evaluation of phase diagrams for systems containing particles of nanoscale dimensions is valuable to the process of selection of material alloys and fine-tuning of their composition in order to achieve the desired properties.

As materials/grain sizes are made smaller, surface to volume ratio increases. This leads to a much greater contribution of surface energy to the total Gibbs free energy of the material, and must be included in the calculation of phase equilibria. In this work, we have evaluated the phase diagrams for one semiconductor and two metallic systems at dimensions of several tens of nanometers (termed as nano dimensions): Au-Si, Ge-Si, and Al-Cu using the CALPHAD method [16] by adding a surface energy term to the excess Gibbs free energy, which makes it a function of particle size in addition to composition and temperature [131]. For the initial model development, an isolated particle-in-melt based surface energy formalism is presented to test against a wide range of experimental data. The first system Au-Si was chosen because it is one of the few systems for which the amount of shift in equilibrium lines in the phase diagram was experimentally estimated based on phase transitions observed using *in-situ* microscopy of spherical nano-sized particles [132]. This is one of the reasons for the selection of the spherical particle model in this work as it makes possible a direct comparison between the calculated Au-Si phase diagram and experimental data. In addition, since spheres have the minimum surface area to volume ratio, particles with this shape

will be the lower bound of effects. In other words, the shift of phase equilibrium due to spherical particles will be the minimum compared to particles with other shapes (as shown in Table 6.1). We then proceed on to test extending the model on particle and non-particle based experimental data sets, and calculate the phase diagram at nano dimensions of Ge-Si, one of the most widely used and technologically important semiconductor alloy. Lastly, the phase diagram of Al-Cu nano-sized particles is also calculated. A comparison is made against measured experimental data on surface tension of spherically shaped alloy samples, and melting points of Al and Cu nano-particles. Unlike the first two systems, the bulk Al-Cu phase diagram exhibits numerous intermetallic phases, and thus its phase diagram at nanoscale dimensions should incorporate surface energies of all the equilibrium phases. However, such data is usually unavailable for phases other than the liquid and ground-state phases of the pure elements. Thus, we resort to using Density Functional Theory (DFT) [14, 15] to calculate the surface energy for one of the intermetallic phases Al_2Cu, which is then used in its thermodynamic model to calculate the phase diagram at these small dimensions. In our study we also identified areas for future model development that were beyond the current scope of our work, and point in the directions for future enhancements of the model in cases of thin films and dimensions below 5 nm.

Table 6.1: Surface area to volume ratio of different shapes of nano-particles.

Geometrical nanostructure	**Size** (a or r)	**Surface Area**	**Volume**	**Ratio of Surface Area/Volume**	**Coefficient of ratio**
Cube	a	$6a^2$	a^3	$\frac{6}{a}$	6
Regular Tetrahedron	a	$\sqrt{3}a^2$	$\frac{a^3}{6\sqrt{2}}$	$\frac{6\sqrt{6}}{a}$	14.7
Hexahedron	a,L; a/L = 1	$(6a^2 + 3\sqrt{3}a^2)$	$\frac{3\sqrt{3}a^3}{2}$	$\frac{4}{\sqrt{3}a}(1+\frac{\sqrt{3}}{2})$	4.3
Regular icosahedron	a	$5\sqrt{3}a^2$	$\frac{5(3+\sqrt{5})a^3}{12}$	$\frac{12\sqrt{3}}{(3+\sqrt{5})a}$	3.97
Sphere	r	$4\pi r^2$	$\frac{4\pi r^3}{3}$	$\frac{3}{r}$	3
Cylinder	r,H; r/H = 1	$4\pi r^2$	πr^3	$\frac{4}{r}$	4

6.2 Method and computational details

6.2.1 The CALPHAD method

The method of CALculation of PHAse Diagrams (or CALPHAD for short) has been widely utilized to calculate bulk phase diagrams and thermodynamic properties of multi-component systems [16]. It involves the use of Gibbs free energy models developed for various types of phases, such as random solutions (gases, liquids, and solids), sublattice phases, ionic phases, etc. Variables used in these models are calculated by fitting either to experimental data or *ab initio* calculations.

The CALPHAD method [16] is well established for calculating bulk phase diagrams, and is a good starting point for calculating phase equilibria in nanoscale systems. In this work, since we have considered surface effects on binary solution phases, thermodynamic models for only these types of phases will be described. The Gibbs free energy of a bulk random solution phase ϕ is given by,

$$G_m^{\phi,bulk} \;=\; G_{ref} \;+\; \Delta G_{mix}^{ideal} \;+\; \Delta G_{mix}^{xs}, \tag{6.1}$$

where G_{ref} is the sum of standard Gibbs energies of each component, ΔG_{mix}^{ideal} is the ideal mixing configurational entropy contribution to the Gibbs free energy of the solution phases, and ΔG_{mix}^{xs}, called the excess energy of mixing, takes into account all the non-ideal temperature dependent effects such as interaction between components, non-ideal configurational entropy, vibrational and electronic entropy, etc. Expanding each term, Eqn. (6.1) becomes,

$$\begin{aligned} G_m^{\phi,bulk} &= \sum_{i=A,B} x_i \; {}^oG_i^{bulk} \;+\; RT \sum_{i=A,B} x_i log_e x_i \;+\; \Delta G_{mix}^{xs} \\ &= x_A \; {}^oG_A^{bulk} \;+\; x_B \; {}^oG_B^{bulk} \;+ RT(x_A log_e x_A \;+\; x_B log_e x_B) \;+\; \Delta G_{mix}^{xs}, \end{aligned} \tag{6.2}$$

where x_A and x_B are mole fractions of components A and B of the phase, respectively, and ${}^oG_A^{\phi,bulk}$ and ${}^oG_B^{\phi,bulk}$ are the standard Gibbs energies of the phase containing only the pure component A and B, respectively. These are obtained from the Scientific Group Thermodata Europe (SGTE) database [26]. Functions in this database are based on measurements of heat capacity of single

element materials and alloys, which may or may not be accurate depending on the chosen material. An alternative way of obtaining these functions would be to use state-of-the-art methods to calculate configurational entropy by sampling the space of different atomic arrangements of an alloy, and also calculate vibrational entropy by computing its phonon spectrum. R is the gas constant, and T is the temperature. The excess Gibbs free energy of mixing ΔG^{xs}_{mix} is expanded according to the Redlich-Kister formalism [27] as,

$$\Delta G^{xs}_{mix} \;=\; x_A x_B \sum_v L^{\phi}_v (x_A \;-\; x_B)^v, \tag{6.3}$$

where v is the order of expansion ($v \;=\; 0$ for regular solution phases and $v \;=\; 1$ or above for non-regular solution phases), and L^{ϕ}_v is called the non-ideal interaction parameter. As the excess Gibbs free energy of mixing must include temperature dependency of other sources of entropy (non-ideal configurational, vibrational, and electronic) apart from ideal configurational entropy, these parameters are further expanded as,

$$L^{\phi}_v \;=\; A^{\phi}_v \;+\; B^{\phi}_v.T, \tag{6.4}$$

where A^{ϕ}_v and B^{ϕ}_v are user-defined parameters that are calculated and optimized in the CALPHAD method with available experimental data on positions of equilibrium lines in the phase diagram, phase thermodynamic properties such as enthalpy and entropy of mixing, etc., and/or similar data calculated from *ab initio* calculations, which is particularly useful in cases where no experimental data is available.

6.2.2 Extension of the CALPHAD method to nanoscale systems

The CALPHAD method is extended to nanoscale systems as explained by Park *et al* [131], where the total Gibbs free energy of a phase $G^{\phi,total}_m$ includes the dominant surface energy term, and is given by,

$$G^{\phi,total}_m \;=\; G^{\phi,bulk}_m \;+\; \Delta G^{\phi,surface}_m, \tag{6.5}$$

where $G^{\phi,bulk}_m$ is given by Eqn. (6.2). According to Gibbs [133], the molar surface Gibbs free energy is given by,

$$\Delta G_m^{\phi,surface} = A^{\phi,spec}.V^{\phi}.\sigma_s^{\phi}, \tag{6.6}$$

where $A^{\phi,spec}$ is the specific area of the phase ϕ given by a ratio of its absolute surface area to absolute volume, V^{ϕ} is its molar volume, and σ_s^{ϕ} is the interfacial/surface tension between the phase and its surroundings. In this work, the particles are assumed to be spherical in shape of radius r for reasons explained in the previous section, including the availability of experimental data [132]. The specific area of such a phase is given by,

$$A^{\phi,spec} = \frac{A^{\phi,abs}}{V^{\phi,abs}} = \frac{4\pi r^2}{\frac{4}{3}\pi r^3} = \frac{3}{r}. \tag{6.7}$$

By inserting appropriate expressions in the equation above, this methodology can be extended to any geometrical shape, such as thin films or 3D structures. In the work by Eichhammer *et al* [134], a solid nanowire in contact with a hemispherical alloy nano-particle of different sizes was modeled to calculate its corresponding phase equilibria. As mentioned earlier, for more complicated particle shapes that are multi-facetted, the specific area above (or the surface area to volume ratio) is even higher than that for a sphere. For example in the case of an icosahedron, a regular polyhedron with 20 equilateral triangular faces, the specific area is $A^{\phi,spec} = \frac{3.970}{r}$ [135, 136]. This is slightly higher than that for a sphere, causing a shift in the phase equilibria in a direction such that the shift in phase equilibria due to spherical particles still remain at the minimum. Fig. 6.1 shows this effect in the case of the Ge-Si system, which will be discussed in detail in the subsequent section. This makes it more likely that particles form in the spherical shape than any other shape so as to obtain the lowest molar surface Gibbs free energy and total Gibbs free energy. Thus the phase diagrams calculated for spherical particle systems represent the lowest energy and most stable configuration for nano-particles.

Inserting Eqn. (6.7) into (Eqn. (6.6)) above, we get,

$$\Delta G_m^{\phi,surface} = \frac{3.V^{\phi}.\sigma_s^{\phi}}{r}. \tag{6.8}$$

For some systems, information on grain-size distribution is available from experiments, in which case their weighted averages could be used to calculate the surface Gibbs energy. The corresponding Kelvin equation given by,

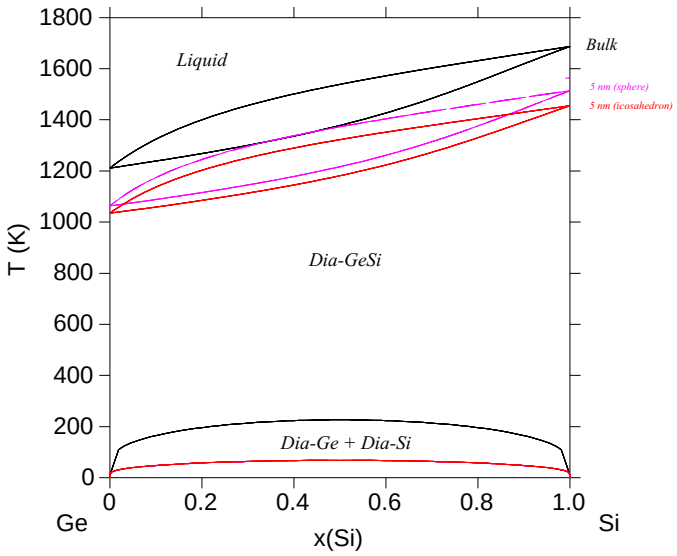

Figure 6.1: (Color online) Phase diagram of the Ge-Si alloy system calculated for two particle shapes - sphere and a regular icosahedron, both for a particle size of 5 nm, and compared with the bulk phase diagram.

$$\Delta G_m^{\phi,surface} = \frac{2.V^{\phi}.\sigma_s^{\phi}}{r} \tag{6.9}$$

is most often used in literature [116, 131, 137, 138], and its incorrectness, as explained by Kaptay in Ref. [114], is mainly due to the fact that the Kelvin equation is derived from substituting inner pressure for outer pressure. A correction factor C is commonly introduced in the equation above to take into account the effects from shape, surface strain due to non-uniformity, and uncertainty in surface tension measurements [137], and is estimated to be 1.00 for liquids and 1.05 for solids. Thus, Eqn. (6.8) becomes

$$\Delta G_m^{\phi,surface} = \frac{3.C.V^{\phi}.\sigma_s^{\phi}}{r}. \tag{6.10}$$

The molar volume V of the phase, assuming an ideal solution with no excess volume of mixing, is given by a fractional contribution of each of its pure components,

$$V^{\phi} = x_A V_A^{\phi} + x_B V_B^{\phi}. \tag{6.11}$$

The surface tension of alloy solution phases is calculated for liquids using Butler's model [139] that assumes that the surface can be modeled as a single close-packed monolayer. The monolayer layer is treated as an independent thermodynamic phase in equilibrium with the bulk phase. This model has been verified with experimental data [140–144], and according to this model, binary alloy surface tension is given by,

$$\begin{aligned} \sigma_s^{\phi} = \ & \sigma_A^{\phi} \ + \ \frac{RT}{A_A^{\phi}} log_e(\frac{x_A^{surface}}{x_A^{bulk}}) \ + \ \frac{1}{A_A^{\phi}}[G_A^{xs,surface} \ - \ G_A^{xs,bulk}] \\ = \ & \sigma_B^{\phi} \ + \ \frac{RT}{A_B^{\phi}} log_e(\frac{x_B^{surface}}{x_B^{bulk}}) \ + \ \frac{1}{A_B^{\phi}}[G_B^{xs,surface} \ - \ G_B^{xs,bulk}], \end{aligned} \tag{6.12}$$

where σ_A^{ϕ} (σ_B^{ϕ}) is the surface tension of pure component A (B) in the phase ϕ, R is the gas constant, T is the temperature, and A_A (A_B) is the molar surface area of component A (B), which is related to molar volumes through Avogadro's number N_0,

$$\begin{aligned} A_A^{\phi} = \ & 1.091 N_0^{\frac{1}{3}} (V_A^{\phi})^{\frac{2}{3}} \\ A_B^{\phi} = \ & 1.091 N_0^{\frac{1}{3}} (V_B^{\phi})^{\frac{2}{3}}, \end{aligned} \tag{6.13}$$

where $x_A^{surface}$ ($x_B^{surface}$) and x_A^{bulk} (x_B^{bulk}) are the concentrations of A (B) in the surface and bulk phases, respectively. $G_A^{xs,bulk}$ ($G_B^{xs,bulk}$) is the excess Gibbs free energy of A (B) in the bulk phase, similar to Eqn. (6.3), and $G_A^{xs,surface}$ ($G_B^{xs,surface}$) is the partial excess Gibbs free energy of A (B) in the surface and is a function of T and $x_A^{surface}$ ($x_B^{surface}$). According to Yeum's model [145],

$$\begin{aligned} G_A^{xs,surface} = \ & \beta^{mix} G_A^{xs,bulk} \\ G_B^{xs,surface} = \ & \beta^{mix} G_B^{xs,bulk}, \end{aligned} \tag{6.14}$$

where β^{mix} is a parameter corresponding to the ratio of the coordination number in the surface to that of the bulk. Tanaka *et al* [141, 146, 147] showed that β^{mix} is not surface concentration dependent for many liquid alloys, and that it can be assumed that β^{mix} is the same as β^{pure}. Due to surface relaxation and surface atomic rearrangements, β^{pure} is estimated to be 0.83 [131, 140]. For

solid metals too, β^{pure} is found to have the same value as liquid metals [131]. Thus, if differences in shape and surface strains as a function of composition are ignored, surface tensions of solid alloys can be calculated using Butler's model in a similar way as for liquid alloys [131].

Combining $G_m^{\phi,bulk}$ (from Eqns. (6.2) and (6.3)) and $\Delta G_m^{\phi,surface}$ (from Eqn. (6.10)) in Eqn. (6.5), the total Gibbs free energy of a phase $G_m^{\phi,total}$ consisting of particles of nanoscale dimensions is obtained,

$$G_m^{\phi,total} = x_A\, {}^oG_A^{bulk} + x_B\, {}^oG_B^{bulk} + RT(x_A log_e x_A + x_B log_e x_B) + x_A x_B \sum_v L_v^{\phi}(x_A - x_B)^v + \frac{3.C.V^{\phi}.\sigma_s^{\phi}}{r}. \tag{6.15}$$

Now, the total Gibbs free energy of this phase can also be defined similar to that of the bulk phase in Eqn. (6.2) above as,

$$G_m^{\phi,total} = x_A\, {}^oG_A^{nano} + x_B\, {}^oG_B^{nano} + RT(x_A log_e x_A + x_B log_e x_B) + x_A x_B \sum_v L_v^{\phi,nano}(x_A - x_B)^v, \tag{6.16}$$

where for nanoscale systems, the standard Gibbs free energy of pure components is redefined in terms of particle size r [131] using the same spherical particle approximation as discussed earlier, and is given by,

$$\begin{aligned} {}^oG_A^{nano} &= {}^oG_A^{bulk} + \frac{3.C.V_A^{\phi}.\sigma_A^{\phi}}{r} \\ {}^oG_B^{nano} &= {}^oG_B^{bulk} + \frac{3.C.V_B^{\phi}.\sigma_B^{\phi}}{r}. \end{aligned} \tag{6.17}$$

Following the work by Park *et al* [131], the non-ideal interaction parameter of a phase $L_v^{\phi,nano}$ is not only temperature dependent as for a bulk phase in Eqn. (6.4), but is now also made size-dependent by expanding it as,

$$L_v^{\phi,nano} = (A_v^{\phi} + \frac{{}'A_v^{\phi}}{r}) + (B_v^{\phi} + \frac{{}'B_v^{\phi}}{r}).T, \tag{6.18}$$

where ${}'A_v^\phi$ and ${}'B_v^\phi$ are also user-defined parameters in addition to A_v^ϕ and B_v^ϕ. Using Eqns. (6.17) and (6.18) in Eqn. (6.16), and then comparing it to Eqn. (6.15), on re-arrangement, it is finally obtained,

$$x_A x_B \sum_v ({}'A_v^\phi \ + \ {}'B_v^\phi.T)(x_A \ - \ x_B)^v \ = \ 3.C(V^\phi.\sigma_s^\phi \ - \ x_A V_A^\phi \sigma_A^\phi \ - \ x_B V_B^\phi \sigma_B^\phi). \tag{6.19}$$

This equation is used to solve for the unknown parameters ${}'A_v^\phi$ and ${}'B_v^\phi$ as described in the following subsection on the assessment methodology followed in this work.

Similar to the case of a bulk phase as described in the previous section, the parameters $L_v^{\phi,nano}$ as part of the excess Gibbs free energy of mixing also describe the temperature dependency of non-ideal configurational, vibrational, and electronic sources of entropy of the nano phase. As described in Ref. [148] (and references therein), moving from a bulk material to a nanocrystalline material can cause a larger change in vibrational entropy than configurational entropy. The source of this increase in vibrational entropy has been attributed to an enhancement of the phonon density of states at low energies (< 20 meV) which results from an increase in the number of degrees of freedom in nanocrystals that scales inversely with particle size. This could have a significant impact on the phase stability of nano-materials, although, due to the lack of inclusion of particle interactions or the effects of grain boundaries and disclocations on the phase stability of materials, nano particles in this work are, in effect, modeled as isolated particles. Thus, the above effect of phonon DOS enhancement at nanoscale particle sizes would not play a role in changing the phase stability of systems discussed in this work.

6.2.3 Assessment methodology

In this work, we have used the Thermo-Calc [29] package for the calculation of phase diagrams. To calculate a phase diagram, the first step is to determine the bulk Gibbs free energies $G_m^{\phi,bulk}$ (in Eqns. (6.1) and (6.2)) for each phase expected to participate in the bulk equilibrium phase diagram. For the binary systems studied in this work, bulk thermodynamic models have in the past been assessed and developed by various authors. This served as a starting point for the calculation of phase diagrams of nanoscale systems in this work. In cases where bulk models are not available,

parameters can be optimized and fitted to either experimental or *ab initio* data [16] using parameter optimization tools implemented in CALPHAD software (PARROT module in Thermo-Calc).

The next step involves the calculation of alloy surface tensions, which are functions of temperature and composition of the components, using Butlers model in Eqn. (6.12). This requires temperature-dependent surface tensions and molar volumes of each pure component in the phase for which alloy surface tension is being calculated, and is collected from literature and shown in Table 6.2. Then Butler's equations are solved for alloy surface tension as follows: (i) a temperature T and bulk composition x_A^{bulk} is selected, (ii) σ_A^ϕ, σ_B^ϕ, A_A^ϕ, and A_B^ϕ are inserted into Eqn. (6.12), (iii) using the condition for equilibrium: $G_A^{xs,surface} = G_B^{xs,surface}$, Eqn. (6.12) is solved by the Newton-Raphson method for σ_s^ϕ and $x_A^{surface}$ (= 1-$x_B^{surface}$) as functions of temperature and bulk compositions. This procedure is repeated at different temperatures, preferably in the range of stability of the phase, and the resulting data is inserted into Eqn. (6.19) to obtain the fitted parameters ${}'A_v^\phi$ and ${}'B_v^\phi$. In this work, surface tensions of liquid alloys in all three binary systems studied here are calculated using the above model, whereas in only the Ge-Si system, surface tension of the solid (diamond) phase is also calculated as it is the only system for which the ground state phase of both the pure element constituents Ge and Si exhibit continuous solid solubility across the entire composition space.

6.2.4 DFT calculations of surface energy

As stated in the Introduction section, no compound phases exist in the bulk equilibria of the Au-Si and Ge-Si systems (metastable phases are not considered in this work). However, the Al-Cu bulk phase diagram has numerous intermetallic phases in equilibrium [163, 164]. In this work we have followed the methodology presented by Kroupa *et al* in Ref. [165] by calculating the surface energy of one such compound Al_2Cu from *ab initio* DFT calculations [17], which is then used in the CALPHAD model. A slab model with two surfaces of the same type is created by inserting a vacuum. The surface tension σ_s^ϕ of such a model is then obtained by subtracting the cohesive energy of the bulk structure E_{coh} from the energy of the slab structure E_{slab},

$$\sigma_s^\phi \;=\; \frac{1}{2.A}(E_{slab} \;-\; N.E_{coh}), \tag{6.20}$$

Table 6.2: Thermodynamic and physical properties used in the calculation of alloy surface tensions and phase diagrams of the Au-Si, Ge-Si, and Al-Cu nanoscale systems (L: Liquid, S: Solid)

Variable	**Function**	**Reference**
Surface tension (J/m^2)	σ_{Au}^{L} = 1.33 - 1.4 x 10^{-4}T	[149]
	σ_{Au}^{S} = 1.947 - 4.3 x 10^{-4}T	[150]
	σ_{Si}^{L} = 0.732 - 8.6 x 10^{-5}(T - 1687.15)	[151]
	σ_{Si}^{S} = 1.510 - 1.589 x 10^{-4}(T - 298.2)	[152]
	σ_{Ge}^{L} = 0.621 - 2.6 x 10^{-4}(T - 1211.4)	[153]
	σ_{Ge}^{S} = 1.32 - 2.531 x 10^{-4}(T - 298.2)	[154]
	σ_{Al}^{L} = 0.871 - 1.55 x 10^{-4}(T - 933)	[155, 156]
	σ_{Al}^{S} = 1.143 - 1.946 x 10^{-4}T	[157, 158]
	σ_{Cu}^{L} = 1.615 - 2.3 x 10^{-4}T	[153]
	σ_{Cu}^{S} = 2.1585 - 4 x 10^{-4}T	[159]
Molar volume (m^3/mol)	V_{Au}^{L} = 1.02582 x 10^{-5} + 7.797 x 10^{-10}T	[153]
	V_{Au}^{S} = 1.07109 x 10^{-5}	[153]
	V_{Si}^{L} = 11.1 x 10^{-6}[1 + 1.4 x 10^{-4}(T - 1687.15)	[153]
	V_{Si}^{S} = 1.206 x 10^{-5}	[154]
	V_{Ge}^{L} = 13.2 x 10^{-6}[1 + 8 x 10^{-5}(T - 1211.4)	[153]
	V_{Ge}^{S} = 1.365 x 10^{-5}	[154]
	V_{Al}^{L} = 11.491 x 10^{-6}[1 + 9 x 10^{-5}(T - 933)	[160]
	V_{Al}^{S} = 10.797 x 10^{-6}[1 + 1.29 x 10^{-4}(T - 933)	[161]
	V_{Cu}^{L} = 7.94 x 10^{-6}[1 + 1 x 10^{-4}(T - 1356.15)	[153]
	V_{Cu}^{S} = 7.01 x 10^{-6} + 2.92 x 10^{-10}T + 1.02 x 10^{-13}T^2	[159]
	$V_{Al_2Cu}^{S}$ = 9 x 10^{-6}	[162]

where N is the number of atoms in the slab structure, and A is the area of the surface being considered. Cohesive energy is calculated using the following equation,

$$E_{coh}(Al_2Cu) \;=\; \frac{1}{3}[E_{tot}(Al_2Cu) \;-\; 2.E_{tot}^{atom}(Al) \;-\; E_{tot}^{atom}(Cu)], \tag{6.21}$$

where $E_{tot}(Al_2Cu)$ represents the total energy per formula unit of Al_2Cu, and $E_{tot}^{atom}(Al)$ and $E_{tot}^{atom}(Cu)$ are the total energies of Al and Cu, respectively. The surface tension is then used to calculate the surface energy using the spherical particle approximation in a similar way as discussed in the previous section (see Eqn. (6.10)),

$$\Delta G_m^{\phi,surface} \;=\; \frac{3.C.V^{\phi}.\sigma_s^{\phi}}{r}. \tag{6.22}$$

The surface energies of the (100), (110), and (111) planes of Al_2Cu are calculated, and the minimum is included in the model of the Al-Cu system. This method is advantageous as, in prin-

ciple, the surface energy contribution of all elements, compounds, and metastable phases can be calculated. The Al-Cu system is complex with many intermetallic phases participating in phase equilibria, so a logical extension of our current work is to perform surface energy calculations for all such structures and compare the impacts on the model predictions. It should be noted here that the larger the number of phases for which surface energies are calculated and included in the thermodynamic model, larger will be the difference in phase diagrams (melting points, reaction temperatures, etc.) between the nano and bulk systems.

The Al_2Cu compound is of tetragonal $tI12$ symmetry with space group I4/mcm (no. 140). The unit cell has the dimensions a=6.067 Å and c=4.877 Å [166]. DFT calculations were performed using the Vienna Ab-initio Simulation Package (VASP) [50–53], and ion-electron interactions were described using the Projector Augmented Wave (PAW) method [22–24]. The $3s^2 2p^1$ orbitals of Al and $3d^{10} 4s^1$ orbitals of Cu were treated as valence states to generate the PAW potentials. Non spin-polarized Local Density Approximation (LDA) [167] was used to approximate the exchange-correlation functional. The cutoff energy of plane wave basis was set to 500 eV, and integrations over the first Brillouin zone were made using a k-point grid set of 8 x 8 x 10 (and scaled appropriately for slab structures), generated according to the Γ-centered MonkhorstPack scheme [54]. Unit cell parameters and atomic positions were relaxed based on an energy convergence criteria of 10^{-4} eV/atom, and a final static calculation was performed for an accurate total energy.

6.3 Results and Discussion

6.3.1 Au-Si

There are very few experimental results that allow a direct comparison with theoretical results, and the work by Kim *et al* [132] on the Au-Si system is one of the few. In their study, spherical Au nano-particles ≈35 nm in diameter were continuously exposed to disilane (Si_2H_6) gas, and imaged with a transmission electron microscope. It was observed that with time, solid Au shrinks and the added Si forms a liquid AuSi shell on its surface, which grows until no solid Au remains. Thus, the transition from the two-phase sol-Au + liq-AuSi region of the phase diagram to the single-phase liq-AuSi is recorded. It was concluded that at 500-525^{0}C the liquidus is shifted in composition by

Δx = 3.5 at.% more Au-rich, and that the transition temperature is lowered by $\approx 240^0$C. The use of sphere-shaped particles in this study, and the fact that the above experimental data was used to make a direct correlation to a shift in the liquidus line, made the Au-Si system a perfect candidate to verify the spherical particle approximation employed in the thermodynamic models shown in the Method section.

Table 6.2 shows surface tensions and molar volumes of Au and Si, in the liquid and solid phases, as functions of temperature that are employed in this work. These functions lead to calculated melting points of Au and Si shown in Figs. 6.2 and 6.3, respectively, along with experimental data from literature which they are in fair agreement with. As expected from Eqn. (6.17), they vary inversely as a function of particle radius r. The surface tension data of liquid Si from literature shows considerable scatter as discussed in Ref. [168], and ranges anywhere between the so-called "high" and "low" values of $\sigma = 0.86$ J/m^{-2} and $\sigma = 0.74$ J/m^{-2}, respectively. The resulting value is debated to depend on the measurement method (sessile drop, large drop, levitation techniques, oscillating drop method), the crucible/substrate material, and oxygen contamination [169]. In this work we have chosen the "low" value from Ref. [151], i.e., $\sigma^L_{Si} = 0.732$ - 8.6 x 10^{-5}(T - 1687.15), because when combined with surface tension of solid Si: $\sigma^S_{Si} = 1.510$ - 1.589 x 10^{-4}(T - 298.2) [152], the resulting melting points of Si lie within the upper and lower limits defined by Couchman *et al* [170]. Results from the study on isolated Si particles of sizes ≤ 6 nm by Goldstein Ref. [171] show a much more significant drop in melting points. Due to the previously mentioned size limitations in the CALPHAD model, the applicability of the spherical particle approximation in this current method is limited to radius exceeding 5 nm. Curve (a) in Fig. 6.3 is calculated using surface tension data of liquid and solid Si from Refs. [153] and [158], respectively, and is in worse agreement with literature data. Discrepancies in melting temperatures can be attributed to several reasons: due to the fact that experimental melting temperatures are not defined by the equality of Gibbs energy of the solid and liquid phases; nanoparticles are prone to defects and impurities especially due to their relatively large surface areas; although phase-field theory has its own limitations, it has been demonstrated using phase-field approach [172, 173] that surface melting can begin at lower temperatures than complete melting and that complete melting occurs when the interface between the surface melt and solid core loses its stability as the surface melt propagates towards the center, which is determined by local equilibrium conditions at the interface; due to kinetics and thermal

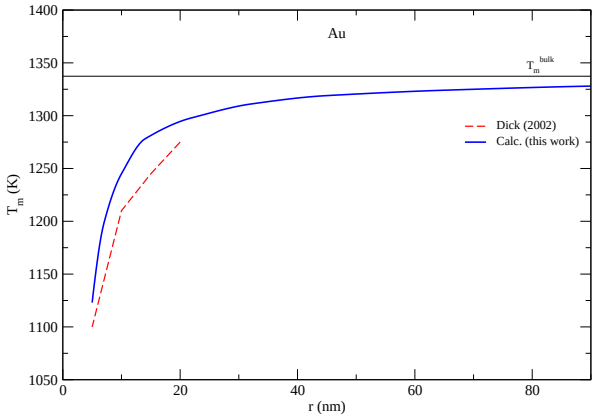

Figure 6.2: (Color online) Calculated melting points of Au as a function of particle size compared with experimental data from Ref. [179].

fluctuations, melting may start when the kinetic nucleation criterion is satisfied.

Following the methodology explained in the Method section, we first start with bulk thermodynamic data of Au-Si which is obtained from the work by Meng *et al* [174]. His model was optimized with measured data on mixing enthalpies of the liquid phase and activities of Au and Si. Then, using the surface tension and volumetric data of Au and Si, Butler's equations are solved to calculate alloy surface tension of the liquid phase of Au-Si as a function of temperature and composition. Parameters ${}^{'}A_v^{\phi}$ and ${}^{'}B_v^{\phi}$ are then fitted to this data using Eqn. (6.19). Increasing the order parameters v was found to have no significant effect on the phase diagrams, and thus its maximum value was kept the same between nano and bulk systems. Resulting non-ideal interaction parameters, combined with bulk parameters, are shown in Table 6.3 along with the modified standard Gibbs energies of pure components. This completes the thermodynamic model for nano-sized particles, and the resulting phase diagrams can be calculated for different particle sizes by changing r.

Fig. 6.4a shows the calculated Au-Si phase diagram at $r = 7$ nm. Fig. 6.4b shows the same phase diagram, but now plotted to compare with the experimental data from Ref. [132]. The amount of shift of the liquidus solubility line and the drop in transition temperature agree very well with the predicted amounts in Ref. [132]. As discussed earlier, the use of spherical particles in Ref. [132] serves as a direct validation of the spherical particle model used in this study to calculate

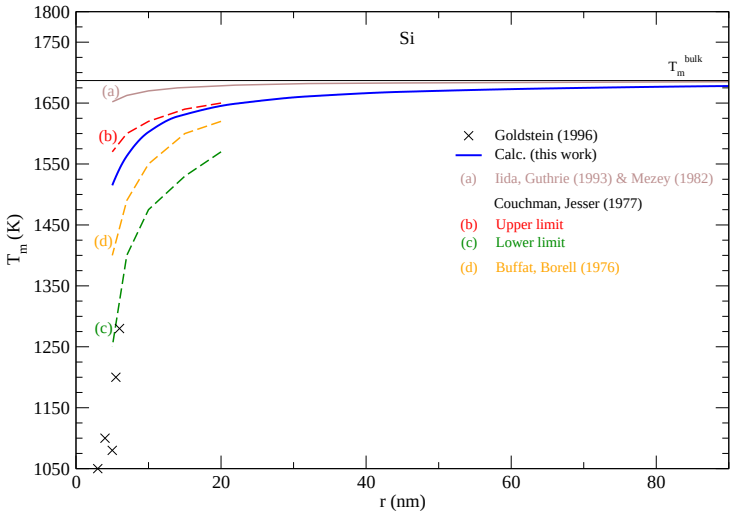

Figure 6.3: (Color online) Calculated melting points of Si, using surface tension data from Mallot *et al* [151] for liquid and from Jaccodine *et al* [152] for the solid phase, as a function of particle size compared with experimental data from Iida & Guthrie [153], Mezey *et al* [158], Couchman & Jesser [170], Buffat & Borell [180], and Goldstein [171].

surface energies. Table 6.4 shows the drop in eutectic temperatures and its compositional shifts in the Au-Si system as a function of particle size.

6.3.2 Ge-Si

Semiconductors based on GeSi are used in electronic devices for a wide variety of applications, making it of great industrial and technological importance. The above validated model is applied to the Ge-Si system following the same methodology, but this time alloy surface tension of the solid diamond phase is also calculated in addition to that of the liquid phase. This is possible because the solid diamond phase in the Ge-Si system exhibits continuous solid solubility between its pure components Ge and Si up to very high temperatures in the order of 1200 K, as shown in Fig. 6.5a. This phase also exhibits a low-temperature symmetrical miscibility gap with its highest point at $\approx$ 226.5 K. The bulk thermodynamic data of the liquid and diamond phases is extracted from Refs. [175] and [176], respectively. Fig. 6.6 shows the calculated surface tensions of the liquid phase at various compositions and temperatures, and agrees very well with experimental data on Si and

(a)

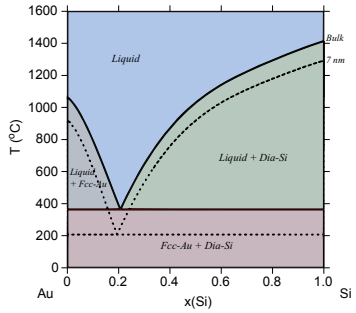

(b)

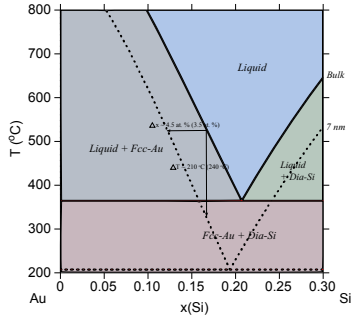

Figure 6.4: (Color online) Au-Si phase diagram. (a) Phase diagram of the Au-Si alloy system calculated for particles of radius, r = 7 nm, and compared with the bulk phase diagram from Ref. [174]. (b) Part of Au-Si phase diagram showing the amounts of shift in solubility lines which agrees well with experimental results from Ref. [132] shown in parentheses.

Ge melts from Ref. [177]. Complete thermodynamic functions of the model are listed in Table 6.3. The functions for Ge lead to melting points shown in Fig. 6.7 compared with experimental data on Ge nanocrystals. The calculated phase diagram at particle radius $r =$ 22 nm is shown in Fig. 6.5b, and as expected, equilibrium lines are lowered in temperature from their positions in the bulk phase diagram. At the suggested lowest particle size of $r = 5$ nm for the nano-CALPHAD method, the peak temperature of the solid phase miscibility gap is reduced to 68.1 K as shown in Fig. 6.5b. Table 6.4 lists the calculated peak temperatures of the miscibility gap. The depression of the miscibility gap at small particle sizes due to larger contributions of surface energy terms could have significant implications for engineering alloy design and fabrication which rely on phase

diagram to tune thermodynamic, electrical, and transport properties.

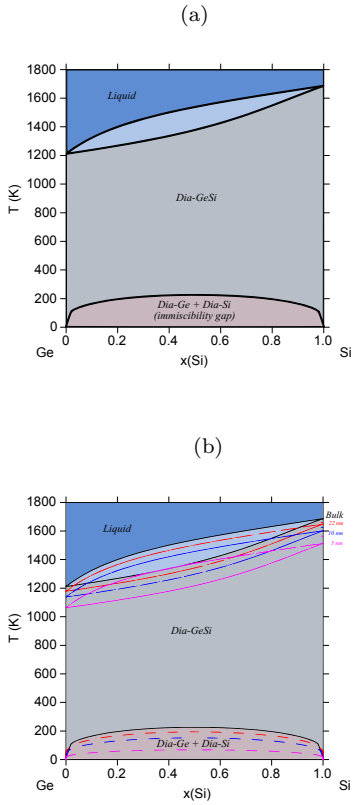

Figure 6.5: (Color online) Ge-Si phase diagram. (a) Bulk Ge-Si phase diagram calculated using data from Refs. [26, 175, 176]. (b) Phase diagram of the Ge-Si alloy system calculated for varying radii particles, and compared with the bulk phase diagram. With decreasing particle radii, the peak temperature of the miscibility gap decreases from $\approx$ 226 K for bulk particles to $\approx$ 68 K for particles of radii, r = 5 nm.

6.3.3 Al-Cu

The Al-Cu system is different from the Au-Si and Ge-Si systems in that there are a number of intermetallic compounds, totaling to 13, both stoichiometric and non-stoichiometric, that participate in the equilibrium phase diagram [163, 164], as shown in Fig. 6.8a. In principle, the thermodynamic model of Al-Cu must include surface energies of all these compounds in addition to those of the

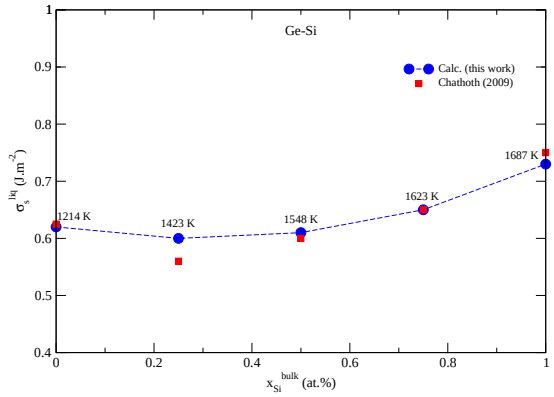

Figure 6.6: (Color online) Calculated surface tension of the liquid phase in the Ge-Si system compared with experimental data from Ref. [177]. Dashed line only serves as a guide to the eye.

liquid and room-temperature solid phases. Since such data is largely unavailable for most systems from literature, one can resort to DFT to calculate the surface tension of each phase. However, calculating the surface tension of different planes in each of the 13 compounds is computationally expensive. For the purpose of demonstration, in this work we have calculated the surface energy of only one such compound Al_2Cu from DFT, and included that in the thermodynamic model to calculate the phase diagram of Al-Cu.

Details of the calculation methods used, and structural information about the Al_2Cu compound are mentioned earlier in Section 6.2.4. Its unit cell is shown in Fig. 6.9. The calculated structural and cohesive energies of the compound, along with those of Al and Cu, are compared with experimental data in Table 6.5. These results are in accordance with the observation of underestimation of lattice constants and over-estimation of cohesive energies by the LDA approximation to the exchange-correlation functional [178]. Slab models were created for the (100), (110), and (111) surfaces as shown in Fig. 6.10. Both the height of the vacuum, and number of atomic layers were varied in each model so as to obtain converged surface tension values. Table 6.6 shows the resulting surface tensions of each surface as a function of vacuum height and number of atomic layers calculated using Eqn. (6.20). Since the surface tension of the (111) plane is the lowest, its surface energy calculated using Eqn. (6.22) is inserted into the thermodynamic model. Thermodynamic functions for this phase, along with non-ideal interaction parameters computed for the

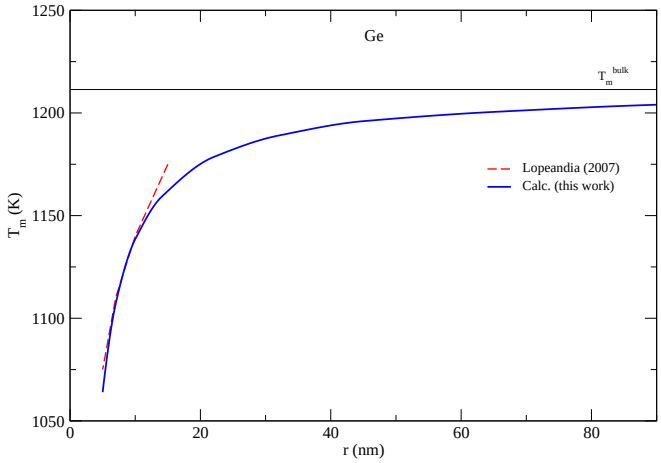

Figure 6.7: (Color online) Calculated melting points of Ge as a function of particle size compared with experimental data from Ref. [181].

liquid phase, and standard Gibbs energies of Al and Cu are listed in Table 6.3. Melting points of Al and Cu calculated using these functions as a function of particle size agree with experimental data on synthesized nano-particles as shown in Figs. 6.11 and 6.12, respectively, and so does the liquid phase surface tensions calculated using Butler's equations at T = 1375 K as shown in Fig. 6.13. The good agreement of the model predictions and experimental data suggest that even for complex systems with many intermetallics such as Al-Cu, rigorous calculations of surface and phase data for a single or a limited number of critical compositions may be sufficient to eliminate the need for wide-ranging calculations for all intermetallics. The Al-Cu phase diagram calculated at $r = 10$ nm is shown in Fig. 6.8b. Only Al-rich compositions are shown in this figure as the surface tension of only one of several intermetallic compounds, Al_2Cu, is calculated in this work. Table 6.4 shows the drop in temperature and shift in composition of the eutectic reaction: Liq $\rightarrow$ fcc-Al + Al_2Cu as particle sizes are decreased.

6.4 Conclusions and outlook

In this work, by calculating phase diagrams at varying particle radii, we have shown the considerable changes in equilibrium thermodynamics resulting from decreasing particle sizes to nanoscale dimensions. At these particle sizes, the surface to volume ratio is drastically increased, and so is

(a)

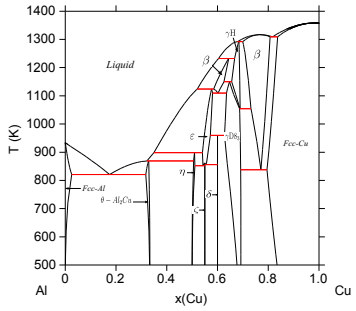

(b)

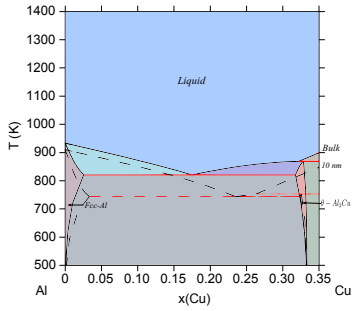

Figure 6.8: (Color online) Al-Cu phase diagram. (a) Bulk Al-Cu phase diagram according to Refs. [163, 164]. (b) Phase diagram of the Al-Cu alloy system calculated for particles of radius r = 10 nm, compared with the bulk phase diagram at Al-rich/Cu-poor compositions. The eutectic temperature drops from ≈ 821 K for bulk particles to ≈ 695 K for particles of radii, r = 5 nm.

the contribution of surface energy to the Gibbs free energies of the phases. This dominant surface energy term is calculated using the spherical particle approximation that assumes particles to be spherical in shape. In a similar way, this methodology can be extended to non-spherical particles using a non-ideality factor in the Gibbs surface energy term.

The Au-Si system was first chosen as it is one of the few systems for which experimental data that estimates shift in equilibrium lines for spherical nano-particles was available. This allowed for a direct verification of the surface energy models that assume sphere-shaped particles, and the resulting phase diagram was in good agreement. Phase diagrams of Ge-Si particles were computed

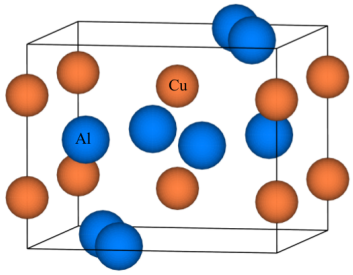

Figure 6.9: (Color online) Unit cell of the Al_2Cu compound.

in a similar way, and a considerable depression of the miscibility gap was noted. This is vital when, for example, alloys are designed to achieve compositions that do not lie in the miscibility gap to achieve a desired band gap value. Finally, DFT was used to compute the surface energy of one of the many intermetallic compounds in the Al-Cu system. This was then added to its thermodynamic model, and a drop in the eutectic temperature in its phase diagram was tabulated.

To conclude, due to surfaces (and interfaces) materials can have considerably different thermodynamic and phase stability behavior from bulk systems, and as transistor and devices continue to be scaled down in sizes, the study of their phase stability becomes necessary. This is critical not only for designing semiconductor alloys and compounds, but also for tuning their electrical, thermodynamic, and transport properties in order to achieve optimum device performance.

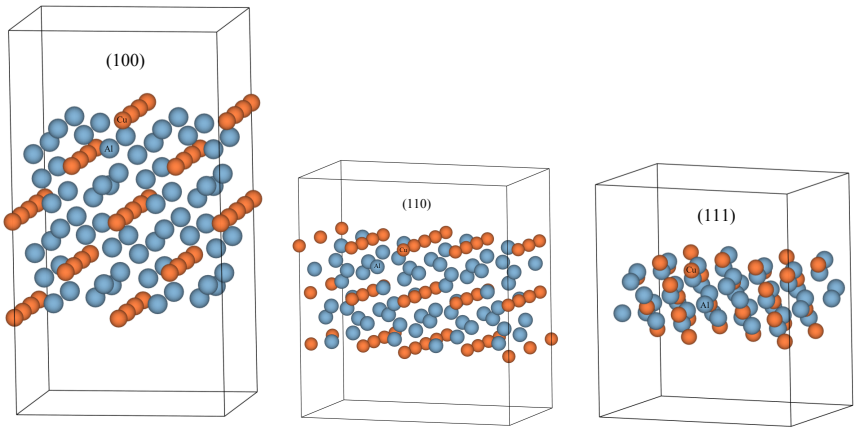

Figure 6.10: (Color online) Slab models created for the calculation of surface energies of the (100), (110), and (111) planes in the Al_2Cu compound. These surface energies can then be used to calculate the surface energy contribution to the total Gibbs free energy of this phase, which will lead to the estimation of the change in phase stability of this compound in the phase diagram as a function of particle radii. Since the surface energy can theoretically be calculated for any compound using DFT, this method can be applied to all the phases in a system including equilibrium, metastable, and unstable phases.

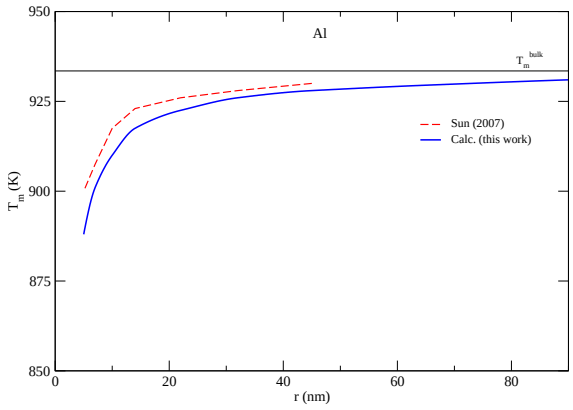

Figure 6.11: (Color online) Calculated melting points of Al as a function of particle size compared with experimental data from Ref. [185].

Table 6.3: Thermodynamic functions used in the calculation of phase diagrams in this work (in J mol^{-1} and K). All bulk and size-independent functions are obtained from (a) Au-Si: SGTE database [26] and Ref. [174], (b) Ge-Si: SGTE database [26] and Refs. [175] and [176] for the liquid and diamond phases, respectively, and (c) Al-Cu: Ref. [164] for the liquid and $\gamma D8_3$ phases, and the COST-507 database [163] for the rest of the phases.

Standard element reference Gibbs energies

$${}^{o}G_{Au}^{fcc,nano} = {}^{o}G_{Au}^{fcc,bulk} + \frac{6.569\times10^{-5}}{r} - \frac{1.4508\times10^{-8}}{r}.\mathrm{T}$$

$${}^{o}G_{Si}^{dia,nano} = {}^{o}G_{Si}^{dia,bulk} + \frac{5.916\times10^{-5}}{r} - \frac{6.0365\times10^{-9}}{r}.\mathrm{T}$$

$${}^{o}G_{Ge}^{dia,nano} = {}^{o}G_{Ge}^{dia,bulk} + \frac{6.000\times10^{-5}}{r} - \frac{1.0883\times10^{-8}}{r}.\mathrm{T}$$

$${}^{o}G_{Al}^{fcc,nano} = {}^{o}G_{Al}^{fcc,bulk} + \frac{3.419\times10^{-5}}{r} - \frac{8.07\times10^{-10}}{r}.\mathrm{T} - \frac{8.539\times10^{-13}}{r}.\mathrm{T}^2$$

$${}^{o}G_{Cu}^{fcc,nano} = {}^{o}G_{Cu}^{fcc,bulk} + \frac{4.767\times10^{-5}}{r} - \frac{6.847\times10^{-9}}{r}.\mathrm{T} + \frac{3.257\times10^{-13}}{r}.\mathrm{T}^2$$

Liquid phases

$$G_{Au}^{liq,nano} = G_{Au}^{liq,bulk} + \frac{4.093\times10^{-5}}{r} - \frac{1.197\times10^{-9}}{r}.\mathrm{T} - \frac{3.2747\times10^{-13}}{r}.\mathrm{T}^2$$

$$G_{Si}^{liq,nano} = G_{Si}^{liq,bulk} + \frac{2.231\times10^{-5}}{r} + \frac{1.9013\times10^{-9}}{r}.\mathrm{T} - \frac{4.009\times10^{-13}}{r}.\mathrm{T}^2$$

$$G_{Ge}^{liq,nano} = G_{Ge}^{liq,bulk} + \frac{3.347\times10^{-5}}{r} - \frac{6.3326\times10^{-9}}{r}.\mathrm{T} - \frac{8.2368\times10^{-13}}{r}.\mathrm{T}^2$$

$$G_{Al}^{liq,nano} = G_{Al}^{liq,bulk} + \frac{3.207\times10^{-5}}{r} - \frac{1.745\times10^{-9}}{r}.\mathrm{T} - \frac{4.809\times10^{-13}}{r}.\mathrm{T}^2$$

$$G_{Cu}^{liq,nano} = G_{Cu}^{liq,bulk} + \frac{3.325\times10^{-5}}{r} - \frac{8.880\times10^{-10}}{r}.\mathrm{T} - \frac{5.478\times10^{-13}}{r}.\mathrm{T}^2$$

Intermetallic compounds

$$G_{Al:Cu}^{Al_2Cu,nano} = 2 * {}^{o}G_{Al}^{fcc,nano} + {}^{o}G_{Cu}^{fcc,nano} + (-47406 + \frac{3.479\times10^{-5}}{r}) + (6.75).\mathrm{T}$$

Interaction parameters

1. Au-Si

$$L_0^{liq,nano} = (-24103.3028 - \frac{1.5445\times10^{-5}}{r}) + (-15.13883 + \frac{7.4895\times10^{-9}}{r}).\mathrm{T}$$

$$L_1^{liq,nano} = (-29375.2777 + \frac{5.200\times10^{-6}}{r}) + (1.1065 + \frac{1.0399\times10^{-9}}{r}).\mathrm{T}$$

$$L_2^{liq,nano} = (-13032.2412 + \frac{1.5498\times10^{-5}}{r}) - (\frac{4.469\times10^{-9}}{r}).\mathrm{T}$$

2. Ge-Si

$$L_0^{liq,nano} = (+6610 + \frac{2.362\times10^{-6}}{r}) + (-0.354 - \frac{3.596\times10^{-9}}{r}).\mathrm{T}$$

$$L_0^{dia,nano} = (+3765.6 - \frac{1.3823\times10^{-5}}{r}) + (\frac{9.6134\times10^{-9}}{r}).\mathrm{T}$$

3. Al-Cu

$$L_0^{liq,nano} = (-67094 - \frac{9.379\times10^{-6}}{r}) + (8.555 + \frac{4.642\times10^{-9}}{r}).\mathrm{T}$$

$$L_1^{liq,nano} = (32148 - \frac{1.785\times10^{-6}}{r}) + (-7.118 - \frac{5.667\times10^{-10}}{r}).\mathrm{T}$$

$$L_2^{liq,nano} = (5915 + \frac{6.445\times10^{-6}}{r}) + (-5.889 - \frac{1.89\times10^{-9}}{r}).\mathrm{T}$$

$$L_3^{liq,nano} = -8175 + 6.049.\mathrm{T}$$

Table 6.4: Change in points on the phase diagram for particles from bulk to nanoscale dimensions. Au-Si: temperature and composition of the eutectic point - Liq → fcc-Au + dia-Si, Ge-Si: peak temperature of the miscibility gap in the diamond phase, and Al-Cu: temperature and composition of the eutectic point - Liq → fcc-Al + Al_2Cu.

	Au-Si: Liq→fcc-Au+dia-Si		**Ge-Si: Peak miscibility gap**	**Al-Cu: Liq→fcc-Al+Al_2Cu**	
Radius (nm)	x(Si) (at.%)	T (^{o}C)	T (K)	x(Cu) (at.%)	T (K)
Bulk	20.6	364.2	226.5	17.5	821
90	20.6	353.1	218.6	18.2	812.5
65	20.6	348.8	215.6	18.4	810
45	20.5	341.8	210.5	18.7	805
32	20.5	332.6	204.2	19.3	799
22	20.3	317.7	193.7	20.2	787.5
14	20.1	289.9	174.3	21.8	767.5
10	19.8	257.9	152.1	23.5	744
7	19.4	207.4	117.5	25.1	717
5	18.6	134.2	68.1	25.8	695

Table 6.5: Calculated lattice constants (in Å) and cohesive energy, E_{coh} (in eV/atom) of Al, Cu, and the Al_2Cu phase from DFT using the LDA approximation. Experimental data are shown in parentheses.

Phase	**Space group**	**Pearson symbol**	**Lattice constants**	**E_{coh} (eV/atom)**
Al	$Fm\bar{3}m$ (no. 225)	cF4	a = 3.9793 (4.047[a])	4.133 (3.39[c])
Cu	$Fm\bar{3}m$ (no. 225)	cF4	a = 3.5246 (3.6536[b])	4.703 (3.49[c])
Al_2Cu	I4/mcm (no. 140)	tI12	a = 5.943 (6.063[d]) c = 4.781 (4.872[d])	-4.506

a: Ref. [182]
b: Ref. [183]
c: Ref. [184]
d: Ref. [166]

Table 6.6: Converged surface tension values of different planes in the Al_2Cu intermetallic compound calculated from DFT using the LDA approximation.

Plane	**Surface tension, $\sigma_s^{Al_2Cu}$**	
	meV/Å^2	J/m^2
(100)	0.079	1.275
(110)	0.099	1.586
(111)	0.077	1.227

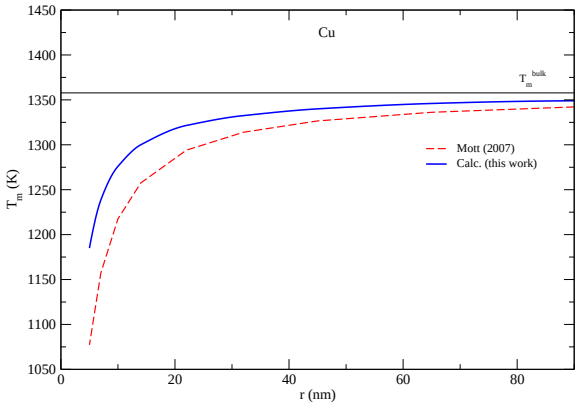

Figure 6.12: (Color online) Calculated melting points of Cu as a function of particle size compared with experimental data from Ref. [186].

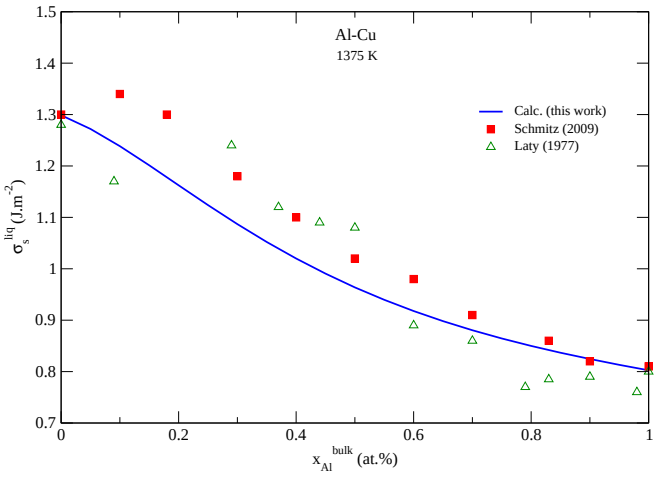

Figure 6.13: (Color online) Calculated surface tension of the liquid phase in the Al-Cu system compared with experimental data from Refs. [156, 187].

Chapter 7

Conclusions and summary

In the majority of the work in this thesis, the theories of computational thermodynamics and phase stability have been applied to the field of thermoelectric materials research. The electrical properties exhibited by a particular thermoelectric alloy stems from the defects present in the system. DFT has frequently been used to understand the defect physics of a semiconducting material, and in Chapter 3, we use it to study the thermodynamics of intrinsic point defects in a popular and one of the most efficient thermoelectric material, PbTe. Using the principle of charge balance, equilibrium Fermi levels in the system are calculated as a function of temperature, that helps attribute the origins of n-type and p-type conductivity in PbTe to V_{Te}^{+2} defects in Pb-rich and V_{Pb}^{-2} defects in Te-rich growth conditions, respectively. The resulting equilibrium carrier concentrations as functions of temperature agree fairly well with experimental measurements. In order to couple these DFT results with the CALPHAD method, the calculated defect formation energies of the vacancy defects above at the equilibrium Fermi level are used as input to optimize the thermodynamic model of the Pb-Te phase diagram system. The resulting phase solubility of the PbTe phase agrees well with experimental results and DFT calculations. This work paves a way to couple the DFT and CALPHAD methods (details of which are discussed in Chapter 2), which is essential to predicting phase solubilities of thermoelectric materials in cases when no experimental data is available. Knowing such solubility limits is critical to the field of thermoelectrics since it gives information on the extent of obtainable carrier concentrations and other thermoelectric properties.

Doping a thermoelectric, or a semiconducting material in general, with impurity atoms is a common strategy to unlock its potential for higher performance efficiencies. It allows for precise control

over carrier concentrations and other electronic properties that are important for thermoelectric materials. In Chapters 4 and 5, changes in phase stability upon doping another lead chalcogenide PbSe is explored. Specifically in Chapter 4, two dopants, Na and Br, are picked for doping on the cation and anion sites of PbSe, respectively. Defect formation energy calculations on intrinsic and extrinsic point defects in these systems show unusually low formation energies for neutral defects. Further investigating the charge density of supercells containing these defects, it is found that there is significant delocalization of charge indicating that their energies are not representative of their true neutral states, but actually of charged defects in polaronic states. Without any physical correction method available to treat such defects, experimental results on doping efficiencies are used to correct their energies, thus providing a way to calculate phase boundaries of the PbSe phase upon the addition of dopants.

In Chapter 5, phase diagrams of the PbSe phase upon the addition of Cl, I, Sb, Bi, and In as dopants are calculated. This is important to know the range of efficiencies and thermoelectric properties as functions of composition and temperature that can be achieved without precipitating secondary phases. Depending on the phase diagram, there is usually more than one method of doping. The calculated phase boundaries and solubilities help illustrate which doping method would be the most effective in doping a material without precipitating secondary phases. Results on defect formation energies at solubility points of different regions of phase diagram also help predict electrical properties that would be exhibited by samples prepared using these doping methods, demonstrating the importance of such a study in the field of thermoelectric materials research.

With reduction in material grain sizes for nano-engineering of materials becoming more popular, knowing whether a material exhibits the same phase stability at nano grain sizes as for bulk sizes becomes important. In Chapter 6, the effect of reduction in grain sizes on phase diagrams is explored in three binary alloys popular in the electronic industry: Au-Si, Ge-Si, and Al-Cu. At nanoscale, the significant difference in material structure from bulk sizes originates from enhanced surface areas. Energy contributions from surfaces is modeled assuming spherical particles, and then added to bulk Gibbs free energy models from the CALPHAD method to obtain phase diagrams as functions of grain sizes. For intermetallic phases, surface energies are calculated using DFT on slab structures as illustrated for the Al_2Cu phase in the Al-Cu system. Using this procedure, it is found

that changes from bulk diagrams upon reduction in particle sizes can be significant, thus making such determination of nano phase diagrams critical.

Bibliography

[1] M.B. Dyurgerov, M.F. Meier, Proc. Natl. Acad. Sci. 97 (2000) 1406-1411.

[2] S.L. van der Linden , A.A. Leiserowitz, G.D. Feinberg, E.W. Maibach, PLoS ONE 10 (2014) 1-8.

[3] N. Oreskes, Science 306 (2004) 1686.

[4] P.T. Doran, M.K. Zimmerman, EOS 90 (2009) 22-23.

[5] E. Maibach, T. Myers, A. Leiserowitz, Earth's Future 2 (2014) 295-298.

[6] D.B. Gingerich, M.S. Mauter, Environ. Sci. Technol., 49 (14) (2015), 82978306.

[7] J.R. Salvador, J.Y. Cho, Z. Ye, J.E. Moczygemba, A.J. Thompson, J.W. Sharp, J.D. Knig, R. Maloney, T. Thompson, J. Sakamoto, H. Wang, A.A. Wereszczak, G.P. Meisner, J. Elec. Mat. 42(7) (2013) 1389-1399.

[8] J. Liebl, S. Neugebauer, A. Eder, M. Linde, B. Mazar, W. Sttz, MTZ Worldwide 70(4) (2009) 4-11.

[9] Y.P. Prilepo, A.A. Pustovalov, V.V. Sinyavskiy, N.M. Sudak, O.B. Yatsenko, Thermal Engineering 59(13) (2012) 981-983.

[10] S. Thomas, D. Leonard, H. John, Z. June, in 9th Annual International Energy Conversion Engineering Conference (2011) American Institute of Aeronautics and Astronautics.

[11] J.E.P. Connerney, N.F. Ness, M.H. Acunúa, Nature 298 (1982) 44-46.

[12] S.K. Yee, S. LeBlanc, K.E. Goodson, C. Dames, Energy Environ. Sci. 6(9) (2013) 2561-2571.

[13] G.J. Snyder, E.S. Toberer, Nature Mater. 7 (2008) 105-114.

[14] P. Hohenberg and W. Kohn, Phys. Rev. 136 (1964) B864-B871.

[15] W. Kohn and L. J. Sham, Phys. Rev. 140 (1965) A1133-A1138.

[16] N. Saunders, A.P. Miodownik, Pergamon Mater. Ser. (1998).

[17] R.M. Martin, Electronic Structure, in:Cambridge University Press, Cambridge, England, 2004.

[18] J.P. Perdew, K. Burke, M. Ernzerhof, Phys. Rev. Lett. 77 (1996) 3865-3868.

[19] D.R. Hamann, M. Schlüter, C. Chiang, Phys. Rev. Lett. 43 (1979) 1494-1497.

[20] P.E. Blöchl, Phys. Rev. B 41 (1990) 5414-5416.

[21] D. Vanderbilt, Phys. Rev. B 41 (1990) 7892-7895.

[22] P.E. Blöchl, Phys. Rev. B 50 (1994) 17953-17979.

[23] G. Kresse, D. Joubert, Phys. Rev. B 59 (1999) 1758-1775.

[24] O. Bengone, M. Alouani, P. Blöchl, J. Hugel, Phys. Rev. B 62 (2000) 16392-16401.

[25] N.A.W. Holzwarth, G.E. Matthews, R.B. Dunning, A.R. Tackett, Y. Zeng, Phys. Rev. B 55 (1997) 2005-2017.

[26] A.T. Dinsdale, CALPHAD 15 (1991) 317-425.

[27] O. Redlich, A.T. Kister, Ind. Eng. Chem. 40 (1948) 345-348.

[28] B. Jansson, *TRITA-MAC-0234*, Division of Physical Metallurgy, Royal Institute of Technology, Stockholm, Sweden, 1984.

[29] J-O Andersson, T. Helander, L. Höglund, P. Shi, B. Sundman, CALPHAD 26 (2002) 273-312.

[30] S. Bajaj, G.S. Pomrehn, J.W. Doak, W. Gierlotka, H. Wu, S.W. Chen, C. Wolverton, W.A. Goddard, G.J. Snyder, Acta Mater. 92 (2015) 72-80.

[31] R.F. Brebrick, R.S. Allgaier, J. Chem. Phys. 32 (1960) 18261831.

[32] R.F. Brebrick, E. Grubner, J. Chem. Phys. 36 (1962) 12831289.

[33] C.R. Hewes, M.S. Adler, S.D. Senturia, J. Appl. Phys. 44 (1973) 13271332.

[34] B.J. Sealy, A.J. Krocker, J. Mater. Sci. 8 (1973) 17371743.

[35] H. Maier, J. Hesse, Org. Cryst. Germanates Semicond. 4 (1980) 145-219.

[36] W.W. Scanlon, Phys. Rev. 126 (1962) 509513.

[37] N. Chou, K. Komarek, E. Miller, Trans. AIME 245 (1969) 15531560.

[38] S. Ahmad, S.D. Mahanti, K. Hoang, M.G. Kanatzidis, Phys. Rev. B 74 (2006) 155205-1-13.

[39] K. Xiong, G. Lee, R.P. Gupta, W. Wang, B.E. Gnade, K. Cho, J. Phys. D: Appl. Phys. 43 (2010) 405403-1-8.

[40] N. Wang, D. West, J. Liu, J. Li, Q. Yan, B.-L. Gu, S. B. Zhang, W. Duan, Phys. Rev. B 89 (2014) 045142-1-6.

[41] W. Gierlotka, J. Lapsa, D. Jendrzejczyk-Handzlik, J. Alloys Compd. 479 (2009) 152-156.

[42] C. Wagner, W. Schottky, Z. Phys. Chem. 11 (1930) 163-171.

[43] S.B. Zhang, J.E. Northrup, Phys. Rev. Lett. 67 (1991) 2339-2342.

[44] S. Lany, A. Zunger, Model. Simul. Mater. Sci. 17 (2009) 084002-1-14.

[45] G. Makov, M. Payne, Phys. Rev. B 51 (1995) 4014-4022.

[46] M. Gajdoš, K. Hummer, G. Kresse, J. Furthmüller, F. Bechstedt, Phys. Rev. B 73 (2006) 045112-1-9.

[47] S. Baroni, R. Resta, Phys. Rev. B 33 (1986) 7017-7021.

[48] X. Wu, D. Vanderbilt, D.R. Hamann, Phys. Rev. B 72 (2005) 035105-1-13.

[49] W. Cochran, R. A. Cowley, G. Dolling, M. M. Elcombe, Proc. R. Soc. London A 293 (1966) 433-451.

[50] G. Kresse, J. Hafner, Phys. Rev. B 47 (1993) 558-561.

[51] G. Kresse, J. Hafner, Phys. Rev. B 49 (1994) 14251-14269.

[52] G. Kresse, J. Furthmüller, Comput. Mater. Sci. 6 (1996) 15-50.

[53] G. Kresse, J. Furthmüller, Phys. Rev. B 54 (1996) 11169-11186.

[54] H.J. Monkhorst, J.D. Pack, Phys. Rev. B 13 (1976) 5188-5192.

[55] W. Gierlotka, J. Lapsa, K. Fitzner, J. Phase Equilib. Diffus. 31 (2010) 509-517.

[56] U. Kattner, H.L. Lukas, G. Petzow, CALPHAD 10 (1986) 103116.

[57] J.C. Valiant, T.E. Faber, Philos. Mag. 29 (1974) 571-583.

[58] V.M. Glazov, S.N. Tshizevskaya, N.N. Glozdeva, Liquid Semiconductors, Nauka, Moscow, 1967.

[59] F. Sommer, Z. Metallkd. 73 (1982) 72-86.

[60] K. Koike, T. Honden, I. Makabe, F.P. Yan, M. Yano, J. Cryst. Growth 257 (2003) 212-217.

[61] C. Hirayama, J. Chem. Eng. Data 9 (1964) 6568.

[62] P.M. Robinson, M.B. Bever, Trans. AIME 236 (1966) 814817.

[63] Z.M. Gibbs, H. Kim, H. Wang, R.L. White, F. Drymiotis, M. Kaviany, G.J. Snyder, Appl. Phys. Lett. 103 (2013) 262109-1-5.

[64] C. Freysoldt, B. Grabowski, T. Hickel, J. Neugebauer, G. Kresse, A. Janotti, C. Walle, Rev. Mod. Phys. 86 (2014) 253-305.

[65] S. Lany, A. Zunger, Phys. Rev. B 78 (2008) 235104-1-25.

[66] S.M. Sze, Physics of Semiconductor Devices, 2nd ed., John Wiley & Sons, New York, 1981.

[67] M. Schenk, H. Berger, A. Klimakow, M. Mühlberg, M. Wienecke, Cryst. Res. Technol. 23 (1988) 77-84.

[68] H. Gravemann, H.-J.Wallbaum, Z. Metallkde 47 (1956) 433441.

[69] M. Moniri, C. Petot, J. Calorim. Anal. Therm. 24b (1978) 195201.

[70] Y.L. Kharif, P.V. Kovtunenko, A.A. Maier, I.K. Avetisov, Russ. J. Phys. Chem. 56 (1982) 1331-1334.

[71] H. Fay, C.B. Gillson, J. Am. Chem. 27 (1902) 8195.

[72] M. Kimura, Mem. Coll. Eng. Kyoto 1 (1915) 149152.

[73] S. Bajaj, A. Landa, P. Söderlind, P. Turchi, R. Arróyave, J. Nucl. Mater. 419 (2011) 177185.

[74] R. Castanet, Y. Claire, M. Laffite, High Temp. High Press. 4 (1972) 343351.

[75] T. Maekawa, T. Yokokawa, K. Niwa, Bussei Kenkyu 17 (1972) 282286.

[76] R. Blachnik, B. Gather, J. Less Common Met. 92 (1983) 207213.

[77] R.F. Brebrick, A.J. Strauss, J. Chem. Phys. 40 (1964) 32303241.

[78] B. Predel, J. Piehl, M.J. Pool, Z. Metallkde 66 (1975) 347352.

[79] K. Ellmer, Nat. Phot. 6 (2012) 809-817.

[80] J. Vidal, S. Lany, M. dAvezac, A. Zunger, A. Zakutayev, J. Francis, J. Tate, App. Phys. Lett. 100 (2012) 032104-1-4.

[81] Y.Z. Pei, X.Y. Shi, A.D. LaLonde, H. Wang, L.D. Chen, G.J. Snyder, Nature 473 (2011) 66-69.

[82] H. Wang, Y.Z. Pei, A.D. LaLonde, G.J. Snyder, Adv. Mater. 23 (2011) 1366-1370.

[83] L.-D. Zhao, S.-H. Lo, J. He, H. Li, K. Biswas, J. Androulakis, C.-I. Wu, T.P. Hogan, D.-Y. Chung, V.P. Dravid, M.G. Kanatzidis, J. Am. Chem. Soc. 133 (2011) 20476-20487.

[84] H. Wang, Y.Z. Pei, A.D. LaLonde, G.J. Snyder, Proc. Natl. Acad. Sci. 109 (2012) 9705-9709.

[85] G.T. Alekseeva, E.A. Gurieva, P.P. Konstantinov, L.V. Prokofeva, M.I. Fedorov, Semic. 30 (1996) 1125-1127.

[86] D. Parker, D.J. Singh, Phys. Rev. B 82 (2010) 035204-1-5.

[87] L.-D. Zhao, S. Hao, S.-H. Lo, C.-I. Wu, X. Zhou, Y. Lee, H. Li, K. Biswas, T.P. Hogan, C. Uher, C. Wolverton, V.P. Dravid, M.G. Kanatzidis, J. Am. Chem. Soc. 135 (2013) 7364-7370.

[88] H. Wang, Z.M. Gibbs, Y. Takagiwa, G. J. Snyder, Energy Environ. Sci. 7 (2014) 804-811.

[89] H. Wang, X. Cao, Y. Takagiwa, G. J. Snyder, Mater. Horiz. 2 (2015) 323-329.

[90] M.N. Vinogradova, I.M. Rudnik, L.M. Sysoeva, N.V. Kolomoet, Sov. Phys. Semicond., 2 (1969) 892-893.

[91] Y. Lee, S.-H. Lo, J. Androulakis, C.-I. Wu, L.-D. Zhao, D.-Y. Chung, T.P. Hogan, V.P. Dravid, M.G. Kanatzidis, J. Am. Chem. Soc. 135 (2013) 5152-5160.

[92] A. Jain, S.P. Ong, G. Hautier, W. Chen, W.D. Richards, S. Dacek, S. Cholia, D. Gunter, D. Skinner, G. Ceder, K.A. Persson, APL Mater. 1 (2013) 011002-1-11.

[93] S.P. Ong, L. Wang, B. Kang, G. Ceder, Chem. Mater. 20 (2008) 1798-1807.

[94] A. Jain, G. Hautier, S.P. Ong, C.J. Moore, C.C. Fischer, K.A. Persson, G. Ceder, Phys. Rev. B: Condens. Matter Mater. Phys. 84 (2011) 045115-1-10.

[95] L. Bjerg, G.K.H. Madsen, B.B. Iversen 24 (2012) 2111-2116.

[96] J.W. Doak, K.J. Michel, C. Wolverton, J. Mater. Chem. C (2015).

[97] Semiconductors: Group IV Elements, IV-IV and III-IV Compounds, Landolt-Brnstein, New Series, Group III, Vol. 41, Pt. A, edited by O. Madelung, U. Rssler, and M. Schulz, Springer-Verlag, Berlin, 2005.

[98] W.H. Strehlow, E.L. Cook, J. Phys. Chem. Ref. Data 2 (1973) 163-199.

[99] K. Hummer, A. Grüneis, G. Kresse, Phys. Rev. B 75 (2007) 195211-1-9.

[100] Y. Zhang, X. Ke, C. Chen, J. Yang, P.R.C. Kent, Phys. Rev. B 80 (2009) 024304-1-12.

[101] A. Svane, N.E. Christensen, M. Cardona, A.N. Chantis, M. van Schilfgaarde, T. Kotani, Phys. Rev. B 81 (2010) 245120-1-10.

[102] M. A. Caprio, Comput. Phys. Commun. 171 (2005) 107-118.

[103] L.E. Bell, Science 321 (2008) 1457-1461.

[104] L. Pauling, J. Am. Chem. Soc. 69 (3) (1947) 542-553.

[105] J.C. Slater, J. Chem. Phys. 41 (1964) 3199-3204.

[106] J. Androulakis, D.-Y. Chung, X. Su, L. Zhang, C. Uher, T.C. Hasapis, E. Hatzikraniotis, K.M. Paraskevopoulos, M.G. Kanatzidis, Phys. Rev. B 84 (2011) 155207-1-11.

[107] Y. Lee, S.-H. Lo, C. Chen, H. Sun, D.-Y. Chung, T.C. Chasapis, C. Uher, V.P. Dravid, M.G. Kanatzidis, Nat. Comm. 5:3640 (2014) 1-11.

[108] C.M. Jaworski, J. Tobola, E.M. Levin, K. Schmidt-Rohr, J.P. Heremans, Phys. Rev. B 80 (2009) 125208-1-10.

[109] V.F. Masterov, F.S. Nasredinov, S.A. Nemov, P.P. Seregin, N.N. Troitskaya, S.I. Bondarevskii, Semicond. 31 (1997) 1138-1139.

[110] V.A. Zykov, T.A. Gavrikova, S.A. Nemov, Semicond. 29 (1995) 154-157.

[111] J. Androulakis, Y. Lee, I. Todorov, D.-Y. Chung, M. Kanatzidis, Phys. Rev. B 83 (2011) 195209-1-9.

[112] Q. Zhang, F. Cao, K. Lukas, W. Liu, K. Esfarjani, C. Opeil, D. Broido, D. Parker, D.J. Singh, G. Chen, Z. Ren, J. Am. Chem. Soc. 134 (42) (2012) 17731-17738.

[113] S. Bajaj, M.G. Haverty, R.Arróave, W.A. Goddard III FRSC, S. Shankar, Nanoscale 7 (2015) 9868-9877.

[114] G. Kaptay, J Mater Sci 47 (2012) 8320-8335.

[115] W.A. Jesser, R.Z. Shneck, W.W. Gile, Phys. Rev. B 69 (2004) 144121.

[116] J. Lee, J. Lee, T. Tanaka, H. Mori, K. Penttilä, JOM 57 (2005) 56-59.

[117] N. Braidy, G.R. Purdy, G.A. Botton, Acta Mat. 56 (2008) 5972-5983.

[118] J. Lee, J. Lee, T. Tanaka, H. Mori, Nanotech. 20 (2009) 475706-1-4.

[119] C. Zou, Y. Gao, B. Yang, Q. Zhai, J Mater Sci: Electron Mater 21 (2010) 868-874.

[120] T.T. Bao, Y. Kim, J. Lee, J.-G. Lee, Mater. Trans. 51 (2010) 2145-2149.

[121] J.-G. Lee, H. Mori, Eur. Phys. J. D 34 (2005) 227-230.

[122] M. Wautelet, J. Phys. D: Appl. Phys. 24 (1991) 343-346.

[123] J.-A. Yan, L. Yang, M.Y. Chou, Phys. Rev. B 76 (2007) 115319-1-6.

[124] H. Naganuma, K. Sato, Y. Hirotsu, J. Magn. Magn. Mater. 310 (2007) 2356-2358.

[125] M. Quinten, Optical Properties of Nanoparticle Systems: Mie and Beyond, Wiley-VCH, 2011.

[126] B.F.G. Johnson, Top. Catal. 24 (2003) 147-159.

[127] M. Takagi, J. Phys. Soc. Jpn. 9 (1954) 359-363.

[128] C.L. Chen, J.-G. Lee, K. Arakawa, H. Mori, Appl. Phys. Lett. 99 (2011) 013108-1-3.

[129] W.A. Jesser, C.T. Schamp, Phys. Stat. Sol. (c) 5 (2008) 539-544.

[130] G.E. Moore, Electronics 38 (1965).

[131] J. Park, J. Lee, CALPHAD 32 (2008) 135-141.

[132] B.J. Kim, J. Tersoff, C.-Y. Wen, M.C. Reuter, E.A. Stach, F.M. Ross, Phys. Rev. Lett. 103 (2009) 155701-1-4.

[133] J.W. Gibbs, Trans Conn Acad Arts Sci 3:108 (1875-1878) 343.

[134] Y. Eichhammer, M. Heyns, N. Moelans, CALPHAD 35 (2011) 173-182.

[135] http://www.math.rutgers.edu/ erowland/polyhedra.html

[136] http://wordpress.mrreid.org/2011/10/20/spherical-ice-cubes-and-surface-area-to-volume-ratio/

[137] J. Lee, T. Tanaka, J.G. Lee, H. Mori, CALPHAD 31 (2007) 105-111.

[138] T. Ivas, A.N. Grundy, E. Povoden-Karadeniz, L.J. Gauckler, CALPHAD 36 (2012) 57-64.

[139] J.A.V. Butler, Proc. R. Soc. A 135 (1932) 348-375.

[140] T. Tanaka, K. Hack, T. Iida, S. Hara, Z. Metallkd. 87 (1996) 380-389.

[141] T. Tanaka, K. Hack, S. Hara, CALPHAD 24 (2000) 465-474.

[142] Z. Moser, W. Gasior, J. Pstrus, J. Phase Equilib. 22 (2001) 254-258.

[143] J. Lee, W. Shimoda, T. Tanaka, Mater. Trans. 45 (2004) 2864-2870.

[144] R. Picha, J. Vrestal, A. Kroupa, CALPHAD 28 (2004) 141-146.

[145] K.S. Yeum, R. Speiser, D.R. Poirier, Metall. Trans. B 20 (1989) 693-703.

[146] T. Tanaka, S. Hara, Z. Metallkd. 92 (2001) 467-472.

[147] T. Tanaka, S. Hara, Z. Metallkd. 92 (2001) 1236-1241.

[148] B. Fultz, Phase Transitions in Materials, Cambridge University Press eBook, Cambridge, UK, 2014.

[149] J. Lee, M. Nakamoto, T. Tanaka, J. Mater. Sci. 40 (2005) 21672171.

[150] L.E. Murr, Interfacial Phenomena in Metals and Alloys, Addison-Wesley Publishing Company, London, 1975, p. 124.

[151] F. Millot, V. Sarou-Kanian, J.C. Rifflet, B. Vinet, Mat. Sci. Eng. A 495(2008) 8-13.

[152] R.J. Jaccodine, J. Electrochem. Soc. 110 (1963) 524-527.

[153] T. Iida, R.I.L. Guthrie, The Physical Properties of Liquid Metals, Oxford Science Publications, (1993).

[154] I. Sa, B.-M. Lee, C.-J. Kim, M.-H. Jo, B.-J. Lee, CALPHAD 32 (2008) 669-674.

[155] K.C. Mills: Recommended values of thermophysical properties for selected commercial alloys, Woodhead Publishing Ltd., Cambridge, UK, 2002.

[156] J. Schmitz, J. Brillo, I. Egry, R. Schmid-Fetzer, Int. J. Mater. Res. 100:11 (2009) 1529-1535.

[157] W.R. Tyson, W.A. Miller, Surf. Sci. 62 (1977) 267-276.

[158] L.Z. Mezey, J. Giber, Jap. J. App. Phys. 21:11 (1982) 1569-1571.

[159] G. Garzel, J. Janczak-Rusch, L. Zabdyr, CALPHAD 36 (2012) 52-56.

[160] J. Brillo, I. Egry, J. Westphal, Int. J. Mat. Res. 99 (2008) 162-167.

[161] W. Gasior, Z. Moser, J. Pstrus, J. Phase Equilib. 21 (2000) 167171.

[162] M. Gündüz, J.D. Hunt, Acta Metall. 33 (1985) 1651-1672.

[163] N. Saunders, Al-Cu system, in: I. Ansara, A.T. Dinsdale, M.H. Rand (Eds.), COST-507: Thermochemical Database For light Metal Alloys, European Communities, Luxemburg (1998) 28-33.

[164] V.T. Witusiewicz, U. Hecht, S.G. Fries, S. Rex, J. Alloys Cmpds. 385 (2004) 133-143.

[165] A. Kroupa, T. Kana, A. Zemanova, In Proceedings of Nanocon 2012 conference, Brno, Czech Republic, 2012.

[166] A. Meetsma, J.L. De Boer, S. Van Smaalen, J. Solid State Chem. 83 (1989) 370-372.

[167] J.P. Perdew, A. Zunger, Phys. Rev. B 23 (1981) 5048-5079.

[168] N. Eustathopoulos, B. Drevet, J. Crys. Growth 371 (2013) 77-83.

[169] B.J. Keene, Surf. Interf. Analy. 10 (1987) 367-383.

[170] P.R. Couchman, W.A. Jesser, Nature 269 (1977) 481-483.

[171] A.N. Goldstein, Appl. Phys. A: Mater. Sci. Process. 62 (1995) 33-37.

[172] V. I. Levitas, K. Samani, Nat. Commun. 2:284 (2011) 1-6.

[173] V. I. Levitas, K. Samani, Phys. Rev. B 89 (2014) 075427-1-10.

[174] F.G. Meng, H.S. Liu, L.B. Liu, Z.P. Jin, J. Alloys Cmpds. 431 (2007) 292-297.

[175] R.W. Olesinski, G.J. Abbaschian, Bull. Alloy Phase Diagrams 5 (1984) 180-183.

[176] Y.-B. Kang, C. Aliravci, P.J. Spencer, G. Eriksson, C.D. Fuerst, P. Chartrand, A.D. Pelton, JOM 61 (4) (2009) 75-82.

[177] S.M. Chathoth, B. Damaschke, K. Samwer, S. Schneider, J. Appl. Phys. 106 (2009) 103524-14.

[178] R.O. Jones, O. Gunnarsson, Rev. Mod. Phys. 61 (1989) 689-746.

[179] K. Dick, T. Dhanasekaran, Z. Zhang, D. Meisel, J. Am. Chem. Soc. 124 (2002) 2312-2317.

[180] Ph. Buffat, J.-P. Borel, Phys. Rev. A 13 (1976) 2287-2298.

[181] A.F. Lopeandía, J. Rodríguez-Viejo, Thermochim. Acta 461 (2007) 82-87.

[182] V.I. Arkharov, L.M. Magat, Phys. Met. Metallogr. 6(5) (1958) 32-36.

[183] M. Ellner, K. Kolatschek, B. Predel, J. Less-Common Met. 170 (1991) 171-184.

[184] C. Kittel, Introduction to Solid State Physics, sixth edition, John Wiley, (1986).

[185] J. Sun, S.L. Simon, Thermochim. Acta 463 (2007) 32-40.

[186] D. Mott, J. Galkowski, L. Wang, J. Luo, C-J. Zhong, Langmuir 23 (2007) 5740-5745.

[187] P. Laty, J.C. Joud, P. Desré, Surf. Sci. 69 (1977) 508-520.